Doctoral Dissertation

Measurements of the charge asymmetry in dilepton channels of top quark pair production in pp collisions at $\sqrt{s} = 13$ TeV with the ATLAS detector (ATLAS実験での重心系エネルギー 13 TeV におけるダイレプトン事象を用いた トップクォーク対電荷非対称度の測定)

Shogo Kido
木戸 将吾

Graduate School of Science,
Kobe University

January 2019

Abstract

This thesis presents an improvement of estimation method of the systematic uncertainties about the charge asymmetry in top quark pair production at $\sqrt{s} = 13\,\text{TeV}$ with the ATLAS detector. The data set corresponds to an integrated luminosity of $79.7\,\text{fb}^{-1}$, recorded in 2015, 2016 and 2017. The measurement focuses on dilepton channels (ee, eμ, $\mu\mu$). The data are unfolded to parton level at full phase space using a fully Bayesian unfolding method. The bayesian technique "marginalization" is used to deal with nuisance parameters affecting this measurement. By the technique, the systematic uncertainties have succeeded to reduce much smaller than the result at the $\sqrt{s} = 8\,\text{TeV}$. The differential measurements are performed as a function of the invariant mass, transverse momentum and longitudinal boost of the $t\bar{t}$ system.

Contents

Chapter 1

Introduction

The particle physics has been developed in theories and experiments. This leds to the establishment of the Standard Model (SM) of the particle physics from 1970s. In the SM, the material in the universe consists of fermions. The fermions are composed of quarks and leptons of three generations, where each generation consists of two types of quarks and leptons. The interactions between elemental particles are mediated by vector bosons, which are formulated in a frame of the gauge theory. Three types of interactions, electromagnetic, strong and weak interactions are distinguished in the SM. The gauge bosons associated with the interactions are photons (electromagnetic), gluons (strong) and W or Z bosons (weak). The discovery of the Higgs boson is reported in July 2012. The Brout–Englert–Higgs mechanism [1],[2], which is the topic of the 2013 Nobel Prize in Physics, explains where the masses of elementary particles come from.

Despite its splendid success, the SM still cannot explain key concepts in our understanding of the universe; the exist of dark matter, the mass of the neutrino and the lack of antimatter in our universe. There are thousands of Beyond Standard Model (BSM) theories that make an effort to unite our current understanding of the universe with new ideas. For example, the axigluons [3] are predicted to be massive in BSM theories. Axigluons may be discovered when interactions are studied at higher energy. In these years, searches for BSM have been performed actively in various experiments.

The large mass of the top quark ($m_t \sim 173\,\mathrm{GeV}$) suggests that the top quark may be connected to heavy particles in some BSM models as well as couples strongly with the Higgs in the SM. Top quark decays into a W boson and a b quark almost without exception. Top quark has a very short lifetime ($\tau_t \sim 10^{-25}\,\mathrm{s}$) and decays before hadronization. This allows an experimental test of the properties of a bare quark. Therefore, precise measurements of the top quark properties are very interesting.

The top-pair production cross section at the Large Hadron Collider (LHC) [4] can collect the world's largest number of events; $\sim 6 \times 10^7$ $t\bar{t}$ events in case of top-pair

production cross section ($\sigma(pp \to t\bar{t}) \sim 820\,\text{pb}$) in an integrated luminosity of 79.7 fb^{-1} at $\sqrt{s} = 13\,\text{TeV}$. The production of $t\bar{t}$ pairs at LHC in proton–proton collisions is symmetric under charge conjugation at leading order (LO) in quantum chromodynamics (QCD). There are the LO Feynman diagrams for the $t\bar{t}$ production via gluon-gluon fusion process ($\sim 90\%$, dominant process at LHC) and $q\bar{q}$ annihilation process ($\sim 10\%$).

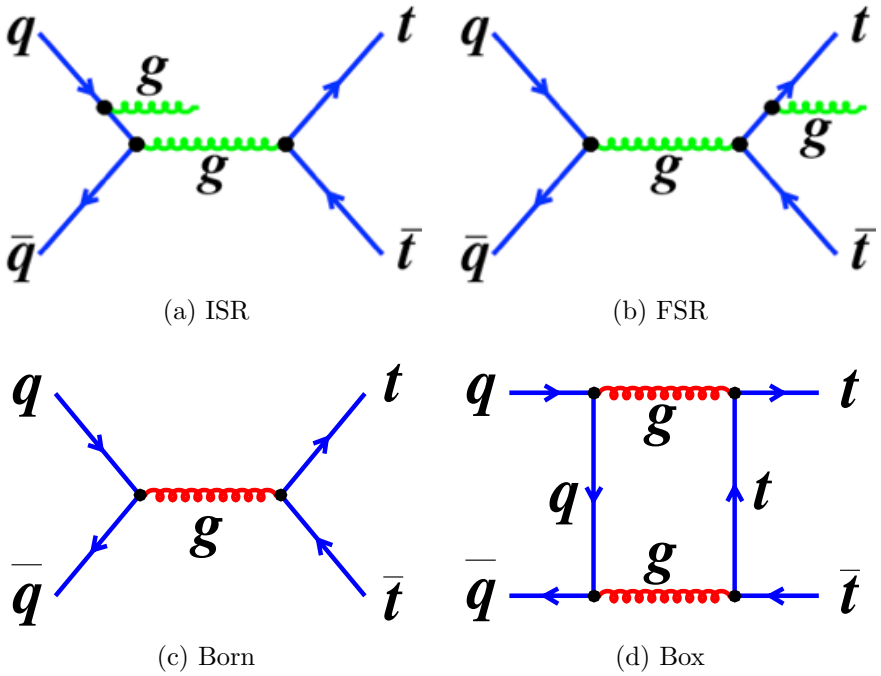

Figure 1.1: Feynman diagrams for initial-state radiation (ISR) (a), final-state radiation (FSR) (b), Born (c) and Box (d)

At next-to-leading order (NLO) in QCD, an asymmetry arises from interference between different Feynman diagrams with the $q\bar{q}$ annihilation process [5].
The charge asymmetry, $A_C^{t\bar{t}}$, is defined as the following formula, by using $\Delta|y| = |y(t)| - |y(\bar{t})|$,

$$A_C^{t\bar{t}} = \frac{N(\Delta|y| > 0) - N(\Delta|y| < 0)}{N(\Delta|y| > 0) + N(\Delta|y| < 0)} \tag{1.1}$$

here $y(t)$ and $y(\bar{t})$ are reconstructed rapidities of the top and antitop quark. $N(\Delta|y| > 0)$ and $N(\Delta|y| < 0)$ represent the number of events with positive and negative $\Delta|y|$, respectively. The interference between initial-state radiation (ISR) (Fig. 1.1(a)) and final-state radiation (FSR) (Fig. 1.1(b)) diagrams leads to a negative asymmetry value. The interference between the Born (Fig. 1.1(c)) and Box (one-loop) (Fig. 1.1(d)) diagram of the $q\bar{q} \to t\bar{t}$ leads to a positive asymmetry value. The measured charge asymmetry, $A_C^{t\bar{t}}$ value in an integrated luminosity of 20.3 fb^{-1} at $\sqrt{s} = 8\,\text{TeV}$ in the LHC was $A_C^{t\bar{t}} = 0.021 \pm 0.016$ [6]. The meas-

urements at $\sqrt{s} = 8$ TeV are compatible the inclusive $t\bar{t}$ with the SM prediction ($A_C^{t\bar{t}} = 0.0111 \pm 0.0004$ [7]).
At proton–antiproton collider, the $t\bar{t}$ production rate difference is often referred to as forward-backward asymmetry. The asymmetry defines as the proton direction, "forward" and the antiproton direction, "backward". The forward-backward asymmetry has the same underlying physical effects of the charge asymmetry. The forward-backward asymmetry in $t\bar{t}$ production at the Tevatron (proton–antiproton collision at $\sqrt{s} = 1.96\,\text{TeV}$) by the CDF experiment was measured 0.128 ± 0.025 [8].

In this analysis, the $t\bar{t}$ charge asymmetry, $A_C^{t\bar{t}}$, is measured with an integrated luminosity of 79.7 fb^{-1} at LHC $\sqrt{s} = 13\,\text{TeV}$ run. The measurement focuses on dilepton channels (ee, $e\mu$, and $\mu\mu$) of $t\bar{t} \to W^+bW^-\bar{b} \to l^+\nu_l b l^-\bar{\nu}_l\bar{b}$ process. The dilepton channels have some unique advantages. There are very few background events and it looks clean signature. Quark charge can be determined by charge of leptons from W decays. However, branching ratio of dilepton channels is smallest (6%) among all top decay channels. Owing to higher center-of-mass energy at LHC $\sqrt{s} = 13\,\text{TeV}$ run, large number of events can be obtained with higher cross section and higher luminosity compared to measurements at $\sqrt{s} = 8\,\text{TeV}$.
However, two neutrinos are produced and escape undetected in dilepton channels. It is not easy to measure the top and antitop quark in dilepton channels. The neutrino weighting method (NW method) [9] is adopted to reconstruct momenta of top and antitop quarks by searching most probable directions of escaped neutrinos. In the measurement at $\sqrt{s} = 8\,\text{TeV}$, these momenta were reconstructed using the likelihood in multivariate variable. In NW method, these momenta can be decided with fewer unknown variables.
At the last stage of analysis, it is mandatory to know the bare $\Delta|y|$ distribution in order that experiment results are compared to theoretical expectation. The observed $\Delta|y|$ distribution needs to be corrected by using the technique named "unfolding". The reason is because the observed $\Delta|y|$ distribution is distorted due to detector resolution and acceptance effects. The response matrix can be calculated by comparing reconstruction-level $\Delta|y|$ distribution with MC truth-level one. In particular for the differential measurement, a difference of reconstruction-level and MC truth-level $\Delta|y|$ distribution may become large for each bin in the response matrix. The response matrix has the uncertainties related to detector resolution acceptance effects and theoretical models. For example, the uncertainties about $t\bar{t}$ MC generator modeling (matrix element, parton shower and radiation) are large. These are called as the systematic uncertainties in this analysis. In this measurement, a method called marginalization in *Fully Bayesian Unfolding* [10] based on bayesian statistics is used to surpress the systematic uncertainties. The marginalization means making the effects of nuisance parameter which are unknown values affecting systematic uncertainties are unimportant and powerless in an unfair way.

To decide to be agreement in the gaussian prior and posterior probability density fitted MC data for each nuisance parameters, it is used the unfolding based on bayesian statistics. Total systematic uncertainties are surpressed by lowering differences between prior and posterior probability density. By this method, the systematic uncertainties can be reduced to about one-half successfully and smaller than the statistical errors.

In this thesis, the A_C is measured differentially as a function of the invariant mass m, transverese momentum p_{T}, and velocity β_z of the $t\bar{t}$ system, as well as inclusive measurements. Owing to higher center-of-mass energy at LHC $\sqrt{s} = 13\,\mathrm{TeV}$ run, more sensitive measurements at the higher mass region of $t\bar{t}$ system, where the sensitivity in BSM models expected to be enhanced, can be carried out compared to $\sqrt{s} = 8\,\mathrm{TeV}$ measurements. The charge asymmetry can be enhanced due to $t\bar{t}$ production via the exchange of new heavy particles in BSM theories. At low $p_{\mathrm{T}}^{t\bar{t}}$, the asymmetry is dominated by the positive contribution from Born and one-loop amplitude interference. At high $p_{\mathrm{T}}^{t\bar{t}}$, the interference of ISR and FSR amplitudes causes a negative asymmetry. Thus, the measurements as a function of $p_{\mathrm{T}}^{t\bar{t}}$ probes different sources of asymmetry. At high $\beta_z^{t\bar{t}}$, the quark in a proton is boosted and the fraction of the $t\bar{t}$ production via $q\bar{q}$ annihilation is larger and the asymmetry is enhanced in a model independent way. The value of the $t\bar{t}$ charge asymmetry can be observed larger in higher $\beta_z^{t\bar{t}}$ region.

The structure of this thesis is the following. In Chapter 2, the theories about the $t\bar{t}$ pair production at LHC are discussed. In Chapter 3, the experimental setup with the ATLAS detector are discussed. In Chapter 4, it is shown in the collected data sample and simulation samples. In Chapter 5, the definition for the physics objects used in this analysis are discussed. Chapter 6 summarizes selection criteria, background estimation and the reconstruction of physics objects used in this analysis. In Chapter 7, the unfolding method to calculate bare $\Delta|y|$ distribution from the reconstruction-level $\Delta|y|$ distribution is discussed. Estimation of systematic uncertainties are discussed in Chapter 8. The sensitivities of $t\bar{t}$ charge asymmetry in inclusive and differential measurements and disscussion about the measured $t\bar{t}$ charge asymmetry are presented in Chapter 9. Last Chapter gives the conclusion of this thesis.

Chapter 2

Top-pair physics

This chapter provides the theories necessary to motivate the study in the thesis. The Standard Model (SM) physics related to the top quark and the $t\bar{t}$ production mechanism are discussed. The concepts of $t\bar{t}$ charge asymmetry in SM and BSM physics are described in section 2.3 and 2.4.

2.1 Standard Model

In the SM physics, there are two types of elementary particles. One of them is called fermions which obeys the Fermi-Dirac statistics, while the other is called bosons obeying the Bose-Einstein statistics. In the SM, there are three types of particles: spin-1/2 quarks and leptons (fermions) that consist matters in the universe, gauge bosons with the spin-1 mediating the interaction acting between particles and the spin-0 Higgs boson feeding their masses. These SM particles are summarized in in Fig. 2.1. Within the SM, the top quark is the third generation up-type quark.

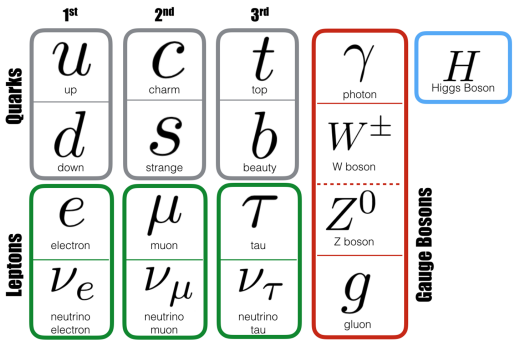

Figure 2.1: The elementary particles of the Standard Model (SM). [11]

The top quark was discovered by the CDF and DØ experiments in 1995 at the Tevatron (proton-antiproton collider), with a center-of-mass energy $\sqrt{s} = 1.8\,\text{TeV}$

at Fermilab [12], [13]. Since then its properties (mass, couplings, production cross-section, charge asymmetry, etc.) have been studied extensively during Tevatron's runs (2002-11). Among them, The top quark mass, m_t ($\sim 173\,\mathrm{GeV}$) especially is a key parameter in the SM. The top quark couples strongly with the Higgs sector because of its large mass.
Furthermore, because of its enormous mass, the top quark life-time ($\tau_t \sim 10^{-25}\,\mathrm{s}$) is shorter than the hadronization time-scale ($O(10^{-24}\,\mathrm{s})$) and thus it provides a unique opportunity to study the bare quark. From constraint of the CKM (Cabibbo-Kobayashi-Maskawa) matrix [14], [15], the branching fraction of $t \to bW$ is predicted to be almost 100% by the SM. Top quark is the only quark heavy enough to decay into a real (on-shell) W boson. The W boson decays into a charged lepton and a neutrino with a branching fraction of ∼11% for each flavour of leptons. The W boson also decays into a pair of quarks with a branching fraction of ∼67%. The experimental signature is a jet containing a bottom hadron ("b-jet") and the W boson decay products. By how the W boson decays, top decays are classified. The decay branching ratio of possible combinations in the final state of the top pair production are shown in Fig. 2.2. For example, the diagram of two leptons decay channel (dilepton channels) of $t\bar{t}$ is shown in Fig. 2.3. There are two high transverse momentum charged leptons, a large missing transverse energy from two neutrinos and two b-quark jets in this final state.

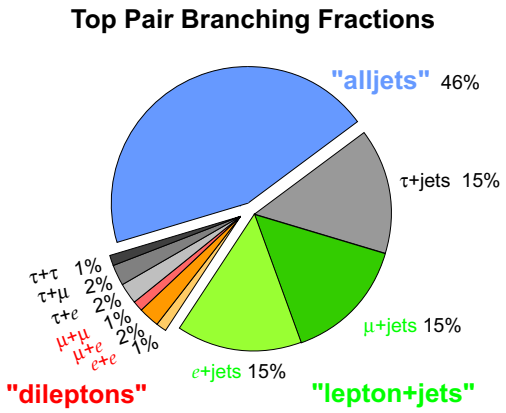

Figure 2.2: $t\bar{t}$ decay channels and branch ratio

2.2 $t\bar{t}$ production cross section

Top (top-antitop) pair ($t\bar{t}$) production are produced through the strong interaction, while single top quark production occurs via the electroweak interaction. Top quarks are produced through two kinds of processes at the leading-order (LO), namely quark-antiquark annihilation ($q\bar{q} \to t\bar{t}$) and gluon-gluon fusion ($gg \to t\bar{t}$). The diagrams for $t\bar{t}$ production in the LO via $q\bar{q}$ and gluon-gluon fusion are shown

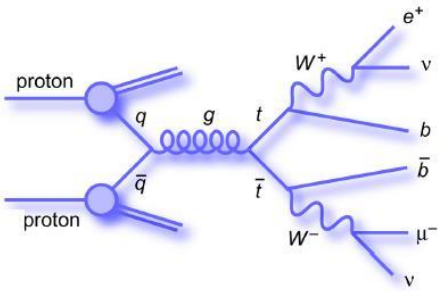

Figure 2.3: Diagram of dilepton channel ($e\mu$ channel)

in Fig. 2.4. In the proton-proton collider (LHC) at $\sqrt{s} = 13\,\text{TeV}$, The $t\bar{t}$ pairs are produced through gluon fusion (∼90%) and quark-antiquark annihilation (∼10%). Since the LHC is a proton-proton collider, the anti-quarks are sea quarks. In contrast to the proton-antiproton collider (Tevatron), gluon-gluon fusion is the dominant process.

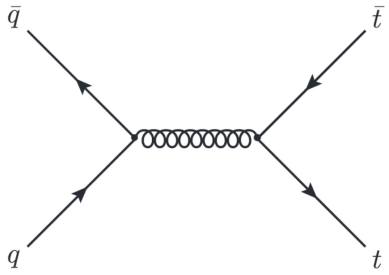

(a) quark-antiquark annihilation

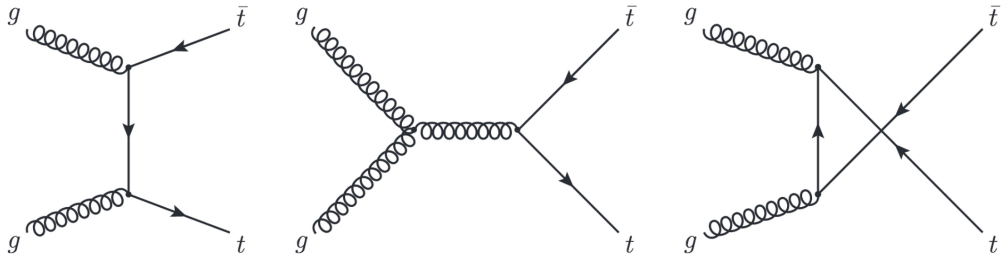

(b) gluon-gluon fusion

Figure 2.4: Feynman diagrams for the top quark production via $q\bar{q}$ annihilation (a), and gluon-gluon fusion processes (b).

The process of high energy proton-proton collisions at LHC is rather complex, involving both soft QCD processes and hard processes. A diagrammatic structure of a generic hard scattering process in proton-proton collision is shown in Fig. 2.5. The type of partons a and b (quarks or gluons) participate the hard interaction $a + b \to X$. To predict the rates of the various processes a set of universal parton distribution functions (PDFs) is required. The calculation at the LHC requires

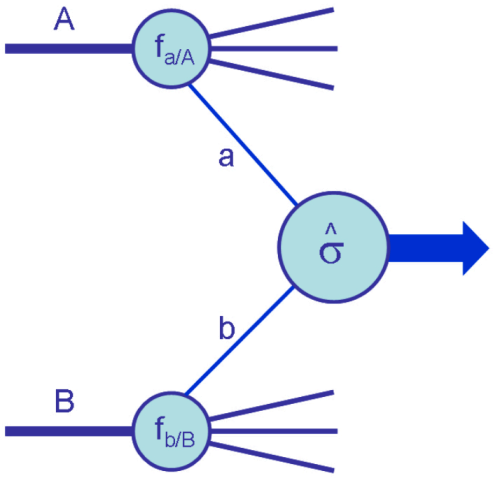

Figure 2.5: Diagrammatic structure of a generic hard scattering process.

further theoretical treatments because the proton is a composite particle. The cross section of $t\bar{t}$ production can be precisely calculated by including the next-to-leading order (NLO) and the next-to-next-to-leading order (NNLO) diagrams. The cross section calculation for collisions between proton type a and b can be written as follows,

$$\sigma_{AB} = \int dx_a dx_b f_{a/A}(x_a, \mu_F^2) f_{b/B}(x_b, \mu_F^2) \times \hat{\sigma}_{ab\to X}(\mu_R) \tag{2.1}$$

where the distribution of their parton momentum fraction in the proton, x_a, x_b are given by the PDF $f(x, \mu_F^2)$. The factorization scale, μ_F efines the boundary of energy scale treated as the hard process and the process inclusively contained in the PDF. μ_R is the renormalization scale for the QCD running coupling. The latest result of the total cross section of $t\bar{t}$ production is shown in Fig. 2.6, as a function of collision energies for hadron collider experiments.

2.3 $t\bar{t}$ charge asymmetry in the SM

In this thesis, the $t\bar{t}$ charge asymmetry is measured in dilepton channels (ee, $e\mu$, and $\mu\mu$). Since this section, as for the charge asymmetry, it is mentioned about the theoretical explanation [5]. In the SM, as shown in chapter 1, QCD predicts an asymmetry for $t\bar{t}$ produced via $q\bar{q}$ initial state at the NLO ($O(\alpha_S^3)$; α_S: QCD coupling constant). The asymmetry has its origin in two different reactions: radiative corrections to $q\bar{q}$ annihilation process (Fig. 2.7) and heavy flavor production involving interference terms of different amplitudes contributing to gluon-quark scattering ($qg \to t\bar{t}q$) (Fig. 2.8) a reaction intrinsically of $O(\alpha_S^3)$.

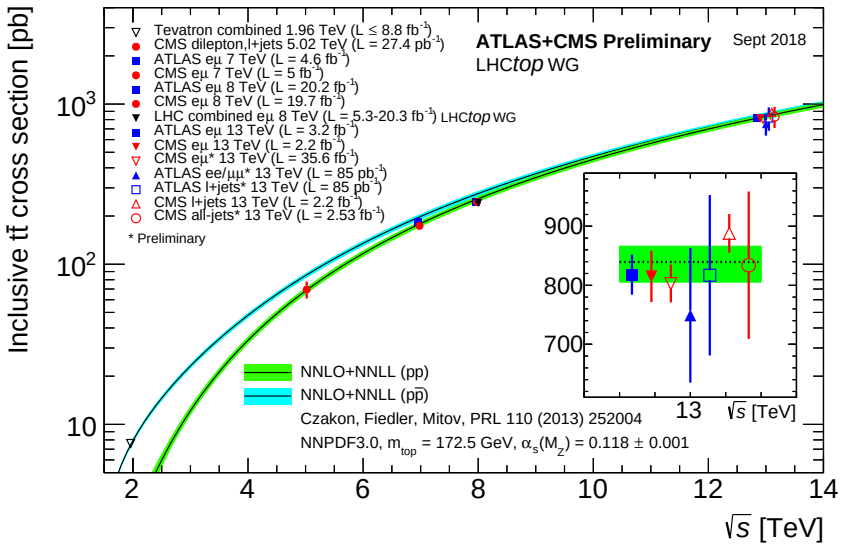

Figure 2.6: Summary of LHC and Tevatron measurements of the top-pair production cross-section as a function of the centre-of-mass energy compared to the NNLO QCD calculation

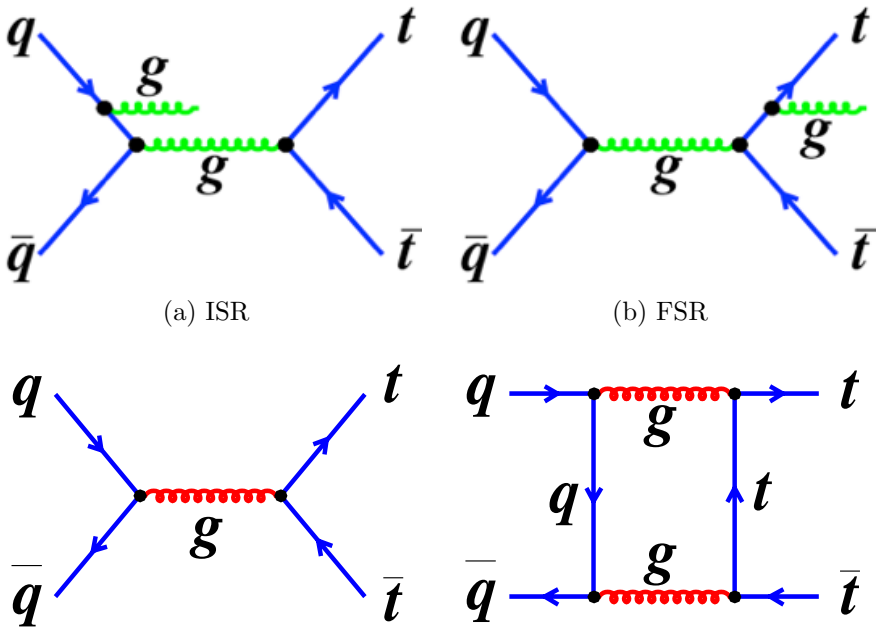

(a) ISR

(b) FSR

(c) Born

(d) Box

Figure 2.7: Diagrams for initial-state radiation (ISR) (a), final-state radiation (FSR) (b), Born (c) and Box (d)

In both $q\bar{q} \to t\bar{t}$ and $qg \to t\bar{t}q$, the asymmetry can be traced to the interference between amplitudes which are relatively odd under the exchange of t and $\bar{t}$. In detail, the charge asymmetry can be understood in analogy to the corresponding

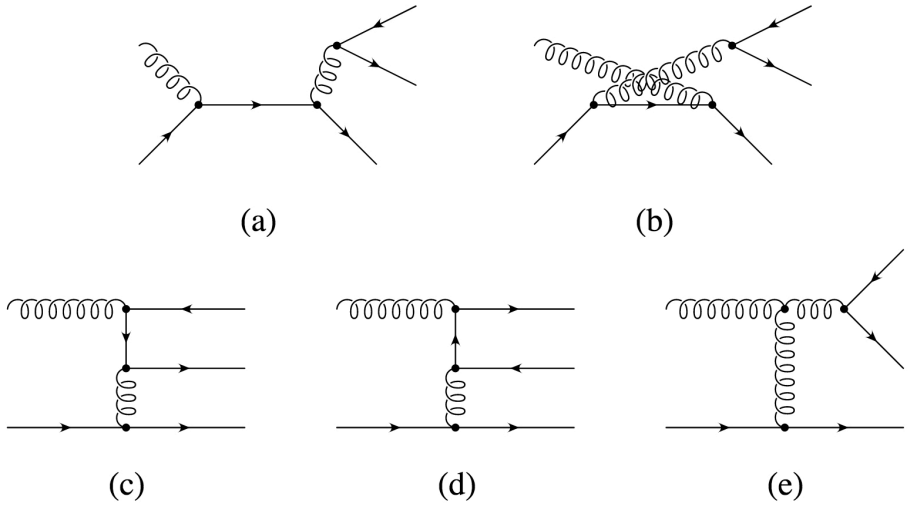

Figure 2.8: Diagrams of the charge asymmetry in production of heavy quarks through flavor excitation ($qg \to t\bar{t}q$)

one in quantum electrodynamics (QED) reactions and is proportional to the color factor d^2_{abc}. The Box diagram amplitude is ultraviolet finite and the asymmetric contribution to the cross section of $O(\alpha_S^3)$ is therefore not affected by renormalization, an obvious consequence of the symmetry of the LO process. In the $qg \to t\bar{t}q$ process, it is absent in the charge asymmetric piece. However, real and virtual radiation (Fig. 2.7), if considered separately, exhibit infrared divergences, which compensate in the sum, corresponding to the inclusive production cross section. It leads to a sizeable $t\bar{t}$ charge asymmetry which is dominated by $q\bar{q} \to t\bar{t}$, and furthermore, can be scrutinized by studying $t\bar{t}$ production at fixed longitudinal momenta and at various partonic energies $\hat{s}$. At proton-proton collisions at high energies, the $t\bar{t}$ charge asymmetry has to reconstruct the $t\bar{t}$ restframe and select kinematic regions, which are dominated by $q\bar{q}$ annihilation or flavor excitation $qg \to t\bar{t}q$. In this case, the flavor excitation has much smaller asymmetric effects than $q\bar{q}$ annihilation because the proton-proton initial state is symmetric. As mentioned in chapter.1, the dominant contribution to the charge asymmetry originates from $q\bar{q}$ annihilation, namely from the asymmetric part in the interference between the Born amplitude for $q\bar{q} \to t\bar{t}$ and the Box corrections to this reaction, which must be combined with the interference term between ISR and FSR. The corresponding contribution to the rate is conveniently expressed by the absorptive contributions (cuts) of the diagrams showned in Fig. 2.9. However, only Fig. 2.9(a) plus the crossed Fig. 2.9(b) are relevant for the charge asymmetric part. Fig. 2.9(c), Fig. 2.9(d) and Fig. 2.9(e), on the other hand lead to a symmetric contribution only.

This can be seen as follows: the color factors corresponding to Fig. 2.9(a) and 2.9(b) (after averaging over initial and summing over final states) respectively are

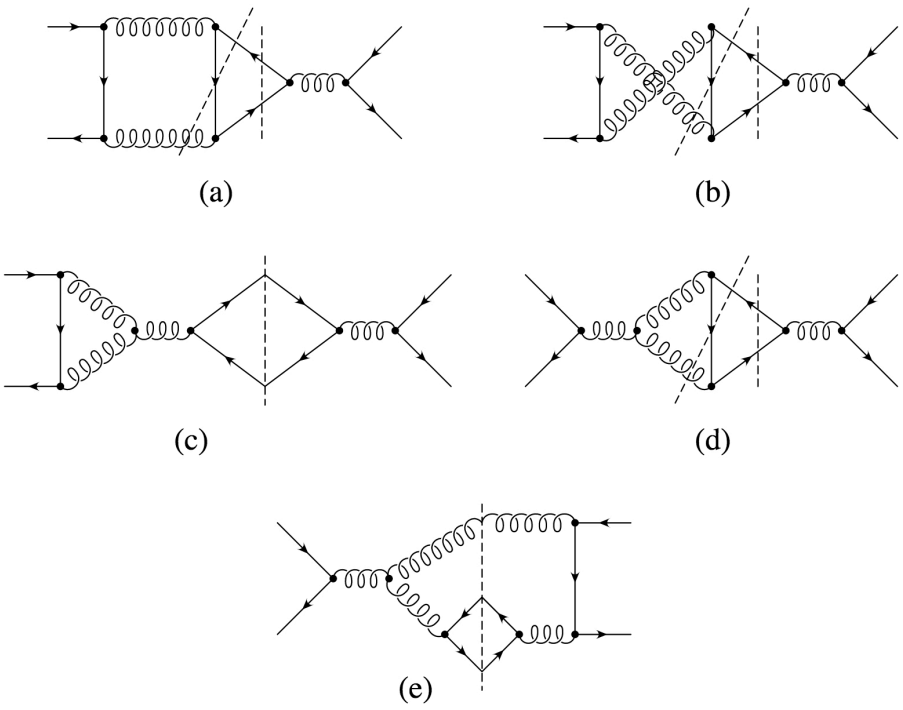

Figure 2.9: Cut diagrams for $q\bar{q} \to t\bar{t}$

given by these color coefficients

$$\begin{aligned} C_a &= \frac{1}{N_C^2} Tr\left(\frac{\lambda^a}{2}\frac{\lambda^b}{2}\frac{\lambda^c}{2}\right) Tr\left(\frac{\lambda^a}{2}\frac{\lambda^c}{2}\frac{\lambda^b}{2}\right) = \frac{1}{16N_C^2}(f_{abc}^2 + d_{abc}^2), \\ C_b &= \frac{1}{N_C^2} Tr\left(\frac{\lambda^a}{2}\frac{\lambda^b}{2}\frac{\lambda^c}{2}\right) Tr\left(\frac{\lambda^b}{2}\frac{\lambda^c}{2}\frac{\lambda^a}{2}\right) = \frac{1}{16N_C^2}(-f_{abc}^2 + d_{abc}^2), \end{aligned} \tag{2.2}$$

where the number of color charge (red, blue, green) $N_C = 3$, the Dirac operator eigenvalues $\lambda^a, \lambda^b, \lambda^c$, the structure constant $f_{abc}^2 = 24$ and the color factor $d_{abc}^2 = 40/3$. Without color factors the contributions to the cross section from Fig. 2.9(a) and 2.9(b) are related by

$$d\sigma_a(t, \bar{t}) = -d\sigma_b(\bar{t}, t), \tag{2.3}$$

which holds true both for two and three particle cuts. Therefore, the asymmetric part originates from the color factor d_{abc}^2 term.
Its form is equivalent to the corresponding QED process with the replacement of the quark charges and QED coupling by the color factor

$$\alpha_{QED}^3 Q_q^3 Q_t^3 \to \frac{1}{16N_C^2} d_{abc}^2 \alpha_S^3. \tag{2.4}$$

On the other hand, The production cross section is obtained from the corresponding QED process through the replacement

$$\alpha_{QED}^2 Q_q^2 Q_t^2 \to \frac{1}{N_C^2} N_C T_F C_F \alpha_S^2, \tag{2.5}$$

here the operator constant $T_F = 1/2$ and $C_F = (N_C^2 - 1)/2N_C^2 = 4/3$. Thus, the QCD asymmetry is also caluculated from the QED results by the replacement

$$\alpha_{QED} Q_q Q_t \to \frac{d_{abc}^2}{16 N_C T_F C_F} \alpha_S = \frac{5}{12} \alpha_S. \tag{2.6}$$

To obtain finally the asymmetric part of the inclusive cross section for $q\bar{q} \to t\bar{t}$ or $qg \to t\bar{t}q$ the integral over the real gluon spectrum is performed numerically [5].

2.4 $t\bar{t}$ charge asymmetry in the BSM theories

In this section, it is mentioned about an example of the charge asymmetry in $t\bar{t}$ production via the exchange of new heavy particles in BSM theories [16]. One generalization of QCD proposed some time ago is chiral color models [17] in which the color gauge group arises from the spontaneous breaking of a larger group at higher energy. This gives rise to a massive color octet of gauge bosons, axigluons, which couples to quarks with a pure axial-vector structure and the same strength as QCD. Chiral color models require also the existence of extra fermions to cancel anomalies, and extra Higgs bosons to break the enlarged gauge symmetry.
The Feynman diagrams for the leading contributions in the partonic process $q\bar{q} \to t\bar{t}g$ are shown in Fig. 2.10. The thin curly outgoing lines represent the QCD gluon

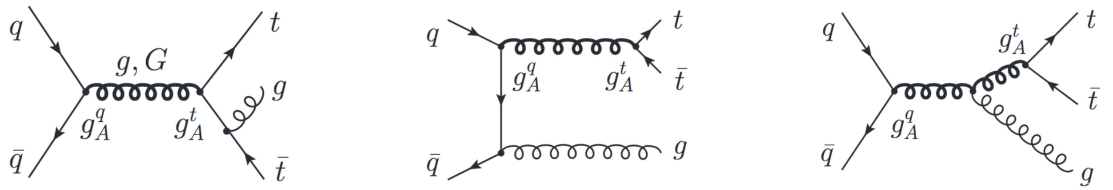

Figure 2.10: Feynman diagrams contributing to the partonic process $q\bar{q} \to t\bar{t}g$. Thin curly lines denote SM gluons while thick curly lines denote either a SM gluon (g) or an axigluon (G). Axial-vector couplings of quarks to axigluons are indicated by g_A^q and axial-vector couplings of top quarks to axigluons by g_A^t. Two more Feynman diagrams with the gluon attached to t instead of $\bar{t}$ (q instead of $\bar{q}$ in (b)) are not shown.

while the thick curly lines can stand for either a QCD gluon or an axigluon. In the most general scenario a color-octet resonance G_a^μ interacts with quarks with arbitrary vector $g_V^{q_i}$ and axial-vector $g_A^{q_i}$ strength relative to the strong coupling g_S :

$$\mathcal{L} = g_S t^a \bar{q}_i (g_V^q + g_A^q \gamma_5) \gamma^\mu G_a^\mu q_i. \tag{2.7}$$

where the covariant chirality operator γ_5 and the gamma matrices γ^μ. In explicit models, parity, gauge invariance or orthonormality of field profiles prevent a direct coupling of G_a^μ to an even number gluons; therefore it is natural to assume that the extra gauge boson do not modify gluon-gluon fusion.
The Born cross-section for $q\bar{q}$ annihilation into top quarks in the presence of a color-octet vector resonance reads [18]

$$\begin{aligned}\frac{d\sigma^{q\bar{q}\to t\bar{t}}}{d\cos\hat{\theta}} = \alpha_S^2 \frac{T_F C_F}{N_C} \frac{\pi\beta}{2\hat{s}} \Big\{ 1 + c^2 + 4m^2 + \frac{2\hat{s}(\hat{s} - m_G^2)}{(\hat{s} - m_G^2)^2 + m_G^2 \Gamma_G^2} [g_V^q g_V^t (1 + c^2 + 4m^2) \\ + 2 g_A^q g_A^t c] + \frac{\hat{s}^2}{(\hat{s} - m_G^2)^2 + m_G^2 \Gamma_G^2} [((g_V^q)^2 + (g_A^q)^2) \\ \times ((g_V^q)^2 (1 + c^2 + 4m^2) + (g_A^q)^2 (1 + c^2 - 4m^2)) + 8 g_V^q g_A^q g_V^t g_A^t c] \Big\},\end{aligned} \tag{2.8}$$

where $\hat{\theta}$ is the polar angle of the top quark with respect to the incoming quark in the centre of mass rest frame, $\hat{s}$ is partonic energies, $T_F = 1/2, N_C = 3$ and $C_F = 4/3$ are colour factors, $\beta = \sqrt{1 - 4m^2}$ is the velocity of the top quark, with $m = m_t/\sqrt{\hat{s}}$, and $c = \beta \cos\hat{\theta}$ The parameters $g_V^q, g_V^t, g_A^q, g_A^t$ represent, respectively, the vector and axial-vector couplings of the excited gluons to the light quarks (top quarks). Colour-octet vector resonances are naturally broad: $\Gamma_G/m_G = O(\alpha_S)$. The terms in above equation that are odd in c generate the charge asymmetry. Due to the factor $(\hat{s} - m_G^2)$ the charge asymmetry generated in flavour universal models, $g_A^q = g_A^t$, is in general negative. A positive asymmetry can be generated if $g_A^q g_A^t < 0$ or if the last term $8 g_V^q g_A^q g_V^t g_A^t c$ dominates over the interference [19]. Therefore, both $g_A^q g_A^t$ and $g_V^q g_A^q g_V^t g_A^t$ are negative and the interference term induces a positive asymmetry while the new physics term induces a negative asymmetry below the resonance.

In fact, various extensions of the SM predict significant enhancement of charge asymmetry value at the previous measurement. For examples, there are strongly constrained various BSM models – W', axigluon (G_μ), doublet (ϕ), color-triplet (ω^4) and color-sextet scalar (Ω^4). The comparison of these models with the SM predictions, charge asymmetry measurements at the LHC (8 TeV) and forward–backward asymmetry at the Tevatron (1.96 TeV) are provided in Fig. 2.11 and 2.12. Each point of clouds in these figures corresponds to a choice of the new particle's mass between 100 GeV and 10 TeV and of the couplings to SM particles. By good precise measuring the top quark properties, it can evaluate for new particles of some BSM models.

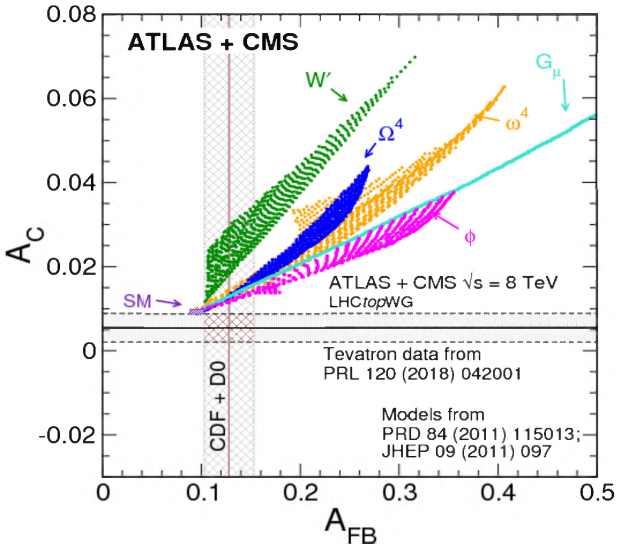

Figure 2.11: Predictions from BSM models for charge asymmetry measurement at the LHC and for forward-backward asymmetry at the Tevatron. The horizontal band represents charge asymmetry value gained from combination of ATLAS and CMS measurements. On the x-axis the forward-backward asymmetry values gained from D0 and CDF experiment are shown [20].

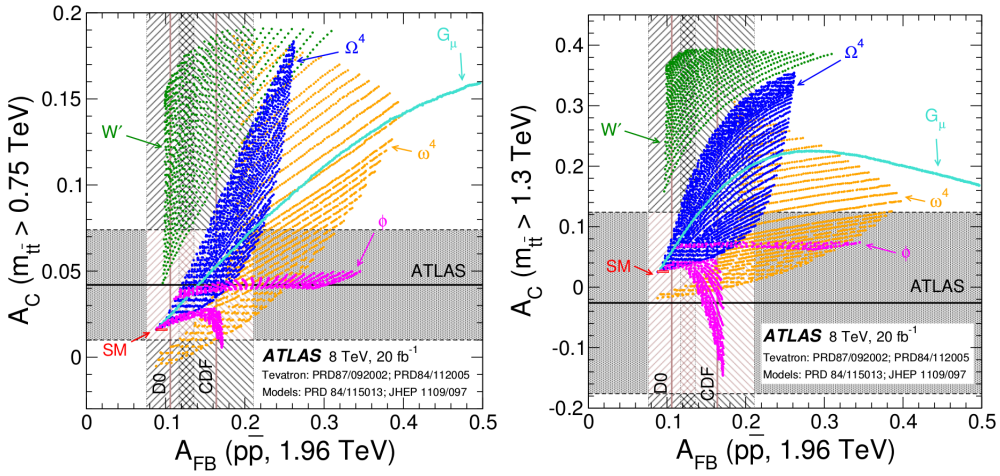

(a) (b)

Figure 2.12: Predictions from a number of extensions of the SM, for the forward–backward asymmetry integrated over $m_{t\bar{t}}$ at the Tevatron (on the x-axis in both plots) and two high-mass charge asymmetry measurements at the LHC. The y-axis in both figures represents the measurement for (a) $m_{t\bar{t}} > 0.75$ TeV and for (b) $m_{t\bar{t}} > 1.3$ TeV. The SM predictions of both the forward–backward asymmetry at the Tevatron and the charge asymmetry at the LHC are also shown [21].

The 13 TeV measurement must achieve higher precision to set an equally stringent limit as the 8 TeV result. The first boosted charge asymmetry measurement, indicated with a red band in Fig. 2.13(a). Differential measurements are expected to improve considerably in Run-2 and drive the constraints on four-fermion operators $\overline{C}_-$. The resulting individual 95% C.L. limits are shown in Fig. 2.13(b). In Fig. 2.13(b), the expected uncertainty on $\overline{C}_-$ from the 13 TeV inclusive charge asymmetry measurement with an presion of 0.5% is larger than 8 TeV measurements with a similar precision. As considered highly boosted top quark pair production with $m_{t\bar{t}} > 1.2$ TeV, if a charge asymmetry is measured in 0.5% precision, an extremely tight constraint on four-fermion interactions can be derived.

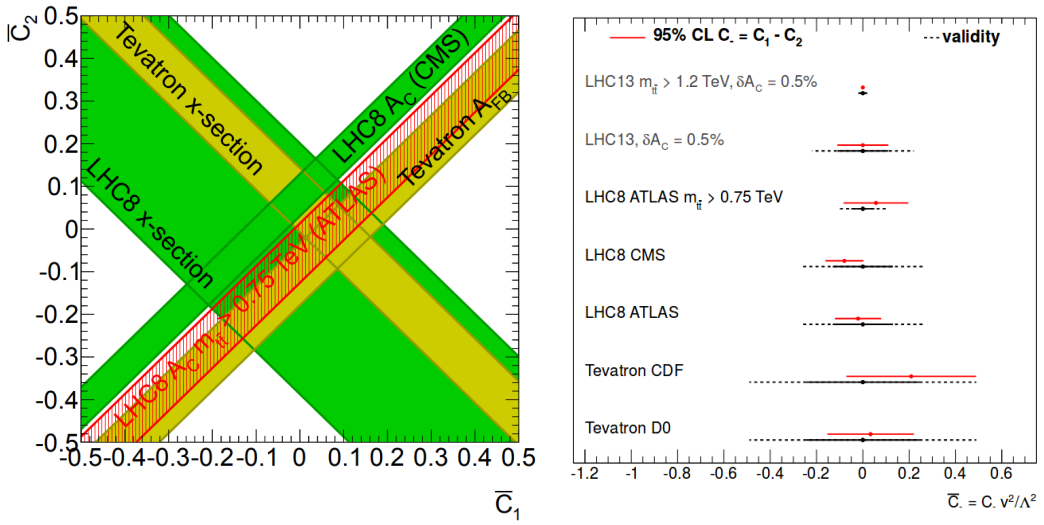

(a) (b)

Figure 2.13: The 95% C.L. limits on the linear combination of four-fermion operators $\overline{C}_- = \overline{C}_1 - \overline{C}_2$ extracted from charge asymmetry measurements at hadron colliders. The entries labelled as LHC13 present the prospects of a charge asymmetry measurement with an uncertainty of 0.5% and a central value in exact agreement with the SM prediction [22].

Chapter 3

The Large Hadron Collider and the ATLAS detector

This study was performed using the data collected by the ATLAS experiment at the LHC. In this chapter, it is mentioned about ATLAS detector focusing on the relevant points for this study.

3.1 The Large Hadron Collider

The Large Hadron Collider (LHC) is the world's largest proton-proton collider constructed at European Organization for Nuclear Research (CERN), where bunches of protons are accelerated to 7 TeV and collide head-on at center-of-mass energy at 14 TeV in its design. The four detector cites (ATLAS, CMS, ALICE and LHCb) built on the accelerator ring. ATLAS and CMS are general purpose detectors designed to study a various range of physics programs, while LHCb and ALICE are specialized in studying b-hadrons and heavy-ion collisions respectively.

The acceleration of protons with various steps: Protons are firstly seeded from hydrogen gas, by blowing the electrons off the hydrogen atoms using electric field. They are injected in the linear accelerator LINAC2 accelerated upto 50 MeV, and sent to the Proton Synchrotron Booster (PSB) with being accelerated up to an energy of 1.4 GeV. The subsequent accelerator is the Proton Synchrotron (PS) elevating the energy of the protons to 25 GeV, and injecting them into the SuperProton Synchrotron (SPS). After being accelerated to 450 GeV in SPS, the protons finally enter the two LHC pipes running the beam oppositely each other. The whole acceleration chain is shown in Fig. 3.1.

The LHC accelrator consists of octant-shaped 2.45 km arcs with 1232 superconducting magnets located at the curves, providing 8.33 T of magnetic field to bend the proton trajectory. In total, bunch-trains can be filled simultaneously at the sign condition, and 2808 bunches per beam are brought to collision in the LHC. Each bunch contains about 10^{11} protons. The beam bunches are collided

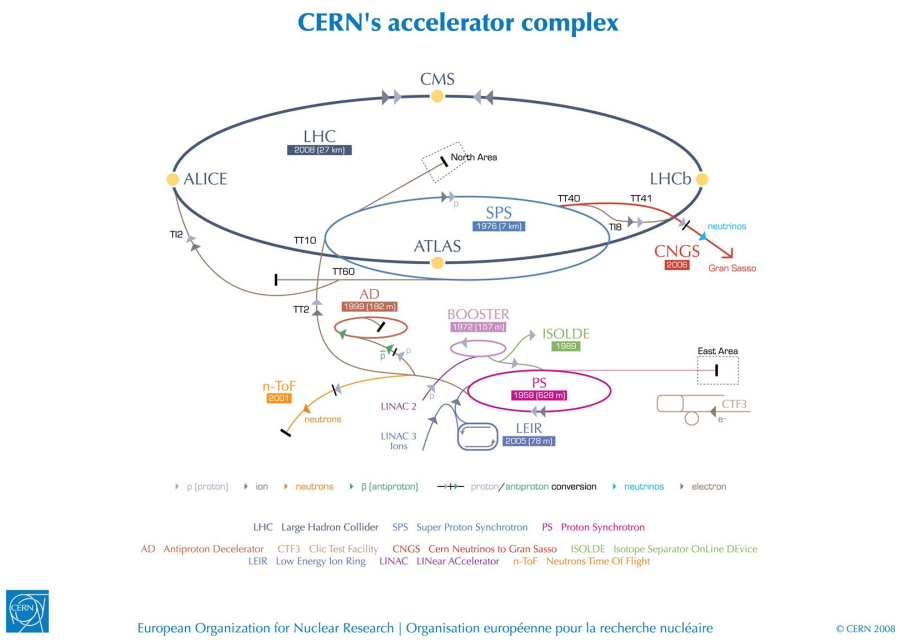

Figure 3.1: The LHC and associated booster accelerator system [23].

with a crossing angle of 285 mrad. Due to the high frequency of collisions and the dense proton bunches, multiple proton collisions can take place within the same bunch crossing, referred as "pile-up". The average pile-up μ, defined as the mean number of interactions per bunch crossing, has been evolved according to the peak luminosity increase.

3.2 The ATLAS detector

ATLAS (A Toroidal LHC ApparatuS) is a general purpose detector, aiming to a wide range of physics programs from precision measurements to the energy frontier experiments, through a dedicated measurement of particles produced in the pp collisions. The detector extends over 44 m in width and 25 m in height weighing 7000 tons in total, covering the interaction point (IP) by a cylindrical barrel and two endcaps, achieving a nearly full solid angle coverage. The cut-away image is shown in Fig. 3.2. From center to the outside, it consists of an inner tracking detector surrounded by a superconducting solenoid magnet creating a 2 T axial magnetic field, electromagnetic and hadronic calorimeter and a muon spectrometer. The particle detection in the sub-detectors is shown in Fig. 3.3 The inner tracking detector covers the pseudorapidity range $|\eta| < 2.5$. The inner track detector consists of silicon pixel, silicon micro-strip and transition radiation tracking detectors, and serves for reconstructing the trajectories of the charged particles produced in the proton-proton interactions with high precision and efficiency. Lead/liquid-argon (LAr) sampling calorimeters provide electromagnetic (EM) energy measurements with high granularity and longitudinal segmentation.

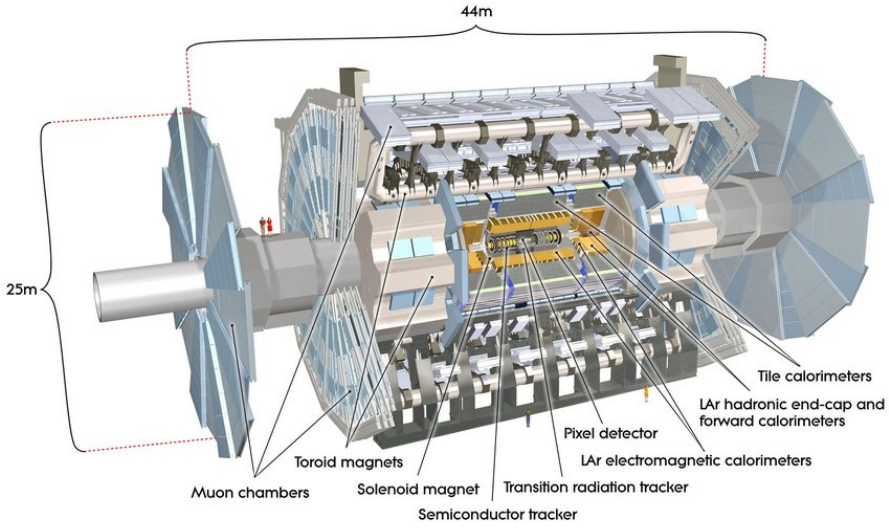

Figure 3.2: Overview of the ATLAS detector [24]. The geometry is completely forward-back symmeric.

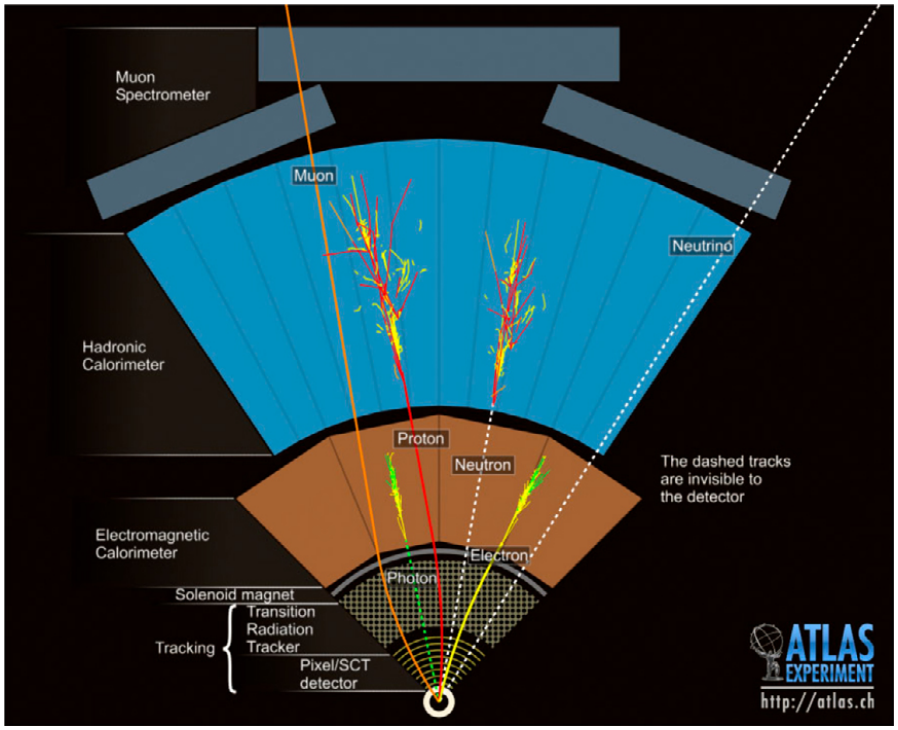

Figure 3.3: A schematic view of particle detection in the ATLAS detector [25].

A hadronic calorimeter covers the central pseudorapidity range ($|\eta| < 1.7$). The endcap and forward regions are instrumented with LAr calorimeters for both EM and hadronic energy measurements up to $|\eta| = 4.9$. The muon spectrometer is located outside of the calorimeter systems. It includes a system of precision tracking chambers and detectors with sufficient timing resolution for triggering events.

3.2.1 Coordinate system

ATLAS used right-handed Cartesian coordinate system with its origin at the nominal interaction point. The corresponding cylindrical coordinate system is shown in Fig. 3.4. The beam axis is defined as z-axis. Transverse to the beam direction

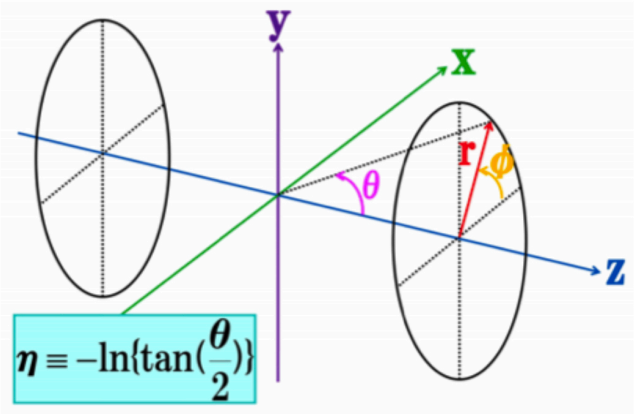

Figure 3.4: The ATLAS coordinate system.

is the x-y plane. The x-axis points from the interaction point to the center of the LHC ring, and y-axis points upwards. In spherical coordinate, the polar angle from the z-axis is θ and azimuthal angle around the z-axis is ϕ. The nominal interaction point is at the center of the detector. The pseudorapidity η is defined as:

$$\eta = -\ln\left(\tan\frac{\theta}{2}\right) \tag{3.1}$$

The pseudorapidity is generally used at the hadron colliders since the distribution of number of particles as a function of η is basically at. And the distance ΔR of the two objects in η-ϕ space is defined as:

$$\Delta R = \sqrt{(\Delta\eta)^2 + (\Delta\phi)^2} \tag{3.2}$$

3.2.2 Magnet

The ATLAS magnet system consists of a thin superconducting solenoid and three large superconducting toroids as shown in Fig. 3.5.

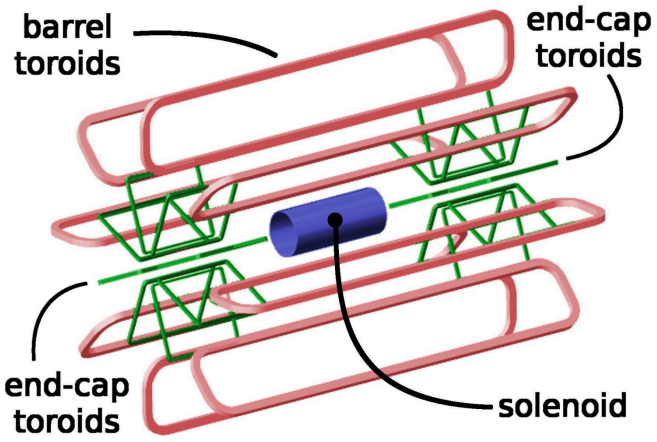

Figure 3.5: A schematic of the ATLAS magnet system with a central solenoid and three toroidals (1 barrel+ 2 endcap) [26].

- **Solenoid Magnet**
  The solenoid is aligned on the beam axis and has a 2 T axial magnetic field for the inner detector. This bends charged particles to ϕ direction for the measurement of p_{T}. It is installed in between the inner detector and the calorimeter with a length of 5.3 m and a radius of 1.2 m.

- **Toroidal Magnet**
  The toroidal magnet system is constituted by a barrel toroid and two endcap toroids. The barrel toroid provides 0.5 T magnetic field in ϕ direction for barrel region ($|\eta| < 1.05$) with a length of 25.3 m, an inner core of 9.4 m and an outer diameter of 20.1 m. There is a complicated magnetic field from the overlap between the barrel and endcap toroids in the η range of $1.4 < |\eta| < 1.6$ as shown in Fig. 3.6.

3.2.3 Inner Detector

The role of ATLAS Inner Detector (ID) is to reconstruct charged particle tracks, to measure p_{T} and charge of the tracks. The ID is immersed in a 2 T solenoid field. As shown in Fig. 3.7, it covers the pseudorapidity range $|\eta| < 2.5$. It consists of three independent layers; Pixel detector (with Insertable B-layer), Silicon micostrip Tracker (SCT) and Transition Radiation Tracker (TRT). The arrangement of the inner detector and outer tracking detector is shown in Fig. 3.8.

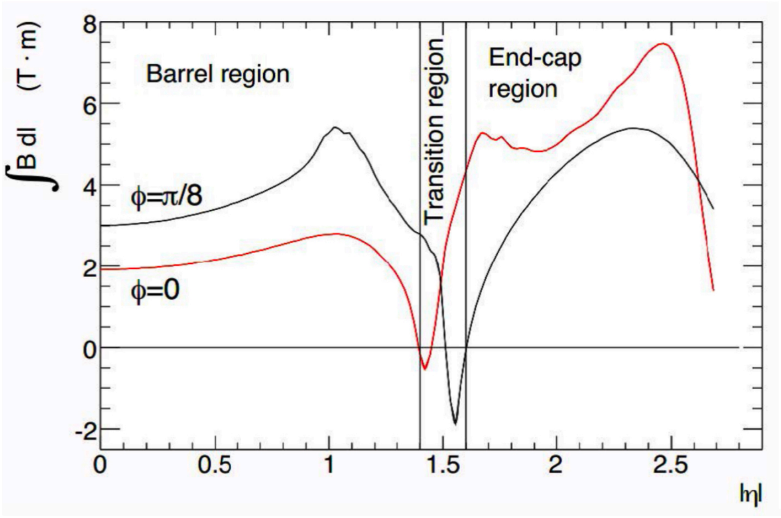

Figure 3.6: Simulated magnetic field integral provided by a single troid octant [27]. the η range of $1.4 < |\eta| < 1.6$ is called transition region

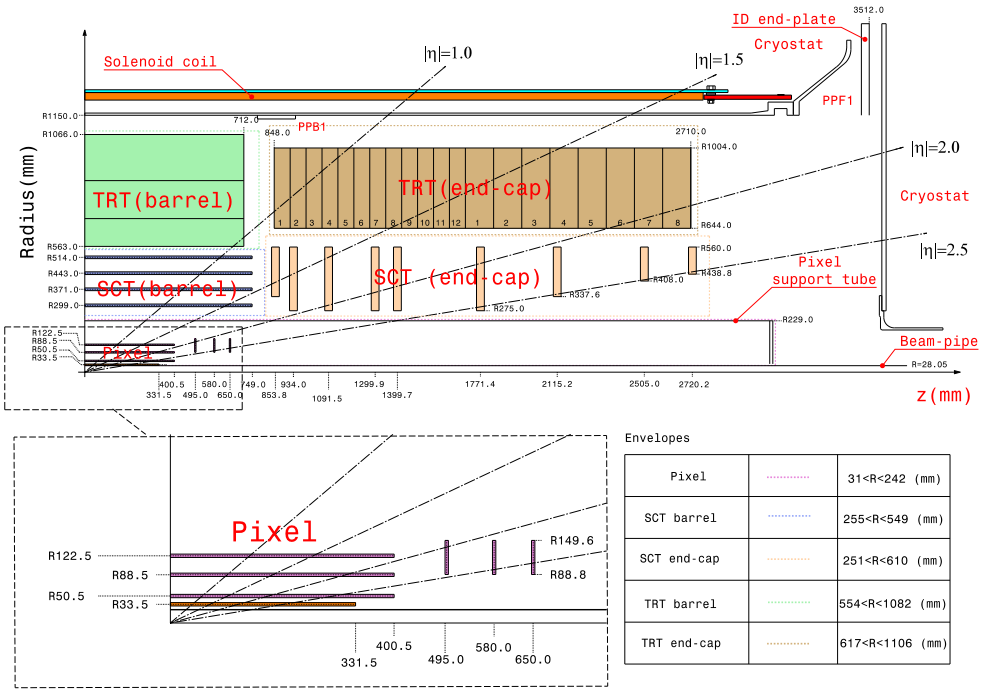

Figure 3.7: Schematic view of the $r - z$ cross section of the ATLAS inner detector for Run-2 [28].

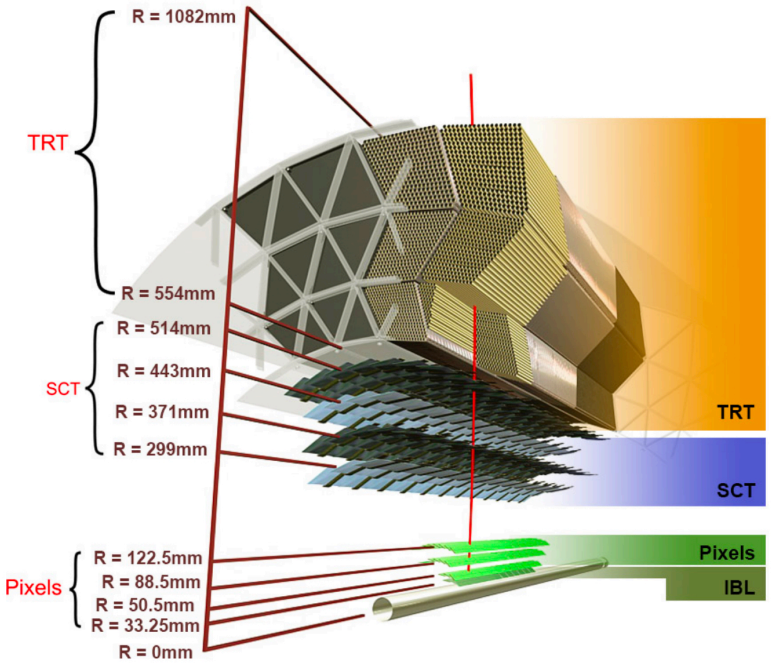

Figure 3.8: Schematic view of the inner detectors [27].

Pixel detector

In the inner radius, pixel detectors that determine collision points and vertices have high position resolution of 10 μm for r-ϕ direction and 115 μm for z direction as shown in Fig. 3.9. The pixel size is 50 $\times$ 400 μm^2 and 50 $\times$ 600 μm^2 and there

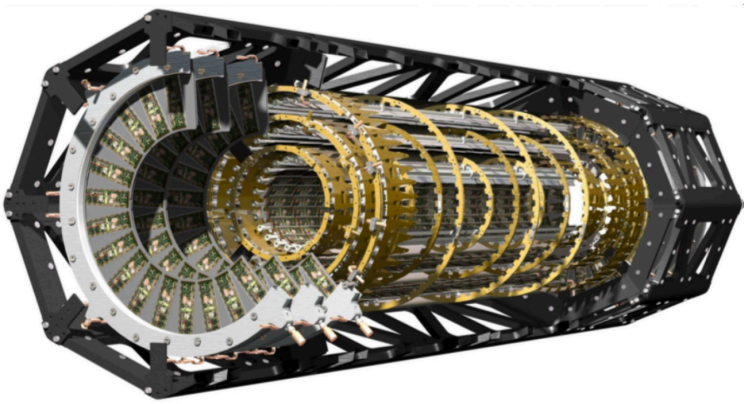

Figure 3.9: The pixel detector, showing individual barrel and endcap modules [27].

are a total of ~80 M readout channels. The innermost layer in the barrel provides the highest precision referred as the "insertable b-layer" (IBL) installed during the long shutdown between Run-1 and Run-2. The IBL is located close to the interaction point (33.25 mm from the beam) in order to improve the tracking per-

formance. The definition of transverse and longitudinal track parameters is shown in Fig. 3.10. The d_0 is the transverse impact parameter (the closest approach of the track to the beam axis), and σ_{d_0} is its resolution. The z_0 is the longitudinal impact parameter with respect to the primary vertex, and θ is the polar angle. The transverse impact parameter (d_0) resolution improved with the IBL, in particular in the low p_{T} region [29].

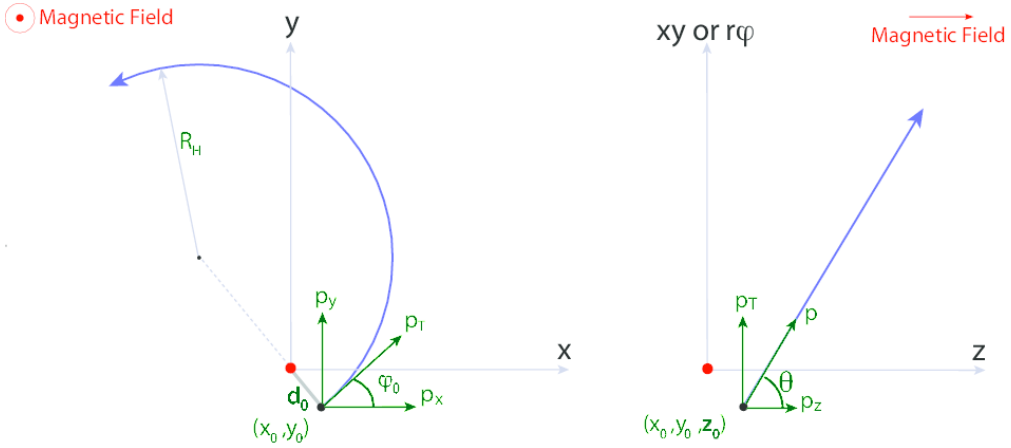

Figure 3.10: The definition of transverse and longitudinal track parameters.

Silicon micostrip Tracker (SCT)

The SCT is located outside of the pixel detector. It provides high-resolution pattern recognition (17 μm for *r-phi* direction and 580 μm for z direction). As shown in Fig. 3.11, each module consists of two back to back sensors of small angle stereo layout (20 mrad), and the array of modules are mounted in four coaxial cylinders in the barrel and nine disk layers in each endcap. The modules cover total of 63 m^2 of the surface and provide hermetic coverage with precision space-point measurements.

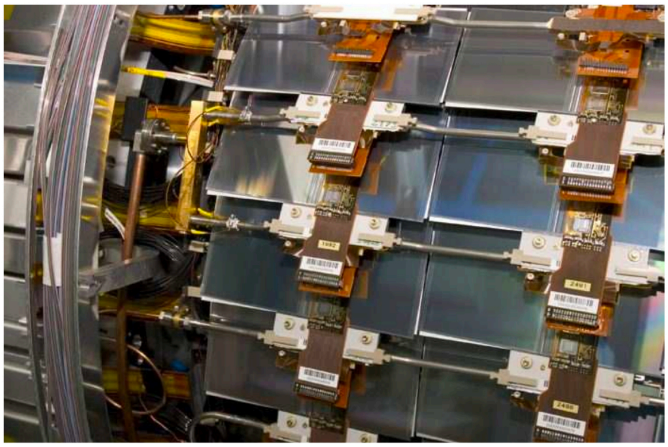

Figure 3.11: The module attached to the SCT scylinders in the barrel region [27].

Transition Radiation Tracker (TRT)

Outside of the SCT is the transition radiation tracker consisting of multi-layers of gaseous straw tube (polymide) elements. There are 73 layers of straws in the barrel and 160 layers in the endcap. The tube diameter is 4 mm and the wall thickness is minimal (35 μm). It is filled with xenon based gas ($Xe : CO_2 : O_2 = 70 : 27 : 3$) to detect X-ray photons of transition radiation from electrons as well as ionization by charged particles. The intrinsic position resolution per straw is about 130 μm.

Combined tracking in the inner detector

The combination of precision pixel measurements at short distances followed by a large number of TRT hits extending over a far greater distance allows for robust pattern recognition. The combined tracking performance has been validated via the measurement of cosmic muons [24]. The momentum resolution typically achieved with the inner detector is:

$$\frac{\sigma_{p_{\mathrm{T}}}}{p_{\mathrm{T}}} = 1.6\% \oplus 0.053\%(\mathrm{GeV}^{-1}) \times p_{\mathrm{T}} \tag{3.3}$$

3.2.4 Calorimeter

The ATLAS calorimeters (Fig. 3.12) are installed at outside of the inner tracker. The purpose of the calorimeters is to measure the energy and position of the electron, photon and hadrons. One is electromagnetic part that stops electronic magnetic showering and the other is hadronic part that stops hadrons by strong interaction. It consists of electromagnetic calorimeter (ECAL) system that stops electronic magnetic showering and a hadronic calorimeter system that stops hadrons by strong interaction, the sensitive region of which is $|\eta| < 4.9$.

Electromagnetic calorimeter (ECAL)

The liquid argon (LAr) sampling calorimeter with Pb plate absorber of accordion shape as shown in Fig. 3.13. This geometry provides a complete ϕ coverage without azimuthal cracks. Each sampling cell point towards the interaction point over the η-coverage. The ECAL is divided into a barrel part ($|\eta| < 1.475$) and two endcaps parts ($1.375 < |\eta| < 3.2$). The system measure energy and position of the particles that have electromagnetic interaction. Total thickness of the module is at least 22 radiation length (X_0) at $\eta = 0$. The main part of the calorimeter is segmented in $\eta \times \phi$ granularity of 0.025×0.025. The energy resolution of the

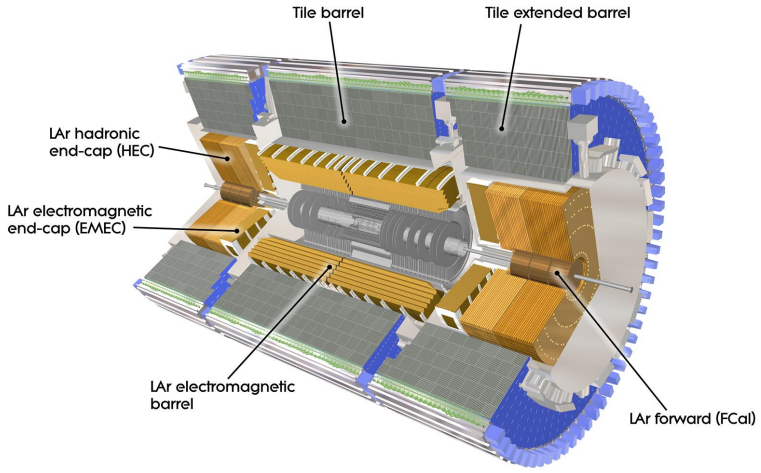

Figure 3.12: A schematic view of the calorimetry system [30].

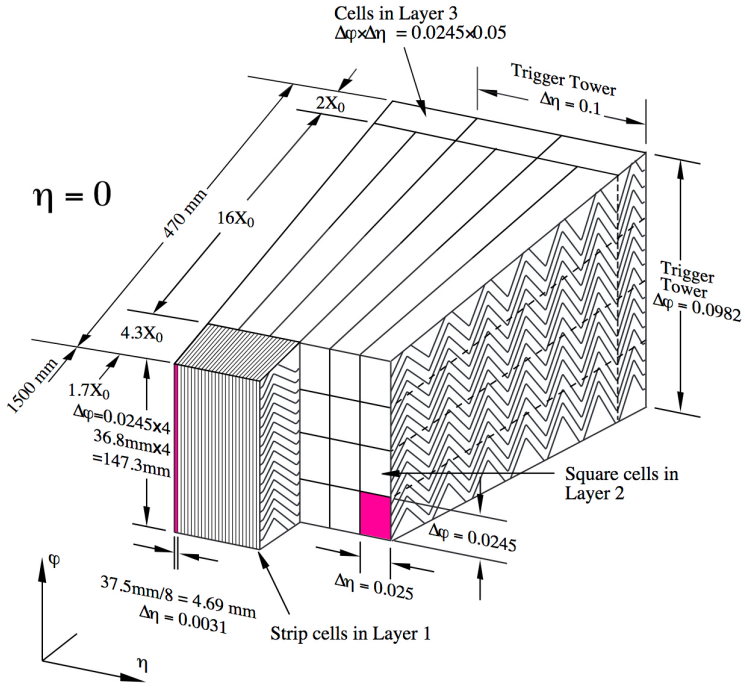

Figure 3.13: Sketch of a accordion structure for ECAL [27].

barrel region measured by the test beam [31] is

$$\frac{\sigma_E}{E} = \frac{10\%}{\sqrt{E(\text{GeV})}} \oplus 0.7\%. \tag{3.4}$$

In fact, the energy resolution in the electrons and photons obtained using LHC Run-2 data collected in 2015 and 2016 are given as follows [32]: for electrons with the energy of 10 GeV the typical resolution is 0.3% to 0.8% and it varies between 0.25% and 1% for photons with the energy around 60 GeV.

Hadronic calorimeter (HC)

The hadronic calorimeters cover the range $|\eta| < 4.9$ through different techniques for widely varying requirements and radiation environment over the large η range. The hadronic calorimeter is designed to measure the energy of hadrons, such as protons, neutrons and pions. The hadronic calorimeter consists of the barrel iron scintillating-tile calorimeter (Tile) HC covering $|\eta| < 1.7$ and endcap LAr HC covering $1.5 < |\eta| < 3.2$. Barrel Tile HC is segmented into three sections, the central barrel section ($|\eta| < 1.0$) and the two extended barrel sections ($1.0 < |\eta| < 1.7$), using different channel dimensions. The approximate 9.7 interaction length (λ) of active calorimeter in the barrel and 10λ or more in the endcap, is adequate to provide a good resolution for high energy jets. A module in the Tile HC is shown in Fig. 3.14. Together with the large η coverage, a good measurement of

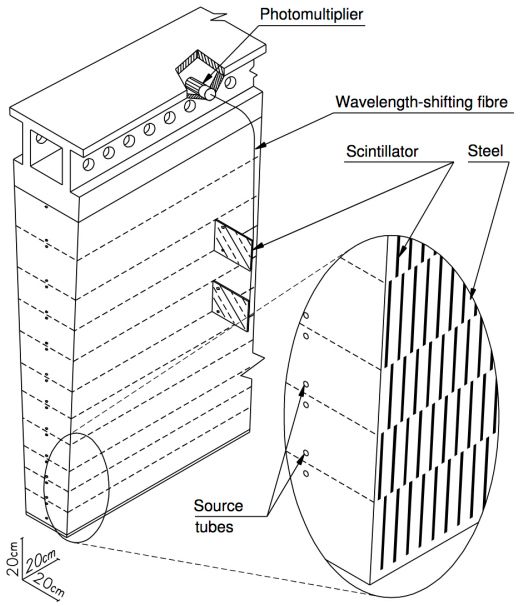

Figure 3.14: Sketch of a Tile HC module [27].

the missing transverse energy ($E_{\text{T}}^{\text{miss}}$) can be performed. The intrinsic resolution

of barrel Tile HC and endcap LAr HC for an individual hadron jet are given as follows:

$$\frac{\sigma_E}{E} = \frac{50\%}{\sqrt{E(\mathrm{GeV})}} \oplus 3\%, \qquad \text{(Tile HC)} \tag{3.5}$$

$$\frac{\sigma_E}{E} = \frac{100\%}{\sqrt{E(\mathrm{GeV})}} \oplus 10\%. \qquad \text{(Endcap LAr HC)} \tag{3.6}$$

In fact, the p_{T}-dependent jet energy resolution obtained using LHC Run-2 data collected during 2015 to 2017 is given as follows [33]: For jets with transverse momenta of 45 GeV that fall in the central calorimeter region ($|\eta| < 1.8$), the relative jet energy resolution is measured to be 16.2±2.8%.

Forward calorimeter

A set of LAr calorimeter layers are arranged in a very forward region close to the beam axis covering $3.1 < |\eta| < 4.9$. It is designed to capture the full content of jets or particles from hard scattering particles from extremely boosted center-of-mass. Forward calorimeter (FCAL) is made by three sampling layers in which both functions of EM calorimeter and hadronic calorimeter are integrated. The first layer is with copper absorber working as EM calorimeter, and the later two layers are with tungsten functioning as EM calorimeter. The overlap region with respect to the endcap HC is deliberated to realize smooth transition.

3.2.5 Muon Spectrometer

Muon spectrometers are located outermost in the ATLAS, consisting of four sub-detectors; Monitored Drift Tube (MDT); Cathode Strip Chamber (CSC); Resistive Plate Chamber (RPC); and the Thin-Gap Chamber (TGC). The former two are dedicated to precision measurement of muon tracks and the latter two are to triggering. Its role is to measure a muon momentum in the pseudorapidity range $|\eta| < 2.7$ and generate trigger on muons in the $|\eta| < 2.4$ region. The muon spectrometers can identify muons with momenta above 3 GeV and precise determination of p_{T} up to about 1 TeV with 10% momentum resolution. In particular, the relative momentum resolutions with the muon spectrometers in the barrel and the endcap regions [34] are:

$$\frac{\sigma_{p_{\mathrm{T}}}}{p_{\mathrm{T}}} = \frac{0.25(\mathrm{TeV})}{p_{\mathrm{T}}} \oplus 3.27\% \oplus 0.168(\mathrm{TeV}^{-1}) \times p_{\mathrm{T}} \qquad \text{(Barrel)} \tag{3.7}$$

$$\frac{\sigma_{p_{\mathrm{T}}}}{p_{\mathrm{T}}} = 3.79\% \oplus 0.196(\mathrm{TeV}^{-1}) \times p_{\mathrm{T}} \qquad \text{(Endcap)} \tag{3.8}$$

The cross-sections in the plane containing the beam axis is shown in Fig. 3.15. In

the barrel region, three cylindrical layers around the beam axis to measure tracks are installed. In the transition and endcap regions, three layers of the chambers are placed perpendicular to the beam axis.

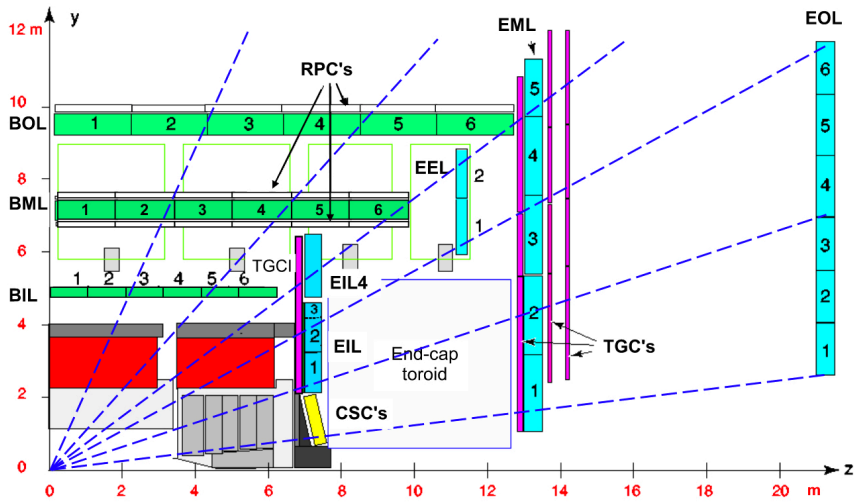

Figure 3.15: The schematic view of the cross-section of the muon system [27]. Infinite momentum muons would propagate along straight trajectories which are shown by the dashed lines and typically traverse three muon stations.

Monitor Drift Tubes (MDT)

MDT is a gaseous drift chamber filled with the basic detection elements of 30 mm diameter aluminum tubes that are covered by a 400 μm thick wall. Drifting electrons are absorbed by a 50 μm diameter tungsten-Rhenium wire in the center of a tube with a bias voltage of 3080 V is applied, and read out by a low-impedance current sensitive preamplifier. The gas mixture is with Ar (93%) and CO_2 (7%), maintaining the maximum drift time of 700 ns. The position resolution by a single wire is about 80 μm. It is the precision momentum measurement chamber covering the pseudorapidity range of $|\eta| < 2.7$. It consists of multi-layers of almuminum tubes with the structure shown in Fig. 3.16. The limitation in the η-coverage is determined by its maximum durable rate (150 $\mathrm{cm^{-1}s^{-1}}$).

Cathode Strip Chamber (CSC)

For high particle fluxes and track density in the forward region of the pseudorapidity of $2.0 < |\eta| < 2.7$, a multiwire proportional chamber CSC is used for the innermost tracking layer since it has higher rate capability and time resolution (7 ns). It is operated with a gas mixture of Ar (80%) and CO_2 (20%) and with a bias voltage of 1900 V applied. The CSC can stand high rate operation up to

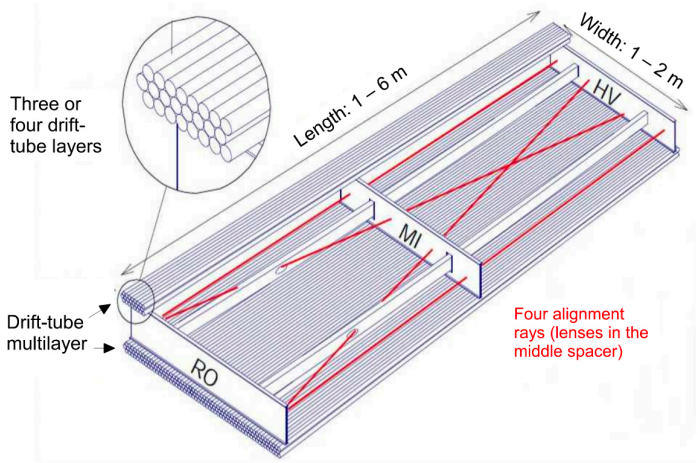

Figure 3.16: The mechanical structure of a MDT chamber [27].

1000 Hz/cm^2 while the limit of the safe operation of the MDT is about 150 Hz/cm^2. The posistion resolution of the CSC is 40 μm in r-direction.

Resistiv Plate Chamber (RPC)

RPC is digital gaseous detectors specialized in fast timing response for triggering. RPC is placed in the barrel region of the pseudorapidity $|\eta| < 1.05$ as shown in Fig. 3.15. The elementary detection unit is a gas gap filled with non-flammable gas mixture (94.7%: $C_2H_2F_4$, 5%: Iso-C_4H_{10}, 0.3%: SF_6). An uniform high electric field (∼4900 V/mm) is applied so that the ionized electrons amplitude by themselves via the avalanches. Signals are read out by a metal strip attached on both ends of the gaps, arranged with a pitch of 30 mm ∼ 39.5 mm. The typical spatial and timing resolution achieved by a RPC chamber are 1 cm and 2 ns respectively.

Thin Gap Chamber (TGC)

TGC covers the pseudorapidity range of $1.05 < |\eta| < 2.7$. It is multiwire proportional chamber, shown in Fig. 3.17. A quick drain of secondary electrons is achieved by the quenching gas mixture of CO_2 (55%) and n-C_5H_{12} (n-pentane) (45%), yielding the timing response of 5 ns. In order to get good time resolution, wire-to-cathode distance of 1.4 mm is smaller than the wire-to-wire distance of 1.8 mm. TGC has good granularity for muon p_T discrimination for trigger.

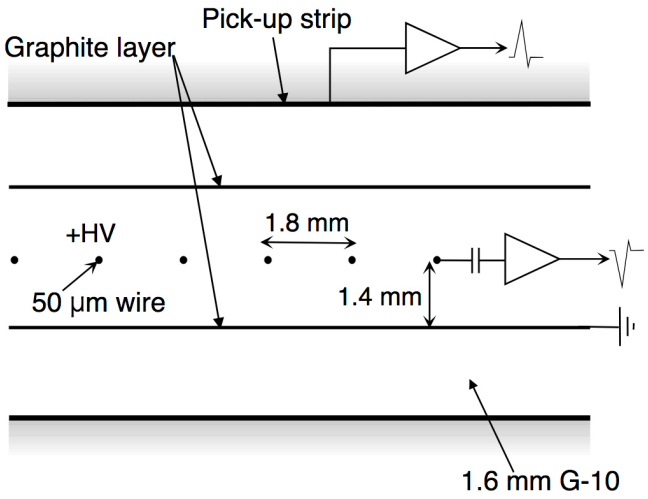

Figure 3.17: TGC structure in the plane orthogonal to the wires. There are anode wires, graphite cathodes, G-10 layers and a pick-up strip [27].

3.3 Trigger and data acquisition system (TDAQ)

The ATLAS Trigger and Data Acquisition System (TDAQ) [27] is designed to effectively collect as various interesting events as possible using two trigger levels, Level-1 (L1) and High Level Trigger (HLT). The first level hardware-based L1 trigger uses a subset of the detector information to reduce the rate of accepted events to a design maximum of 100 kHz. This is followed by a software-based HLT system performed on a computer farm with a maximum average accepted event rate of about 1 kHz. The schematic of the readout streams are shown in Fig. 3.18.

Level-1 (L1) Trigger

The hardware based L1 trigger selects events from 40 MHz to 100 kHz by signals from the calorimeters and muon detectors. The signals are processed by dedicated hardware to meet the requirement of the maximum latency of 2.5 μs. The L1 consists of two independent sub-trigger systems (Fig. 3.18); L1 Calo identifying the EM or hadronic clusters in calorimeter and reconstruct primitive jets, electrons, photons and taus (L1 objects) with calibrated energy in EM scale; L1 Muon identifying and measuring the tracks in the muon spectrometer designed to accept events with muons. The object reconstruction is based on the coarsely segmented blocks of combined detector channel called "trigger tower" with $\eta \times \phi$ granularity of 0.1×0.1. Missing transverse momentum $E_{\mathrm{T}}^{\mathrm{miss}}$ is also calculated at the L1 stage by the vectoral sum of the calorimeter deposits, referred as L1XE. Trigger accept is issued by the Central Trigger Processors (CTP) when the L1 objects meet certain criteria in terms of p_{T} threshold and number of objects. The information about the geometric position of trigger objects is retained in the calorimeter and muon

trigger processor until the trigger decision is made. This information is called as Region-of-Interest (RoI), and sent to the HLT when the L1 trigger is accepted. To suppress pile-up effects by auto-correlation filters and pedestal correction, the preprocessor of calorimeters were replaced to FPGA from ASIC for Run-2. A new topological trigger processor (L1Topo) system enables the L1 trigger to add object's kinematics from hardware base information. The muon endcap trigger requires the coincidence with hits from the innermost muon chamber to suppress most of the fake muon triggers [35].

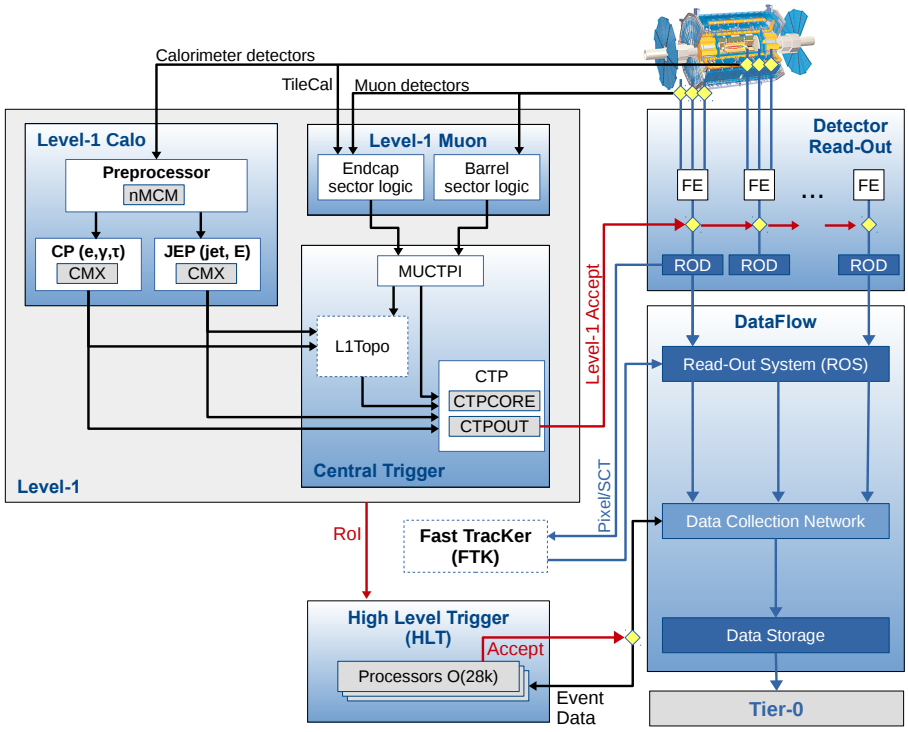

Figure 3.18: The schematic of ATLAS trigger system in Run-2 [35]. Trigger detectors have separated readout line for trigger, sending input information for trigger decision to CTP. The CTP reconstructs L1 objects and issue a global accept signal relieving the buffered data, once the trigger criteria are satisfied.

High Level Trigger (HLT)

The software based HLT selects and records events from output of the L1 trigger to 1 kHz. HLT uses software to discard non-interesting events by refining the

reconstruction of physics objects, such as electron, muon, and jet, found in the angular RoI identified by the L1 trigger. A seed is constructed for each trigger accepted by L1, which consists of a p_{T} threshold and an η-ϕ position. This is performed by a set of custom farmwares with a processing time of 0.2 s on an average. The final accepted event rate is reduced to ∼1.5 kHz. In this thesis, the event is required to pass the lepton trigger, as shown in Sec. 6.1. More details are mentioned in the reference [36].

3.4 Luminosity measurement

Luminosity determination is particular important since it gives the reference of normalizing simulated dataset which enables the comparison to data. The instantaneous luminosity is calculated as the formula below:

$$\mathcal{L} = \frac{\mu n_b f_b}{\sigma}, \tag{3.9}$$

where n_b is the number of colliding bunches and f_b is the frequency of the beam circulation. σ is total fiducial cross-section of proton-proton interaction including both elastic and inelastic scattering, and μ is the average number of such interaction per bunch crossing. While σ is provided by a dedicated calibration (Van der Meer scan [37]) measuring the lateral beam profile using overlapping two beams, μ is obtained directly by exploiting the rate information from luminosity detectors located in the very forward region nearby the beam pipe. Dedicated calibration and luminosity determination algorithm studied in the reference [38]. Two luminosity detectors mainly contribute to the luminosity measurement: LUminosity measurements using Cerenkov Integrating Detector (LUCID) and Absolute Luminosity For ATLAS (ALFA). LUCIDs are located at the both ends of the ATLAS detector at a distance of 17 m from the IP, covering the pseudorapidity range $5.6 < |\eta| < 6.0$. The LUCID detector consists of 16 aluminum tubes filled with C_4H_{10} gas filled inside, designed to count the Cherenkov photons kicked out by charged particles flying along the beam axis which are mainly generated by proton-proton inelastic scattering in the IP. ALFA is located beyond the ATLAS envelope at $z = \pm 240$ m, sandwiching the beam pipe from top and bottom. The detectors are composed of 8 scintillating fibers, designed to measure the elastic scattering component of the proton-proton interaction. The luminosity has been measured with a precision of 2.1∼2.4% for the data acquired in 2015-2017.

Chapter 4

Data and simulated samples

This chapter explains about the data and simulated samples. The data were collected by the ATLAS detector as described in Chapter 3. The simulated samples using Monte Carlo (MC) method are also described, which are used to predict the signal and background productions.

4.1 Data sample

The analysis uses the complete dataset collected in 2015, 2016 and 2017 at $\sqrt{s} =$ 13 TeV with the ATLAS detector, with total integrated luminosity of 79.7 fb^{-1} after requirement on good reconstructed physics objects. The uncertainty in the combined 2015-2017 integrated luminosity is 2.0%. It is derived, following a methodology similar to that detailed in the reference [39], from calibrations of the luminosity scale using x-y beam separation scans performed in August 2015, May 2016 and July 2017. Due to large inelastic cross-section of proton-proton interaction and high luminosity of LHC, a large number of pp interactions, mostly 'soft' interactions, occur in each bunch crossing called pile-up. Number of pp interactions per crossing depends on the total instantaneous machine luminosity L and the number of colliding bunches per beam N_{bunch}. Mean number of interactions $< \mu >$ is provided by:

$$< \mu >= \frac{L \times \sigma_{\text{in}}}{N_{\text{bunch}} \times f_{\text{LHC}}} \tag{4.1}$$

where σ_{in} is the total inelastic proton-proton cross-sections (80 mb), and f_{LHC} is the bunch revolution frequency in LHC (about 11 kHz). Effects of pile-up on event reconstruction arise for example from overlapping calorimeter clusters (called "in-time pile-up"). On the other hand, influence of detector signals from previous bunch crossings can affect the signal of a triggered event (called "out-of-time pile-up"). Pile-up events are implemented in the Monte Carlo (MC) simulation. (see detail in Sec. 4.2)

4.2 Simulated sample

Number of physics processes related to this thesis are simulated using generators, which simulates the final state particles of given physics processes according to certain theoretical models. It uses MC technique in generating events. MC simulation is a highly powerful toolkit providing theoretical prediction on event kinematics as well as the detector response, which is used extensively from studying signal and background separation, performance evaluation to background estimation. In theoretical calculations, the models of hard collisions use perturbative QCD calculation at a finite order of the QCD coupling constant α_S, which is called Matrix Element (ME) part. The generated a few partons subsequently are fragmented into more number of partons by Parton Shower (PS) algorithm. The many partons are finally hadronized into many hadrons using phenomenological models. The general structure of a simulated event is shown in Fig. 4.1. These events subsequently

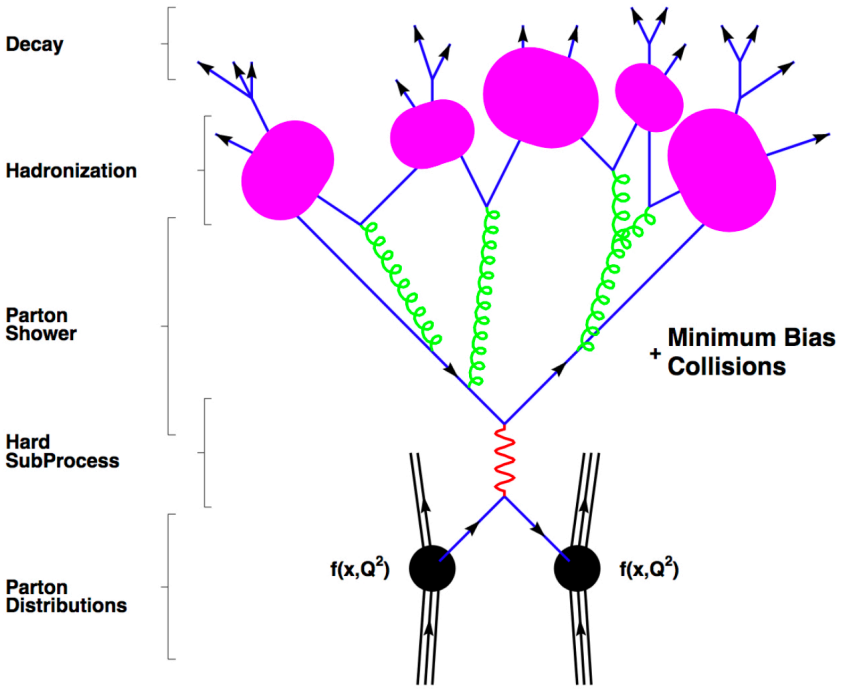

Figure 4.1: The schematic of a showering and hadronization generator event [40].

undergo the detector simulation with the GEANT4 package [41], which are used to estimate the systematic uncertainty of the signal modelling. GEANT4 is a toolkit to simulate how particles interact in a matter. This is used to describe the ATLAS detector components and material distributions and simulate energy deposits in the detectors. Pile-up is implemented by overlaying a certain number of simulated 'soft' (minimum bias) events on the 'hard' event. The number of pile-up events are distributed according to the expected luminosity profile of the data sample. The difference of $< \mu >$ distribution in the MC sample and the real

data is taken into account by reweighting the MC events.

The generators used in this thesis are described as below.

Pythia

An event generator tool for the high-energy collisions whose process starts from hard process in the initial states, then generate multiple interactions of partons, beam remnants, string fragmentation and particle decays. The showering model is expected to match the theoretical description of QCD showers at the Leading Order (LO). It is used the difference between POWHEG and aMC@NLO for Matrix Element calculation (ME).

Herwig

This generator reproduces hard processes, parton showering and QCD effects at the LO. It simulates angular ordered parton shower and the hadronization process is modeled by cluster fragmentation. It is used in combination with the POWHEG for parton showering and hadronization.

Powheg

Generate the hardest emission with positive weight event of the Next to Leading Order (NLO) corrections. This is the extensions of the shower algorithms. It is used the difference between PYTHIA and HERWIG for parton showering and hadronization.

aMC@NLO

It provides matching calculation for QCD process with a parton showering in the hadronization. To avoid double counting events which come from NLO calculation, the events are provided negative weight as well as positive weight. It is used in combination with between PYTHIA for Matrix Element calculation (ME).

Sherpa

Event generator for simulation of high energy reactions of particles. It simulate better for final states with large number of isolated jets than PYTHIA and HERWIG. It is used in the background contribution from the Diboson production, and the associated production of W and Z boson with heavy flavour jets.

MadGraph

It is the matrix element generator for parton level simulation and is used for rare standard model processes. QCD shower and hadronization are simulated by PYTHIA. It is used in the background contribution from the rare standard model processes.

The nominal simulated signal $t\bar{t}$ sample is generated at the NLO using the POWHEG [42] generator, interfaced to PYTHIA8 [43] for parton showering and hadronization with h_{damp} parameter set to $1.5m_t$. In this case the fast-simulation package ATLFAST2 [44] (AFII) is used instead. This is based on a parametrization of the performance of the electromagnetic and hadronic calorimeters measured in the test-beam or in the GEANT4. The difference between the full simulation (Full) is covered to be marginal after examining a number of reference signal points. The subsequent procedures are identical to what is processed for the data sample. To estimate the effect of the matrix element systematic uncertainty, the nominal sample is compared to the one generated using AMC@NLO [45] and the parton shower uncertainty is estimated by comparing PYTHIA8 to HERWIG7 [46].

4.2.1 Signal and background samples

Processes with top pair production and additional bosons produced with AMC@NLO for hard scattering and Pythia8 for parton shower and hadronization. The detailed list of signal $t\bar{t}$ samples used in this analysis is shown in Table. 4.1 with their theoretical cross-sections and k-factors, the ratio of the NLO to LO cross section for a given process.

Filter	Generator	cross-section(pb)	K-factor	Simulation
	$t\bar{t}$ nominal samples			
dilep filt.	Powheg+Pythia8	76.95	1.1398	Full
non all had	Powheg+Pythia8	396.87	1.1398	Full
	$t\bar{t}$ alternative samples			
dilep filt.	Powheg+Pythia8	76.95	1.1398	AFII
non all had	Powheg+Pythia8	396.87	1.1398	AFII
dilep filt.	Powheg+Pythia8 $h_{\text{damp}} = 3.0m_t$	76.94	1.1398	AFII
non all had	Powheg+Pythia8 $h_{\text{damp}} = 3.0m_t$	320.01	1.1398	AFII
dilep filt.	AMC@NLO+Pythia8	76.316	1.1681	AFII
SingleLep	AMC@NLO+Pythia8	313.275	1.1691	AFII
dilep filt.	Powheg+Herwig7	77.00	1.1391	AFII
non all had	Powheg+Herwig7	320.112	1.1392	AFII

Table 4.1: Summary of the signal MC samples.

The background samples represent different physics processes, which have similar decay products as the $t\bar{t}$ signal and thus can also pass the $t\bar{t}$ selection criteria. The background consisting of single top events is produced with Powheg+Pythia8, where the W boson from top quark decays leptonically. The backgrounds from the Diboson production are estimated using Sherpa 2.2.1 samples. Leptonic decays of vector bosons produced in association with jets, referred to as W+jets and Z+jets, are considered and Sherpa 2.2.1 is used as generator. Rare SM processes with top pair production and additional bosons are included and much small background contribution. Table 4.2 shows summary of the background samples. The detail of the background sources is shown in Sec. 6.2.

Filter	Generator	Cross-section(pb)	K-factor	Simulation
Single top				
t-ch_top	Powheg+Pythia8	36.993	1.00	Full
t-ch_antitop	Powheg+Pythia8	22.175	1.00	Full
Wt_inclusive_top	Powheg+Pythia8	37.936	0.945	Full
Wt_inclusive_antitop	Powheg+Pythia8	37.906	0.946	Full
s-ch_top	Powheg+Pythia8	2.0268	1.015	Full
s-ch_antitop	Powheg+Pythia8	1.2676	1.015	Full
W+jets				
$W \to \mu\nu$	Sherpa2.2.1	20472.488	0.9702	Full
$W \to e\nu$	Sherpa2.2.1	20476.908	0.9702	Full
$W \to \tau\nu$	Sherpa2.2.1	20507.226	0.9702	Full
Z+jets				
$Z \to \mu\mu$	Sherpa2.2.1	2138.730	0.9751	Full
$Z \to ee$	Sherpa2.2.1	2137.697	0.9751	Full
$Z \to \tau\tau$	Sherpa2.2.1	2138.015	0.9751	Full
Z+jets – low mass (10 GeV $< m(ll) <$ 40 GeV)				
$Z \to \mu\mu$	Sherpa2.2.1	2465.673	0.9751	Full
$Z \to ee$	Sherpa2.2.1	2466.284	0.9751	Full
$Z \to \tau\tau$	Sherpa2.2.1	2468.6697	0.9751	Full
Diboson				
1 lepton	Sherpa2.2.1	15.564	0.27976	Full
1 lepton	Sherpa2.2.1	15.563	0.13961	Full
1 lepton	Sherpa2.2.1	159.104	1.00	Full
2 and 3 leptons	Sherpa2.2.1	0.60154	1.00	Full
Rare standard model processes				
$t\bar{t}W$	aMC@NLO+Pythia8	0.5483	1.10	Full
$t\bar{t}Z \to \nu\nu$	aMC@NLO+Pythia8	0.15499	1.11	Full
$t\bar{t}Z \to q\bar{q}$	aMC@NLO+Pythia8	0.52771	1.11	Full
$t\bar{t}ee$	aMC@NLO+Pythia8	0.036888	1.12	Full
$t\bar{t}\mu\mu$	aMC@NLO+Pythia8	0.036895	1.12	Full
$t\bar{t}\tau\tau$	aMC@NLO+Pythia8	0.036599	1.12	Full
$t\bar{t}H$ (1 lepton)	Powheg+Pythia8	0.22276	1.00	Full
$t\bar{t}H$ (dilepton)	Powheg+Pythia8	0.05343	1.00	Full
tZ	MadGraph5+Pythia8	0.24037	1.00	Full
tWZ (DR)	aMC@NLO+Pythia8	0.016046	1.00	Full

Table 4.2: Summary of the background processes.

Chapter 5

Object definition

Particles originating from the proton-proton collisions are reconstructed by combining information from various subdetectors. These reconstructed elements are used in the ATLAS experiment, and called as "object". This chapter describes definition for the physics objects, which include electrons, muons, jets, and missing transverse momentum ($E_{\mathrm{T}}^{\mathrm{miss}}$). The $t\bar{t}$ charge asymmetry can be measured by two charged leptons, two b-tagged jets and $E_{\mathrm{T}}^{\mathrm{miss}}$ from $t\bar{t} \to W^+bW^-\bar{b} \to l^+\nu_l b l^-\bar{\nu}_l\bar{b}$ process.

5.1 Primary vertices

The reconstructed tracks come from points in an bunch collision, indicating "primary vertices". A primary vertex has at least two charged tracks reconstructed by the inner detector (ID). The tracks can be clustered according to the z position at the beam line.

For hard-scatter physics processes including $t\bar{t}$ pair production by proton-proton collision, it is necessary to identify the hard-scatter primary vertex as the primary vertex with the highest $\sum p_{\mathrm{T,\,track}}^2$, where $p_{\mathrm{T,\,track}}$ is the transverse momentum of track associated to the vertex, is chosen.

5.2 Electrons

An electron is reconstructed [47] based on a cluster in the electromagnetic calorimeter, which is associated to a charged track reconstructed in the ID. To reject backgrounds while keeping high efficiency for prompt electrons (such as $W \to e\nu$), electron identification algorithms are based on discriminating variables. Here, backgrounds means mis-identified hadronic jets as well as electrons form semileptonic heavy-flavour hadron decays, Dalitz decays and photon conversion. The technique is multivariate analysis(MVA) using a likelihood(LH) [48]. The electron LH makes

use of signal and background probability density functions(PDFs) of the discriminating variables. Signal and background PDFs used for the electron LH identification are obtained from data.
In this analysis, the `TightLH` electron identification criteria are used to identify the signal electrons from W boson decays.

In addition to the identification criteria described above, isolation is required to select electrons from W boson decays. The isolation variables quantify the energy of the particles produced around the electron candidate. The `Gradient` isolation is applied for the signal electrons. In case of `Gradient` isolation, the combined calorimeter and tracker isolation leads to an signal electron reconstruction efficiency of 90% at $p_{\mathrm{T}} = 25$ GeV and 99% at $p_{\mathrm{T}} = 60$ GeV [48].

On the other hand, loose `MediumLH` criteria without isolation requirement is used to estimate the contribution from fake electrons.

5.3 Muons

Unified muon identification chain [49], which combines information from the inner detector and the muon spectrometer(MS), is used to reconstruct muons. Muon identification is performed by applying quality requirements that suppress background, mainly from pion and kaon decays ($\pi, K \to \mu\nu$), while selecting prompt muons (such as $W \to \mu\nu$) with high efficiency. To guarantee a robust momentum measurement, specific requirements on the number of hits in the ID and MS are used. For the ID, the quality cuts require at least one Pixel hit, at least five SCT hits, fewer than three Pixel or SCT holes, and that at least 10% of the TRT hits originally assigned to the track are included in the final fit; the last requirement is only employed for $|\eta|$ between 0.1 and 1.9, in the region of full TRT acceptance.
The `Medium` identification criteria provide the selection as signal muons from W boson decays. This selection minimizes the systematic uncertainties associated with muon reconstruction and calibration.

To develop algorithms to define muon isolation quantities using calorimeters, tracker tracks, etc. for different types of muon candidates, the muon isolation is applied. In this thesis, the `Gradient` isolation is applied, same as in the case of electrons.

5.4 Jets

Jets are reconstructed from clustered energy deposits in the electromagnetic and hadronic calorimeters. The anti-k_t algorithm [50] is used to reconstruct jets from topological calorimeter clusters [51]. Truth muons are added to the four momentum of the truth jet if they are within radius parameter $R < 0.4$. This is

because the generator level jets are electro-magnetic topoclusters(EMTopo). The EMTopo scheme is used for jet calibration. Jets are accepted within $|\eta| < 2.5$.

5.4.1 B-tagging

A multivariate MV2 algorithm [52] is used to identify b-jets initiated by b quark. A Schematic of the production of a b-jet is shown in Fig. 5.1. The b-tagging algorithms identify displaced vertices formed by tracks in the cones of reconstructed jets, taking advantage of the large mass (5 GeV) and long lifetime (1.5 ps) of b-hadrons in the b-jets. This gives rise to a displaced secondary vertex which is a key signature of a b-hadron decay. In this analysis, results from three standalone b-tagging algorithms Secondary Vertex Finding (SV1), Decay Chain Multi-Vertex Algorithm (JetFitter) and Impact Parameter based Algorithm (IP3D) [52] are combined using the boosted decision tree (BDT) algorithm. In this analysis, a MV2c10 algorithm is used, where the threshold c10 is defined that the background sample consists of 10% (90%) c-(light-flavour) jets. The light-flavour jet rejection for 77% b-jet efficiency working point is used. The corresponding rejection factors for jets initiated by a c quark, tau lepton, and light quark are 4, 16, and 113, respectively.

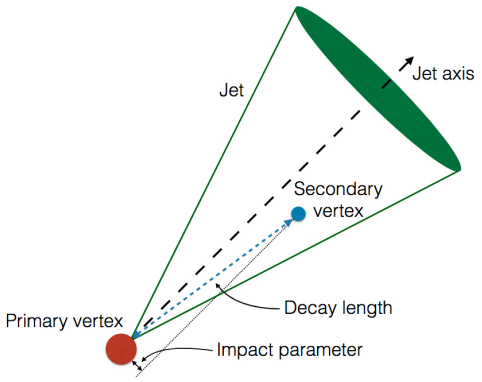

Figure 5.1: Illustration of the production of a b-jet [53]. A displaced secondary vertex is identified as a b-jet. It is dedicated the decay length in the plane transverse to the beamline and the impact parameter for one of the tracks.

5.4.2 Pile-up

During 2017 data-taking, there was a mean of approximately 20 interactions per bunch crossing. There is therefore potentially a large contamination from non-hard scatter pile-up interaction. The energy deposits from these pile-up interactions in the calorimeters can be reconstructed into jets. The Jet Vertex Fraction (JVF) [54] is defined as the summed scalar p_{T} of the tracks associated with both the jet and

the primary vertex divided by the summed scalar p_{T} of all tracks in the jet. The Jet Vertex Tagger (JVT) [54] is a tool identifying jets derived from hard-scatter vertices except pile-up jets using the JVF. In particlular, the JVT algorithm is used to reject low-p_{T} pile-up jets. The discriminant is required to be larger than 0.59 for jets with $p_{\mathrm{T}} < 60$ GeV.

5.5 Missing transverse momentum

The missing transverse momentum vector $\boldsymbol{p}_{\mathrm{T}}^{\mathrm{miss}}$ with magnitude $E_{\mathrm{T}}^{\mathrm{miss}}$ is calculated from a vector sum of $\boldsymbol{p}_{\mathrm{T}}$ of reconstructed objects. Tracks and calorimeter cells without any associated object are also considered.
The primary sources of uncertainty related to the $E_{\mathrm{T}}^{\mathrm{miss}}$ come from the scale and resolution of the objects which the $E_{\mathrm{T}}^{\mathrm{miss}}$ is reconstructed from and the description of additional calorimeter energy from pile-up events. The overall systematic uncertainty related to $E_{\mathrm{T}}^{\mathrm{miss}}$ is obtained using the uncertainty in scale and resolution of the charged leptons, jets.

5.6 Overlap removal

In order to avoid double counting of single final state objects, overlap removal procedure between electrons, muons and jets is implemented [55] as a sequence of operations:

- Electron candidates sharing a track with a muon candidate are removed.
- If the distance between a jet and a baseline electron is $\Delta R < 0.2$ the jet is dropped. If multiple jets are found with this requirement, only the closest one is removed.
- If the distance in between a jet and a baseline electron is $0.2 < \Delta R < 0.4$ the electron is dropped.
- If the distance between a jet and a baseline muon is $\Delta R < 0.4$, then: If the jet has more than 2 associated tracks the muon is dropped, otherwise the jet is removed.

Chapter 6

Event reconstruction

This chapter, the selection criteria used in the measurement are summarized. The physics objects in the analysis is explained as described in chapter. 5. The selections applied to leptons, jets, $E_{\mathrm{T}}^{\mathrm{miss}}$. In dilepton channels ($ee$, $e\mu$, and $\mu\mu$), the number of signal and background events is expected and shown in event yields. In dileptonic events, two neutrinos are produced and escape undetected. Thus, an underconstrained system is obtained. To reconstruct the top and antitop quark momenta, precise reconstruction of the $t\bar{t}$ kinematics is required.

6.1 Selecton criteria

Signatures of the events for the dilepton channel are two oppositly isolated charged leptons and two b-jets. Events are separated into three channels according to lepton flavor; either exactly one electron and one muon ($e\mu$ channel), or two same-flavor leptons (ee and $\mu\mu$ channels). The following selection criteria are used in all channels:

- **Event quality** – to avoid events affected by detector noise the `GoodCalo` criteria must be fullfilled. Any event with at least one jet flagged as `LooseBad` is rejected. Single electron and muon trigger are required, at least one of the triggers must be fired.

- **Lepton selection** – exactly two high-p_{T} charged leptons; one charged lepton with $p_{\mathrm{T}} > 28$ GeV and one additional charged lepton with $p_{\mathrm{T}} > 25$ GeV. The leptons are required to be of opposite electric charge and at least one of the leptons must be matched to the following trigger: Data 2015:
  e: `HLT_e24_lhmedium_L1EM20VH`, `HLT_e60_lhmedium`, `HLT_e120_lhloose`
  μ: `HLT_mu20_iloose_L1MU15`, `HLT_mu50`
  Data 2016 and 2017:
  e: `HLT_e26_lhtight_nod0_ivarloose`, `HLT_e60_lhmedium_nod0`, `HLT_e140_lhloose_nod0`
  μ: `HLT_mu26_ivarmedium`, `HLT_mu50`

- **Jets** – At least 2 jets with $p_{\mathrm{T}} > 25$ GeV are required. At least 1 b-tagged jet is required. The events are categorized into 1 b-tag exclusive (1-b excl.) and 2 b-tag inclusive (2-b incl.) regions according to the b-jet multiplicity.

In ee and $\mu\mu$ channels, the largest contribution to the background comes from the associated production of Z boson with heavy flavour jets, so following criteria are required;

- Z **veto** – The reconstructed invariant mass of the dilepton system is required to be outside of Z boson mass window ($|m_{ll} - m_Z| > 10$ GeV).

- **Drell-Yan process veto** – The reconstructed invariant mass of the dilepton system is required $m_{ll} > 15$ GeV for rejecting the production of Z boson through the Drell–Yan process. Moreover, to avoid large uncertainties from mismodeling the $E_{\mathrm{T}}^{\mathrm{miss}}$ distribution, $E_{\mathrm{T}}^{\mathrm{miss}}$ is required to be larger than 20 GeV.

6.2 Predicted signal and background events

To predict signal and background contributions after applying the selection criteria, several MC event generators are used. The background contribution in this measurement comes from the associated production of Z boson with heavy flavour jets, single top production associated with a W boson and prompt leptons from W,Z boson. Moreover, the background arising from misidentified and nonprompt leptons as "Fakes" is determined using both MC simulated samples and data. This contribution is estimated using MC simulated samples, modified with corrections derived from data. In background estimation from the associated production of Z boson with heavy flavour jets and Fakes, they require a scaling factor due to difficulty of MC modelling the data in the ee and $\mu\mu$ channels. In detail of each background estimation, it is shown in the reference [56].

6.2.1 Event yield in $e\mu$ channel

In $e\mu$ channel, the background contamination is much smaller than ee and $\mu\mu$ channels. The event yields after selection criteria are estimated as shown in Table. 6.1. The number of events in $e\mu$ channel is the largest among three channels. The dominant background contribution comes form single-top production (single top production associated with a W boson). The physcis objects after selection are shown as the plots in signal region. For example, in case of $e\mu$ 1 b-tag exclusive, the corresponding plots are estimated as shown in Fig. 6.1-6.3. The distribution of these properties(individual lepton, dilepton, jets, and $E_{\mathrm{T}}^{\mathrm{miss}}$) are consistent with the data and MC predictions.

Process:	$e\mu$ channel	
	1 b excl.	2 b incl.
$t\bar{t}$	116710±128	136327±135
$t\bar{t}$ (other final state)	13559±44	15218±46
Single top	7506±39	3099±25
Diboson	435±5	33±1
Z + jets	398±38	50±6
Rare SM ($t\bar{t}V$, $t\bar{t}H$, etc)	289±2	430±3
Fakes	167±13	50±5
Total Prediction	139065±146	155208±144
Data (79.7 fb^{-1})	140839	157055

Table 6.1: Event yields in the dilepton topology, $e\mu$ channel split by b-tag multiplicity (1-b excl., 2-b incl.). Presented uncertainties include statistical and systematic uncertainties. No fake lepton calibration factor is applied here.

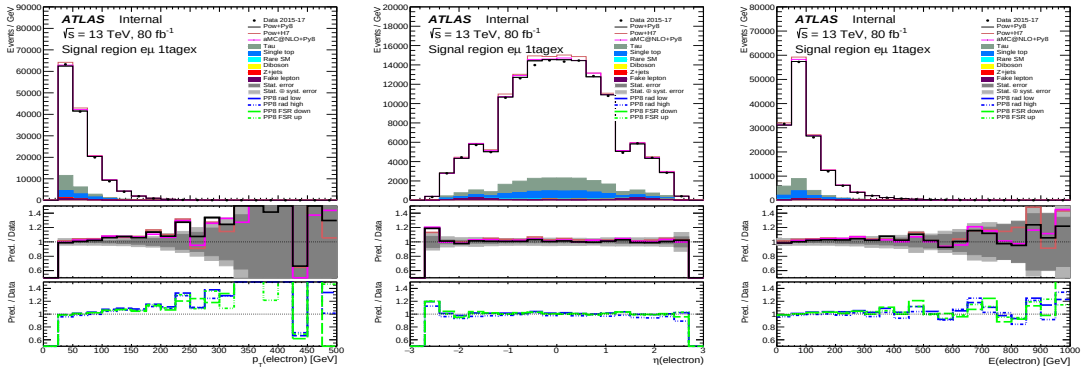

(a) Electron p_{T} (b) Electron η (c) Electron energy

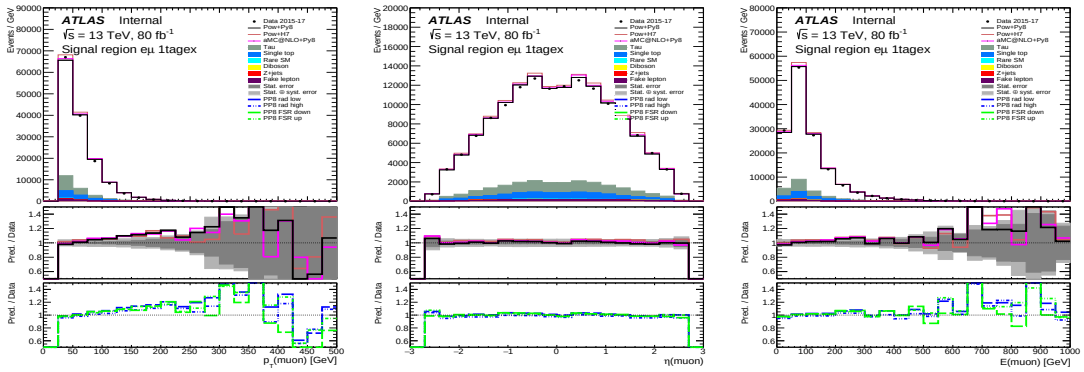

(d) Muon p_{T} (e) Muon η (f) Muon energy

Figure 6.1: A comparison of the observed data and prediction for the individual lepton properties in the $e\mu$ 1-b excl. channel. The bottom panels show the ratio of MC to data predictions.

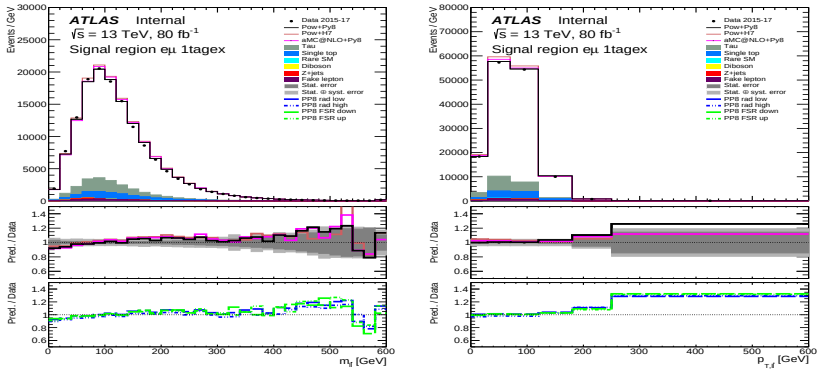

(a) Dilepton invariant mass, $m_{l\bar{l}}$ (b) Dilepton transverse momentum, $p_{T,l\bar{l}}$

Figure 6.2: A comparison of the observed data and prediction for the dilepton properties in the $e\mu$ 1-b excl. channel. The bottom panels show the ratio of MC to data predictions.

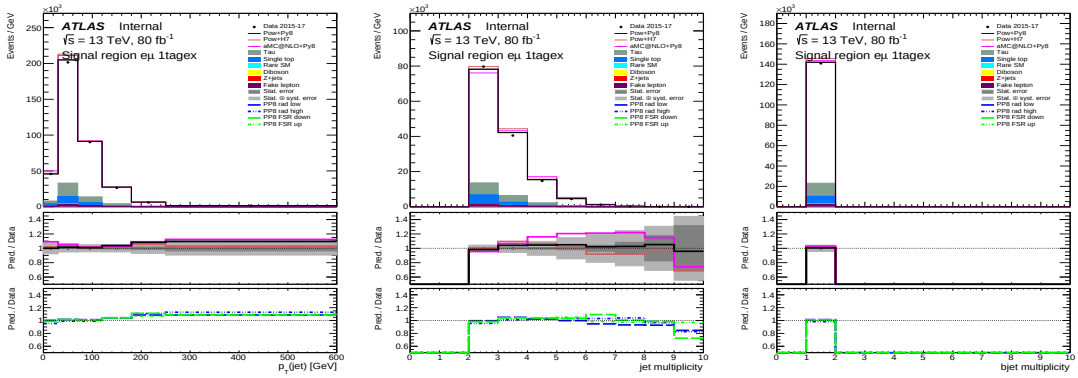

(a) Jet p_{T} (b) Jet multiplicity (c) b-jet multiplicity

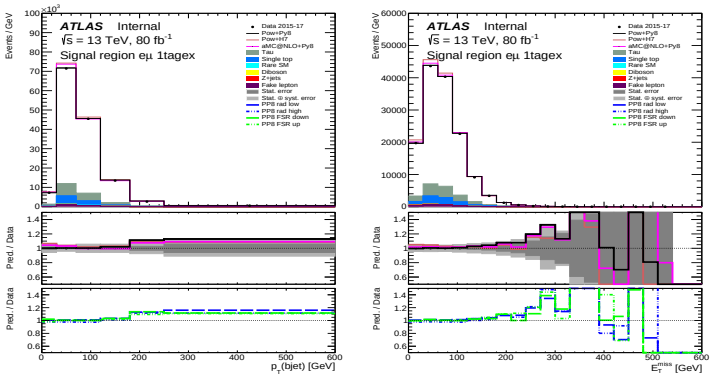

(d) b-jet p_{T} (e) $E_{\mathrm{T}}^{\mathrm{miss}}$

Figure 6.3: A comparison of the observed data and prediction for the jet and $E_{\mathrm{T}}^{\mathrm{miss}}$ properties in $e\mu$ 1-b excl. channel. The bottom panels show the ratio of data to MC predictions.

6.2.2 Event yield in ee channel

The event yields after selection criteria are estimated as shown in Table. 6.2. The largest background contribution comes from the associated production of Z boson with heavy flavour jets. For example, in case of ee 1 b-tag exclusive, the corresponding plots are estimated as shown in Fig. 6.4. In ee channel, the MC predictions are consistent with data event.

Process:	ee channel	
	1 b excl.	2 b incl.
$t\bar{t}$	40954±76	51361±83
$t\bar{t}$ (other final state)	5333±28	6363±27
Single top	2652±23	1162±15
Diboson	198±3	24±1
Z + jets	6632±249	1019±111
Rare SM ($t\bar{t}V$, $t\bar{t}H$, etc)	114±2	174±2
Fakes	324±36	73±6
Total Prediction	56206±266	60176±143
Data (79.7 fb^{-1})	59235	61519

Table 6.2: Event yields in the dilepton topology, ee channel split by b-tag multiplicity (1-b excl., 2-b incl.). Presented uncertainty include detector systematics, background normalization and statistical uncertainty. No fake lepton calibration factor is applied here.

6.2.3 Event yield in $\mu\mu$ channel

The event yields after selection are estimated as shown in Tables. 6.3. The largest background contribution comes from the associated production of Z boson with heavy flavour jets. For example, in case of $\mu\mu$ 1 b-tag exclusive, the corresponding plots are estimated as shown in Fig. 6.5. In $\mu\mu$ channel, the MC predictions are consistent with data event.

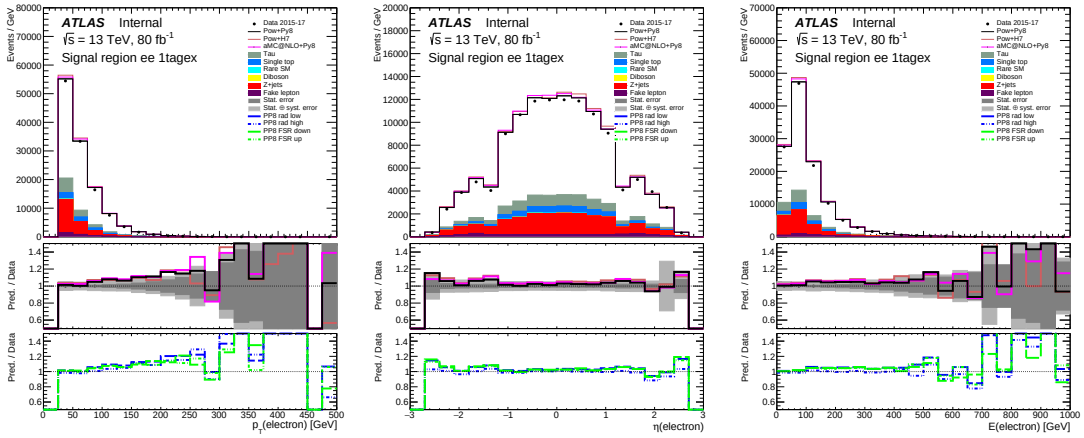

(a) Electron p_{T} (b) Electron η (c) Electron energy

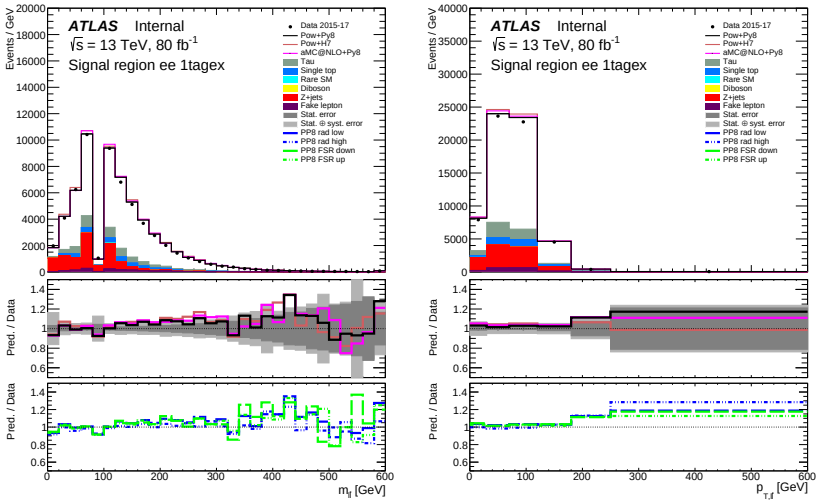

(d) Dilepton invariant mass, $m_{l\bar{l}}$ (e) Dilepton transverse momentum, $p_{T,l\bar{l}}$

Figure 6.4: A comparison of the observed data and prediction for lepton properties in the *ee* 1-*b* excl. channel. The bottom panels show the ratio of data to MC predictions.

Process:	$\mu\mu$ channel	
	1 b excl	2 b incl.
$t\bar{t}$	51617±83	64701±92
$t\bar{t}$ (other final state)	5095±26	6134±28
Single top	3251±25	1443±16
Diboson	254±4	40±2
Z + jets	10202±281	1451±85
Rare SM ($t\bar{t}V$, $t\bar{t}H$, etc)	135±2	200±2
Fakes	76±3	29±2
Total Prediction	70630±295	73998±129
Data (79.7 fb^{-1})	75152	76825

Table 6.3: Event yields in the dilepton topology, $\mu\mu$ channels split by b-tag multiplicity (1 b-excl., 2-b incl.). Presented uncertainty include detector systematics, background normalization and statistical uncertainty. No fake lepton calibration factor is applied here.

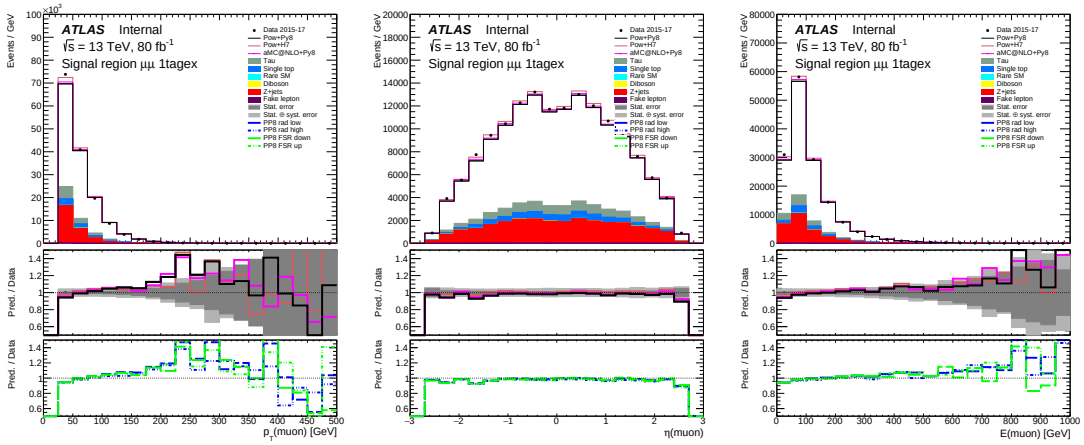

(a) Muon p_{T} (b) Muon η (c) Muon energy

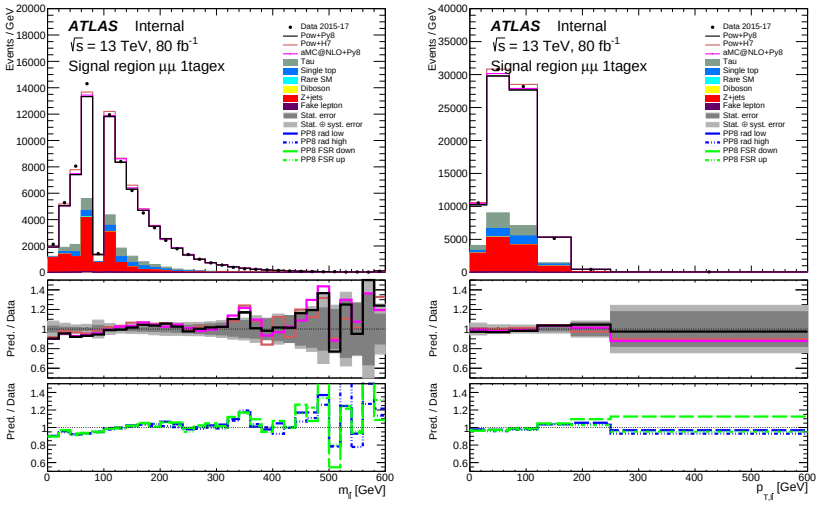

(d) Dilepton invariant mass, $m_{l\bar{l}}$ (e) Dilepton transverse momentum, $p_{T,l\bar{l}}$

Figure 6.5: A comparison of the observed data and prediction for lepton properties in the $\mu\mu$ 1-b excl. channel. The bottom panels show the ratio of data to MC predictions. The error bars on data points are statistical error only.

6.3 Kinematic reconstruction

Kinematic reconstruction of top and anti-top pairs in the dilepton channel is performed due to the presence of two unobserved neutrinos in the final state. In each event, there may be more than two jets and therefore many possible combinations of jets to use in the kinematic reconstruction. In addition, there is an ambiguity in assigning a jet to the t or to the $\bar{t}$ candidate. In events with only one b-tagged jet, the b-tagged jet and the highest-p_{T} non-b-tagged jet are used to reconstruct the t and $\bar{t}$, whereas in events with two or more b-tagged jets, the two b-tagged jets with the highest weight from the b-tagging `MV2c10` algorithm are used. The reconstructed t, $\bar{t}$, and $t\bar{t}$ system are constructed using the neutrino weighting (NW) method [9].

6.3.1 Neutrino Weighting method

Although the individual four-momenta of the two neutrinos in the final state are not directly measured in the detector, the sum of their transverse momenta is measured as $\boldsymbol{p}_{\mathrm{T}}^{\mathrm{miss}}$. The absence of the measured four-momenta of the two neutrinos leads to an under-constrained system that cannot be solved analytically. However, if additional constraints are placed on the mass of the top-quark, the mass of the W boson, and on the pseudorapidities of the two neutrinos, the system can be solved using the following equations:

$$\begin{aligned} (\ell_{1,2} + \nu_{1,2})^2 &= m_W^2 = (80.4 \text{ GeV})^2, \\ (\ell_{1,2} + \nu_{1,2} + b_{1,2})^2 &= m_t^2 = (172.5 \text{ GeV})^2, \\ \eta(\nu_1),\ \eta(\nu_2) &= \eta_1,\ \eta_2, \end{aligned} \tag{6.1}$$

where $\ell_{1,2}$ are the charged leptons, $\nu_{1,2}$ are the neutrinos, and $b_{1,2}$ are the b-jets (or jets), representing four-momentum vectors. Here, η_1, η_2 are the assumed pseudorapidity values of the two neutrinos. The values are scanned between -5 and 5 in steps of 0.2. In total, 2500 combinations are tested for reconstruction of a top-pair in each event.

With the assumptions about m_t, m_W, and values for η_1 and η_2, equation (6.1) can now be solved, leading to two possible solutions of $\boldsymbol{p}_{\mathrm{T}}^{\mathrm{miss}}$ for each assumption of $\eta(\nu_1)$ and $\eta(\nu_2)$. Only real components are considered though solutions are complex numbers in general. A "reconstructed" $\boldsymbol{p}_{\mathrm{T}}^{\mathrm{miss}}$ value resulting from the neutrinos for each solution is compared to the $\boldsymbol{p}_{\mathrm{T}}^{\mathrm{miss}}$ observed in the event. If this reconstructed $\boldsymbol{p}_{\mathrm{T}}^{\mathrm{miss}}$ value matches the observed $\boldsymbol{p}_{\mathrm{T}}^{\mathrm{miss}}$ value in the event, then the solution with those values of η_1 and η_2 is likely to be the correct one. A weight, w, is introduced in order to quantify this agreement:

$$w = \exp\left(\frac{-\Delta {p_x^{\mathrm{miss}}}^2}{2\sigma_x^2}\right) \cdot \exp\left(\frac{-\Delta {p_y^{\mathrm{miss}}}^2}{2\sigma_y^2}\right), \tag{6.2}$$

where $\Delta p_{x,y}^{\mathrm{miss}}$ is the difference between reconstructed and observed values and $\sigma_{x,y}$ is the resolution of the observed $\boldsymbol{p}_{\mathrm{T}}^{\mathrm{miss}}$ in the detector in the x–y plane. The $\boldsymbol{p}_{\mathrm{T}}^{\mathrm{miss}}$ resolution is taken to be 20% for both the x and y directions [57]. The assumption for $\eta(\nu_1)$ and $\eta(\nu_2)$ that gives the highest weight is used to reconstruct the t and $\bar{t}$ for that event. The highest-weight solution remains the same regardless of the choice of $\sigma_{x,y}$.

Equation (6.1) sometimes become unphysical value for a particular assumption of $\eta(\nu_1)$ and $\eta(\nu_2)$. This can be caused by misassignment of the input objects four-momenta and it becomes unphysical value in a real component. To mitigate these effects, the assumed value of m_t is varied between the values of 171 and 174 GeV, in steps of 0.5 GeV, and the p_{T} of the measured jets are smeared using a Gaussian function with a p_{T}-dependent width between 14% and 8% of their measured p_{T}. This allows the NW algorithm to shift the four-momenta (of the electron, muon and the two jets) and m_t assumption to see if a solution can be found. The solution which produces the highest w is taken as the reconstructed system, and the weight is required to be at least 0.0 in order to remove events with poorly reconstructed kinematics. Solutions which provide an invariant mass of the $t\bar{t}$ system below 300 GeV, or which provide t or $\bar{t}$ with negative energies, are automatically rejected.

For a fraction of events, even smearing does not help to find a solution. Such events are not included in the signal selection and are counted as an inefficiency of the reconstruction. For example, in case of $e\mu$ 1 b-tag exclusive, the top-quark and top-pair properties after applying NW are estimated as shown in Fig. 6.6. The total prediction with systematic uncertainties is good in agreement with data event.

Moreover, other different technique used for reconstruction of top and antitop quark momenta was considered: the KLFitter method [58]. Comparison of these techniques is provided in App. C. Based on the study, the NW method was chosen our promary method, and the detail of KLF method is summarized in App. B.

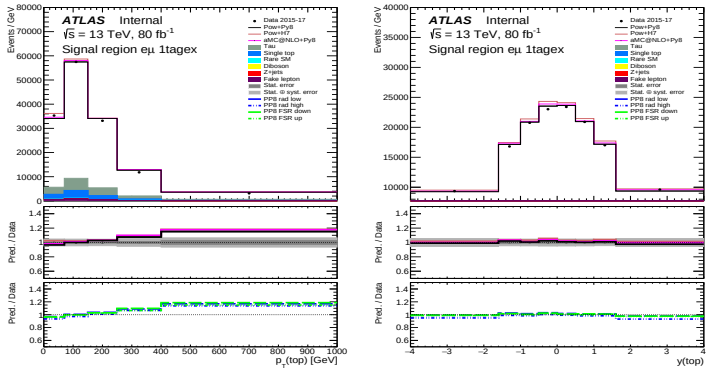

(a) top p_{T} (b) top y

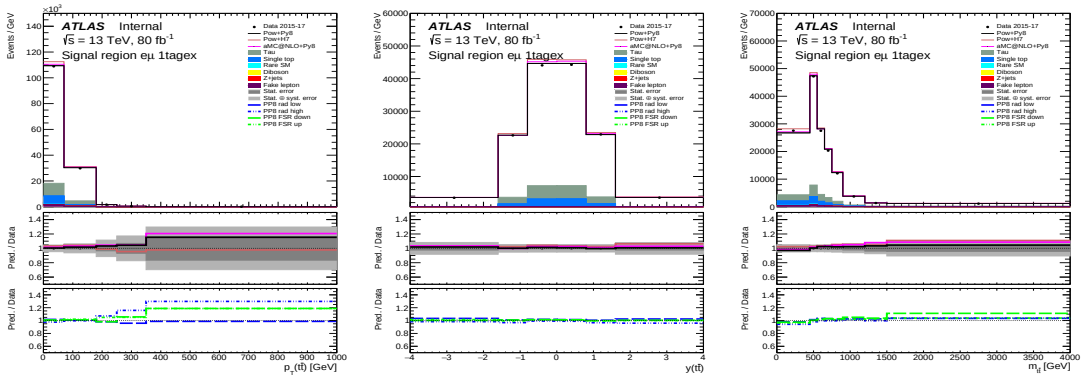

(c) top pair p_{T} (d) top pair y (e) top pair mass

Figure 6.6: A comparison of the observed data and prediction for the top-quark and top-pair properties in the $e\mu$ 1-b excl. channel. The bottom panels show the ratio of data to MC predictions.

Chapter 7

Unfolding

In this chapter, a analysis method as the main point of this thesis is described. The observed $\Delta|y|$ distribution needs to be corrected by "unfolding" because the observed $\Delta|y|$ distribution is distorted due to detector resolution and acceptance effects. In this thesis, the *Fully Bayesian Unfolding* (FBU) [10] is used to estimate the charge asymmetry from the reconstruction level spectra. A method called marginalization is used to surpress the systematic uncertainties.

7.1 Method description

FBU is an application of Bayesian inference to the problem unfolding: Given the data ($\mathrm{D} \in \mathbb{N}^{N_r}$) and the response matrix $\mathcal{M} \in \mathbb{R}^{N_r} \times \mathbb{R}^{N_t}$ (as described in App. D) we want to estimate the actual truth-level spectrum ($\tilde{\mathrm{T}} \in \mathbb{R}^{N_t}$).
Bayesian inference:

$$P(\mathrm{T}|\mathrm{D}, \mathcal{M}) \propto \mathcal{L}(\mathrm{D}|\mathrm{T}, \mathcal{M})\pi(\mathrm{T}), \tag{7.1}$$

where $P(\mathrm{T}|\mathrm{D}, \mathcal{M})$ is the posterior probability of the true spectrum T; $\mathcal{L}(\mathrm{D}|\mathrm{T}\mathcal{M})$ is the likelihood function of D given T and $\mathcal{M}$ and $\pi(\mathrm{T})$ is the prior probability density for the true spectrum T. These are further described in Sec. 7.1.1 and 7.1.2. By sampling the prior probability distribution of the true spectrum and propagating the tallies through the likelihood, it is possible to obtain the posterior distribution of the true spectrum. The sampling is described in more detail in Sec. 7.1.3.

7.1.1 Likelihood

The likelihood term in the Bayes theorem is based upon assumption that the data follows Poisson statistics. The likelihood is defined by comparing the observed spectrum D with the expected one R; assuming Poisson statistics & background prediction $\mathrm{B} \in \mathbb{R}^{N_r}$:

$$\mathcal{L}(\mathrm{D}|\mathrm{T},\mathcal{M},\mathrm{B}) = \prod_{i=1}^{N_r} \frac{(r_i+b_i)^{d_i}}{d_i!} e^{-(r_i+b_i)} \tag{7.2}$$

where r_i and b_i are the expected signal and background yields in ith bin respectively and d_i is the observed data yield in ith bin. The relation between the expected reconstructed signal distribution and the true distribution T can be expressed by response matrix $\mathcal{M}$.

$$r_i(\mathrm{T},\mathcal{M}) = \sum_{j=0}^{N_r} m_{ij} t_j, \tag{7.3}$$

where the response matrix $\mathcal{M}$ is defined by its elements $m_{ij} = \epsilon_{t_j} P(r_i|t_j)$. It contains two pieces of information:

- ϵ_{t_j} - the efficiency for an event from a true bin t_j to be reconstructed in any bin r
- $P(r_i|t_j)$ - probability for an event produced in the true bin t_j to be observed in the reconstructed bin r_i

The ϵ_{t_j} effectively determines the combined detector acceptance, reconstruction efficiency and selection efficiency.The probability $P(r_i|t_j)$ determines the migrations of events that were reconstructed and passed the selection.

7.1.2 Prior

Prior probability density $\pi(\mathrm{T})$ is to be chosen according to what we know about T before the measurement is performed. The simplest possible choice is a flat, so called "uninformative" prior, which is a bounded uniform distribution: Such a choice of prior makes no assumptions about T other than that values outside of a chosen interval are not considered. It is possible to extend this choice of prior with additional information, effectively introducing regularization function, defined by $S(\mathrm{T})$:

$$\pi(\mathrm{T}) \propto \begin{cases} e^{\alpha S(\mathrm{T})} & \text{if } \mathrm{T}_t \in [\mathrm{T}_t^{\lceil}, \mathrm{T}_t^{\rceil}], \forall t \in [1, N_t] \\ 0 & \text{otherwise} \end{cases} \tag{7.4}$$

where α is an arbitrary parameter. This enables to use additional information to constrain the parameter space and reduce variance at a cost of introducing a small bias. In this analysis, an uninformative prior is used with bounds given by MC-based prediction $\tilde{\mathrm{T}}$: $[0, 2\tilde{\mathrm{T}}]$.

7.1.3 Sampling

The posterior probability distribution $P(\mathrm{T}, \mathrm{D})$ is determined by sampling the N_t-dimensional parameter space and evaluating for each point the product of $\mathcal{L}(\mathrm{D}|\mathrm{T},\mathcal{M})$ and $\pi(\mathrm{T})$, thus performing a numerical integration. The sampling is performed using Markov Chain Monte Carlo-based methods [59]. Two sampling algorithms are employed simultaneously within FBU to sample the parameter space:

- *Metropolis-Hastings* algorithm [60] used to sample discrete distriutions, such as the Poissonian-distributed unfolded truth bins.
- *No-U-turn sampler* algorithm [61] used to sample continuously-distributed parameters, such as nuisance parameters.

Within FBU, the technical implementation of the sampling is done using the *PyMC3* package [62]. The unfolded $t\bar{t}$ charge asymmetry are estimated using *No-U-turn sampler*(NUT) algorithm. The result of the sampling is the posterior probability distribution for each bin of the spectrum, in contrast to other unfolding methods where the result is an estimate with its variance for each bin of the unfolded spectrum. Subsequently, posterior probability density distribution can be obtained for any quantity that is computed from the spectrum, such as A_C:

$$p(A_C|\mathrm{D}) = \int \delta(A_C - A_C(\mathrm{T}))P(\mathrm{T}|\mathrm{D})d\mathrm{T} \tag{7.5}$$

The mean and width of the posterior distribution represent the estimate and its variance.

7.2 Marginalization

Treatment of systematic uncertainties is naturally included by extending $\mathcal{L}(\mathrm{D}|\mathrm{T})$ with nuisance parameter terms. Marginal likelihood is defined as

$$\mathcal{L}(\mathrm{D}|\mathrm{T}) = \int \mathcal{L}(\mathrm{D}|\mathrm{T},\theta)\pi(\theta)\mathrm{d}\theta \tag{7.6}$$

where θ are the nuisance parameters and $\pi(\theta)$ their priors - Gaussian distributions G with $\mu = 0$ and $\sigma = 1$. Two categories are considered:

- Background normalizations θ_b - affect only the background predictions
- Uncertainties related to object identification, reconstruction & calibration θ_s - affect both the signal and background prediction; $\mathrm{R}(\mathrm{T};\theta_s)$ and $\mathrm{B}(\theta_s,\theta_b)$

After including the nuisance parameters, The signal reconstructed-level prediction is then:

$$r_i(\mathrm{T}, \mathcal{M}; \theta_s) = r_i(\mathrm{T}, \mathcal{M}; 0) \left(1 + \sum_k \theta_s^k \Delta r_i^k\right) \tag{7.7}$$

where $r_i(\mathrm{T}, \mathcal{M}; 0)$ is defined as above equation and Δr_i^k is the relative systematic uncertainty variation on signal yield in ith bin corresponding to the kth nuisance parameter θ_s^k.
Similarly the prediction for each background process:

$$b_i(\theta_s, \theta_b) = b_i(0)(1 + \theta_b \Delta b) \left(1 + \sum_k \theta_s^k \Delta b_i^k\right) \tag{7.8}$$

where $b_i(0)$ is the predicted yield of background in ith bin, Δb is the relative uncertainty on the background normalization and Δr_i^k is the relative systematic uncertainty variation on signal yield in ith bin of background corresponding to kth nuisance parameter θ_s^k.
The marginal likelihood becomes then:

$$\mathcal{L}(\mathrm{D}|\mathrm{T}) = \int \mathcal{L}(\mathrm{D}|\mathrm{R}(\mathrm{T}; \theta_s), \mathrm{B}(\theta_s, \theta_b)) G(\theta_s) G(\theta_b) \mathrm{d}\theta_s \mathrm{d}\theta_b \tag{7.9}$$

The marginal posterior probability density for T is computed by sampling the N_t and N_{np} parameter space, where N_{np} is the total number of nuisance parameters, and projecting the sample over the T parameter space. The projections over each nuisance parameter give the corresponding marginalized posterior probability density. Typically, this posterior probability density is a Gaussian. The mean and variance of the marginalized posterior distribution correspond to the marginalized nuisance parameter pull and constraint. For nuisance parameters which can be further constrained from the data, this posterior distribution function will be narrower than the prior distribution. Examples of the prior and posterior probability densities for two nuisance parameters are shown in Fig. 7.1. The posterior probability density for $A_{\mathrm{C}}^{t\bar{t}}$ is computed as described in Sec. 7.1.3 with the difference that the RMS of the marginal posterior represents the total uncertainty. Similarly, each nuisance parameter is estimated by the mean value and RMS of the corresponding projection of the posterior probability density.

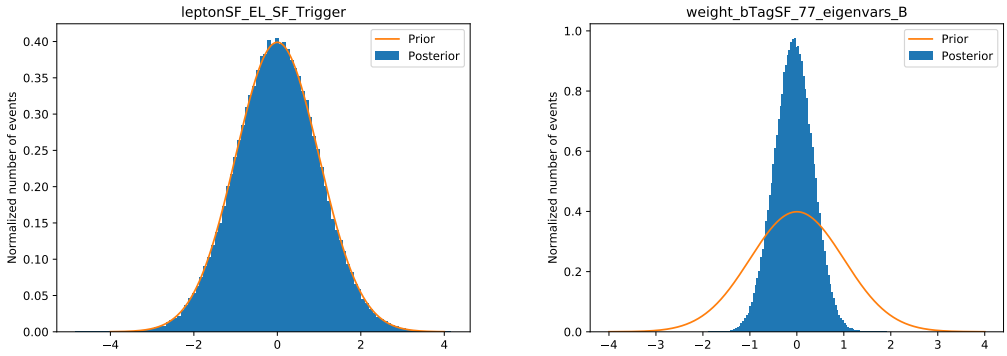

(a) leptonSF_EL_SF_Trigger (b) weight_bTagSF_77_eigenvars_B_0

Figure 7.1: The prior and posterior probability density for nuisance parameters corresponding to electron trigger scale factor (a) and a component of b-tagging effciency calibration (b). No constraint is observed for the electron trigger scale factor, while the b-tagging effciency calibration is constrained and pulled because the sample is divided in b-jet multiplicity bins.(see Sec. 7.3)

7.3 Channel combination

Using orthogonal channels with different background contamination enables to constrain the individual systematic uncertainties and to reduce the total uncertainty by exploiting additional information in the individual regions. Having the nuisance parameters common to all channels, the likelihood is:

$$\mathcal{L}(\{\mathrm{D}_1 \cdots \mathrm{D}_{N_{ch}}\}|\mathrm{T}) = \int \prod_{i=1}^{N_{ch}} \mathcal{L}(\mathrm{D}_i|\mathrm{T};\theta) G(\theta) \mathrm{d}\theta \tag{7.10}$$

The final posterior probability density:

$$P(\mathrm{T}|\{\mathrm{D}_1 \cdots \mathrm{D}_{N_{ch}}\}) = \int \prod_{i=1}^{N_{ch}} \mathcal{L}\left(\mathrm{D}_i|\mathrm{R}_i(\mathrm{T};\theta_s), \mathrm{B}_i(\theta_s,\theta_b)\right) G(\theta_s) G(\theta_b) \pi(\mathrm{T}) \mathrm{d}\theta_s \mathrm{d}\theta_b \tag{7.11}$$

Here, the probability density is applied to fit using Asimov data set, which provides a simple method to obtain the median experimental sensitivity of a search or measurement as well as fluctuations about the expectation. The nuisance parameters obtained from Asimov fit are shown in Fig. 7.2 for inclusive $t\bar{t}$ asymmetry. The estimations of nuisance parameters are using PyMC3.

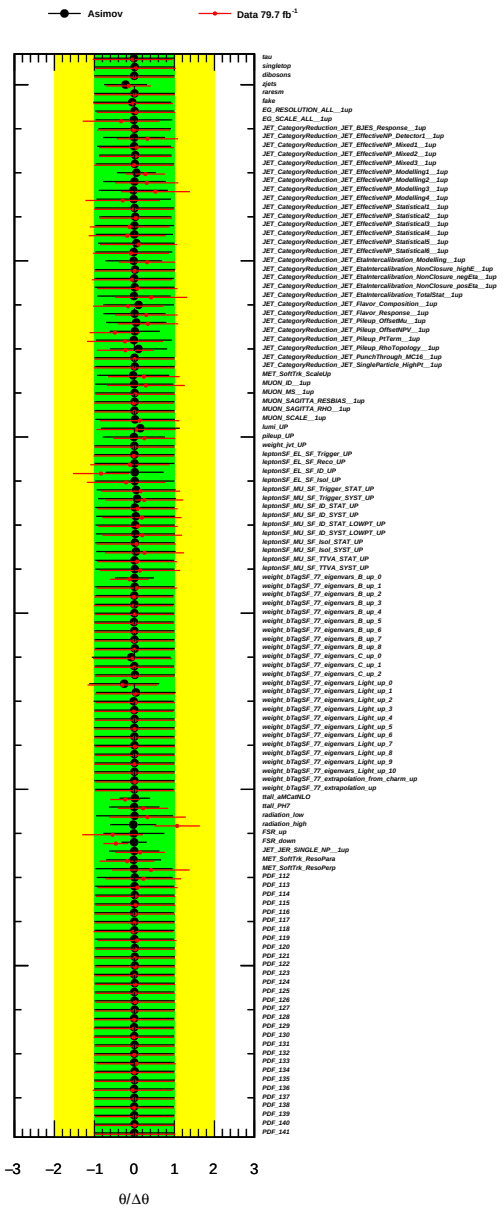

Figure 7.2: Nuisance parameters for the inclusive $A_{\mathrm{C}}^{t\bar{t}}$ measurement obtained from Asimov (black) and Data (red) marginalization in combined all dilepton channels. The color regions highlight the 1σ (green) and 2σ (yellow) intervals of the prior probability density. The estimations of nuisance parameters are using PyMC3. The boostrapping is applied, for the sampling, a tuning of the sampling parameters is performed using 4×2500 steps. To tally the posterior distributions, 4×10000 sampled steps are used.

The nuisance parameters for the inclusive and differential measurements are shown in App. G.

7.4 Binning choice and bias

For the unfolding, an appropriate binning of reconstructed $\Delta|y|$ distributions as well as true $\Delta|y|$ distribution must be chosen. Two competing factors determine the choice of binning in the $\Delta|y|$ distribution:

- Smaller number of bins implies smaller relative statistical uncertainties and vice-versa. At least two bins are necessary to compute $A_C^{t\bar{t}}$ (positive and negative side of the $\Delta|y|$ distribution).
- Larger number of bins allows to track the migrations more accurately and thus allow to obtain unbiased estimates for each bin content. However, only migrations that change the $\Delta|y|$ sign affect the computation of A_C and these are more likely for small $\Delta|y|$ values. Therefore a fine binning is required in the central $\Delta|y|$ region.

As was shown previously [63], four bins in $\Delta|y_{t\bar{t}}|$ is the minimum required for an unbiased response. Using more than 4 bins increases the complexity of the unfolding, therefore we use exactly 4 bins for $\Delta|y_{t\bar{t}}|$ distribution. The bias in the unfolding response is measured by studying the unfolded asymmetry in pseudo-data samples with known true asymmetry. These samples are obtained by reweighting the baseline signal sample to a different charge asymmetry prediction event-by-event based on the value of true $\Delta|y_{t\bar{t}}|$. Two independent reweightings can be considered:

- **Protos reweighting:** Based on BSM axigluon models in which the asymmetry value is predicted to be significantly different from the standard model one. It is defined as a ratio of simulated heavy axigluon sample generated using the PROTOS generator [64] over the nominal signal sample. Asymmetries of $\sim \pm 1\%$, $\pm 2\%$, $\pm 3\%$, and $\pm 4\%$ are considered.
- **Linear reweighting:** The $\Delta|y_{t\bar{t}}|$ distribution is reweighted per-event by $w = 1 + k \times \text{true } \Delta|y_{t\bar{t}}|$.

In order to achieve an unbiased unfolded asymmetry, the $\Delta|y_{t\bar{t}}|$ bin edges $\boldsymbol{x}$ in binning of $[-5.0, -\boldsymbol{x}, 0, \boldsymbol{x}, 5.0]$ need to be optimized. The PROTOS reweighted sample is used for this study (more details in App. F). The linear reweighted sample is used as a cross-check.
The criterion to select the best binning is based on the expected statistical sensitivity and the linearity test of the $\Delta|y_{t\bar{t}}|$ binning, in order to have an unbiased estimate when looking at the calibration curves. Ideal linearity is achieved when the slope of the calibration curves is 1 and the offset is 0. If the agreement between unfolded and truth $A_C^{t\bar{t}}$ for the best binning configuration is not perfect, it is necessary to account for this bias in the overall uncertainty of the $A_C^{t\bar{t}}$ values. From

the linearity lines, with unfolded $A_C^{t\bar{t}}$ = slope × truth $A_C^{t\bar{t}}$ + offset, inverting this equation gives truth $A_C^{t\bar{t}}$ = (unfolded $A_C^{t\bar{t}}$- offset)/slope. An uncertainty on the unfolding is then given by:

$$\text{bias} = \text{unfolded } A_C^{t\bar{t}}\text{- true } A_C^{t\bar{t}} = \text{unfolded } A_C^{t\bar{t}}\text{- (unfolded } A_C^{t\bar{t}}\text{- offset)/slope .}$$

The optimal $\Delta|y|$ binning is obtained by running FBU with statistical uncertainties only. To validate that linear response is kept when systematic uncertainties are included in the FBU, the linearity tests are repeated with systematics included using the optimal binning.
In the case of differential measurements, the choice of differential bin edges of variable of interest ($m_{t\bar{t}}$, $p_{T,t\bar{t}}$, $\beta_{z,t\bar{t}}$) is motivated by physics considerations as mentioned in Chapter 1. Taking into account the statistical limitations, the following binning is used:

- $m_{t\bar{t}}$- 5 bins: $[0, 500, 750, 1000, 1500, \infty]$
- $\beta_{z,t\bar{t}}$- 4 bins: $[0, 0.3, 0.6, 0.8, 1]$
- $p_{T,t\bar{t}}$- 3 bins: $[0, 30, 120, \infty]$

Additionally for each bin of variable of interest ($m_{t\bar{t}}$, $p_{T,t\bar{t}}$, $\beta_{z,t\bar{t}}$), we optimize bin edges x in $\Delta|y_{t\bar{t}}|$ binning of [-5;$-x$; 0; x; 5]. The slope, offset, and bias obtained from the PROTOS reweighting functions are shown in Tables 7.1.

	$\Delta\|y_{t\bar{t}}\|$ binning	Protos reweighting		$\frac{\text{bias}}{A_C^{t\bar{t}}\text{uncer.}}$ [%]
		slope	offset	
inclusive	[-5;**-0.5**; 0; **0.5**; 5]	0.9957±0.0039	-0.0002±0.0001	3.30
$m_{t\bar{t}} \in$ [0, 500]	[-5;**-0.4**; 0; **0.4**; 5]	0.9752±0.0139	0.0003±0.0003	1.15
$m_{t\bar{t}} \in$ [500, 750]	[-5;**-0.5**; 0; **0.5**; 5]	0.9716±0.0058	-0.0004±0.0002	5.26
$m_{t\bar{t}} \in$ [750, 1000]	[-5;**-0.8**; 0; **0.8**; 5]	0.9764±0.0151	0.0021±0.0005	7.05
$m_{t\bar{t}} \in$ [1000, 1500]	[-5;**-0.8**; 0; **0.8**; 5]	1.0209±0.0294	-0.0054±0.0010	9.91
$m_{t\bar{t}} \in$ [1500, ∞]	[-5;**-1.0**; 0; **1.0**; 5]	0.7393±0.1003	0.0062±0.0034	1.95
$p_{T,t\bar{t}} \in$ [0, 30]	[-5;**-0.5**; 0; **0.5**; 5]	0.9901±0.0128	0.0004±0.0004	1.69
$p_{T,t\bar{t}} \in$ [30, 120]	[-5;**-0.6**; 0; **0.6**; 5]	1.0263±0.0103	-0.0002±0.0003	1.38
$p_{T,t\bar{t}} \in$ [120, ∞]	[-5;**-0.6**; 0; **0.6**; 5]	1.0236±0.0117	0.0000±0.0003	0.17
$\beta_{z,t\bar{t}} \in$ [0.0, 0.3]	[-5;**-0.4**; 0; **0.4**; 5]	1.0590±0.0303	-0.0014±0.0004	6.65
$\beta_{z,t\bar{t}} \in$ [0.3, 0.6]	[-5;**-0.4**; 0; **0.4**; 5]	0.9946±0.0101	0.0007±0.0003	4.46
$\beta_{z,t\bar{t}} \in$ [0.6, 0.8]	[-5;**-0.7**; 0; **0.7**; 5]	1.0460±0.0077	-0.0011±0.0003	7.26
$\beta_{z,t\bar{t}} \in$ [0.8, 1.0]	[-5;**-0.5**; 0; **0.5**; 5]	0.9584±0.0068	0.0021±0.0002	13.5

Table 7.1: Linearity test - the slope, offset and bias for inclusive and differential $A_C^{t\bar{t}}$. The statistical uncertainties are included in the linearity test.

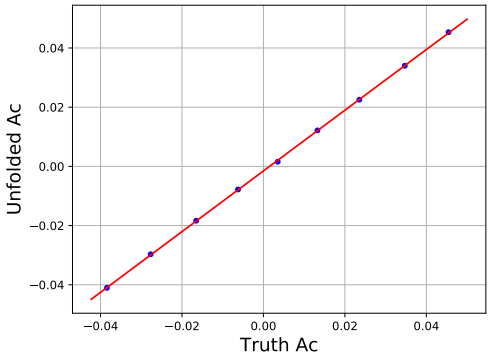

Figure 7.3: Linearity test results for the inclusive $A_{\mathrm{C}}^{t\bar{t}}$ using PROTOS reweighting function when the binning edge $x = 0.5$. It is included systematic uncertainties in the tests.

In the case of inclusive measurement best results are gained with a $\Delta|y_{t\bar{t}}|$ binning of **[-5;-0.5; 0; 0.5; 5]**. The optimal calibration lines with different injected asymmetries at $x = 0.5$ are shown at Fig. 7.3. Futhermore, Iterative Bayesian unfolding was also studied as described in App. E.

Chapter 8

Systematic uncertainties

In this chapter, various systematic uncertainties affecting the signal and background prediction are considered. Individual sources of systematic uncertainties are considered to be uncorrelated. In order to mitigate the effect of limited MC statistics on systematic uncertainties, the bootstrapping method is used to smooth systematic uncertainties that suffer from large statistical fluctuations. The treatment of two-sided and one-sided systematic uncertainties is as follows, unless explicitly stated otherwise. For two-sided uncertainties, the average of up and down variations (each with respect to nominal) is taken as a symmetric systematic two-sided variation. For one-sided systematic uncertainties, the difference between the shifted variation and nominal is taken as the uncertainty and symmetrized. A nuisance parameter with gaussian prior is assigned to each systematic uncertainty, unless otherwise specified, and their effect on the measurement is directly embedded in the unfolding procedure.

8.1 Experimental uncertainties

8.1.1 Luminosity

The uncertainty on the combined 2015-2017 integrated luminosity is 2.0%. It is derived, following a methodology similar to that detailed in [39], from calibrations of the luminosity scale using x-y beam-separation scans performed in August 2015, May 2016 and July 2017.

8.1.2 Pile-up

Scale factors are applied to reweigh simulated events in order to obtain the pile-up distribution corresponding to data. An uncertainty on these reweighting scale factors is considered, based on the disagreement between the instantaneous luminosity in data [39] and in simulation. Both the nominal and systematically-shifted

pileup-reweighting weights are obtained using the standard `PileuReweighting` tool [65].

8.1.3 Lepton identification, reconstruction, isolation and trigger

Lepton (e, μ) identification, reconstruction, isolation and trigger performance differ between data and simulation and scale factors are applied to correct these differences. These are obtained by a tag-and-probe method using Z boson, W boson and J/ψ decays [66, 67]. Uncertainties on the scale factors are considered.

8.1.4 Lepton momentum scale and resolution

Lepton momentum scale and resolution might be different between the simulation and data. This is studied with reconstructed distributions of $Z \to \ell^+\ell^-$, $J/\psi \to \ell\ell$ and $W \to e\nu$ using methods similar to [67, 68]. Observed discrepancies are corrected and uncertainties on these corrections are considered.

8.1.5 Jet vertex tagger efficiency

The uncertainty related to the JVT scaling factors applied to the MC simulation includes the statistical uncertainty, 20% uncertainty on the estimation of the residual contamination from pile-up jets after pile-up suppression and a systematic uncertainty assessed by using different generators for the MC simulation of the $Z \to \mu\mu$ and $t\bar{t}$ events [54].

8.1.6 Jet energy scale

The jet energy scale (JES) and its uncertainty is estimated from the test-beam data, collision data and simulation using techniques described in [69]. Data taken during the $\sqrt{s} = 13$ TeV data taking is used to calibrate the residual uncertainty on the JES. Events with a vector boson and additional jets are used to calibrate jets in the central region. Dijet events are used to calibrate forward jets against the jets in the central region of the detector. Multijet events are used to calibrate high p_{T} jets. The measurements are combined and decorrelated into a set of 29 nuisance parameters which can have different jet p_{T} and η dependencies [70].

8.1.7 Jet energy resolution

Jet energy resolution (JER) has been measured separately for data and simulation using two in-situ techniques [69, 71]. The results of the measurement have been further improved by an additional in-situ measurement using di-jet events and

events with $\gamma+$jet or $Z+$jets. New methods using 2012 data [72] have been used to measure the contribution originating from pile-up activity which contributes significantly to the JER for low-p_{T} jets. The corresponding systematic uncertainty is defined as a quadratic difference between the jet energy resolutions for data and simulation. To estimate the effect on the measurement the energy of jets is smeared by this residual difference and the distributions are compared to the nominal ones.

8.1.8 Large jet moment scale and resolution

The scale of the detector response for all jet moments (p_{T}, mass, τ_{32}) is derived by comparing the calorimeter quantity to a reference track jet [73]. The resolution of the detector response is conservatively estimated as a 2% absolute uncertainty on p_{T} and 20% relative uncertainty on jet mass (parametrized in jet p_{T} and m/p_{T}) [74]. Set of 14 nuisance parameters is used to estimate uncertainties due to these effects.

8.1.9 Flavour tagging

The effects of uncertainties in efficiencies for the heavy flavour identification of jets by the b-tagging algorithm have been evaluated and measured from data. Scale factors with their ucertainties are applied to each jet in the simulation depending on its flavour and p_{T} [52]. Together 9 scale-factor components are used to calibrate b-jets, 3 for c-jets and 11 for light jets.

8.1.10 Missing transverse energy scale and resolution

The $E_{\mathrm{T}}^{\mathrm{miss}}$ is calculated from several terms corresponding to different types of reconstructed objects. Uncertainty on each object is evaluated and then propagated to the uncertainty on $E_{\mathrm{T}}^{\mathrm{miss}}$. Two methods are used to estimate the uncertainty on the soft term that enters the $E_{\mathrm{T}}^{\mathrm{miss}}$ calculation [75]. Different uncertainty sources are combined into a total uncertainty on scale and resolution of $E_{\mathrm{T}}^{\mathrm{miss}}$ respectively.

8.2 Theory uncertainties

8.2.1 Cross-section and normalization

For all of the processes considered in the measurement, normalization uncertainties are considered. The only exception is the signal normalization – the signal contribution in the reconstructed $\Delta|y|$ distribution is given by the folded true $\Delta|y|$ distribution as shown in Equation (7.3). Given that the bins of true $\Delta|y|$ distribution are free parameters to be determined in the unfolding, the signal normalization is effectively a free parameter (however not an explicit single parameter in the likelihood). The background normalization uncertainties are assumed to have

truncated Gaussian priors. A lower-bound truncation is imposed to avoid negative background yield. The relative prior uncertainties are 0.05 ($t\bar{t}$ events with τ leptons, dibosons), 0.053 (single top), 0.15 (Z + jets), 0.13 (rare SM processes), and 0.2 (fakes).

8.2.2 $t\bar{t}$ Matrix element modelling

The matrix element (ME) modelling uncertainty is estimated in two different approach, out of which only one will be used for the final result. In the first approach, the ME uncertainty is included in the nuisance parameter marginalization. The systematic shift corresponding to this nuisance parameter is calculated as the difference between aMC@NLO+Pythia8 and Powheg+Pythia8, both simulated using ATLFASTII simulation.
In the second approach, similarly to ME uncertainty, the uncertainty is estimated from the difference of unfolded asymmetry of pseudodata obtained from the alternative sample and the true asymmetry of the alternative sample. The migration matrix is extracted from the Powheg+Pythia8 nominal sample simulated by ATLFASTII simulation. In this thesis, the choice of the final approach is first one.

8.2.3 $t\bar{t}$ Parton shower and hadronisation modelling

The parton shower and hadronisation (PS) modelling uncertainty is estimated using the same two approaches as the ME uncertainty above. The choice of the final approach is the same approach (marginalization approach) as ME. For the marginalization approach, the systematic shift is calculated from the difference of Powheg+Pythia8 and Powheg+Herwig7 prediction.
In the second approach, similarly to ME uncertainty, the uncertainty is estimated from the difference of unfolded asymmetry of pseudodata obtained from the alternative sample and the true asymmetry of the alternative sample. The migration matrix is extracted from the Powheg+Pythia8 nominal sample simulated by ATLFASTII simulation.

8.2.4 $t\bar{t}$ Radiation modelling

Two sources of uncertainty on radiation modelling are considered; the initial state (ISR) and final state (FSR) radiation.
For the ISR uncertainty, two different Powheg+Pythia8 samples with different choices of factorization (μ_f) and renormalisation (μ_r) scales, different h_{damp} and different shower tune variations are compared. Both samples are simulated using ATLFASTII simulation. The `RadHi` variation (radiation up) is estimated using a dedicated MC sample with $h_{\text{damp}} = 517.5$ GeV with scales $\mu_f = \mu_r = 0.5$ of

the nominal scales and with the shower tune variation `Var3cUp`. The `RadLo` variation (radiation down) uses the nominal signal sample with $h_{\text{damp}} = 258.75$ GeV, varying the $\mu_f = \mu_r = 2.0$ of nominal and shower variation `Var3cDown` via weights variations. For each of these variations, the systematic shift is calculated as the difference with respect to nominal POWHEG+PYTHIA8 simulated with ATLFASTII simulation. Only the more conservative variation is taken, which is then symmetrized and included as a nuisance parameter in the marginalization. To decide which of the two variations is more conservative, both variations are tested by including them separately in FBU marginalization and the variation that yields larger unfolded A_{C} uncertainty is considered for final unfolding.
The FSR uncertainty is estimated using variation of $\alpha_{\text{S}}^{\text{FSR}}$ in parton showering by applying weights on the nominal signal sample. The uncertainty is propagated in the same method as the ISR uncertainty, taking the variation resulting in larger total uncertainty on unfolded A_C.

8.2.5 $t\bar{t}$ Parton distribution functions

The uncertainty on parton distribution functions (PDF) is propagated using the PDF4LHC15 prescription [76], using a set of 30 nuisance parameters. The PDF variations are propagated by using alternative MC generator weighs corresponding to the PDF4LHC15 variations, stored within the nomial POWHEG+PYTHIA8 $t\bar{t}$ sample. The systematic uncertainty is obtained by comparing PDF variation to PDF4LHC15 baseline prediction and symmetrized. Each of the 30 PDF variations is considered as a separate nuisance parameter. For example, the summary of configuration of the leading three PDF nuisance parameters is shown in Table. 8.1.

PDF4LHC15 Errorsets	$\delta\alpha_s(M_b)$ [%]	$\delta\alpha_c(M_c)$ [%]	$\delta\alpha_s(M_{\bar{s}}, M_s)$ [%]	$\delta\alpha_s(M_{\bar{u}}, M_u)$ [%]	$\delta\alpha_s(M_{\bar{d}}, M_d)$ [%]	$\delta\alpha_s(M_g)$ [%]
PDF4LHC15 Error 1	21.48	2.773	(-7.373, -2.763)	(-1.558, -0.122)	(-1.231, 3.530)	4.311
PDF4LHC15 Error 2	-89.46	-4.415	(8.446, -2.573)	(-1.720, 0.027)	(-0.355, 0.115)	-1.851
PDF4LHC15 Error 3	17.00	3.169	(-0.907, -2.438)	(4.289, -0.134)	(9.561, -3.947)	4.588

Table 8.1: Setting of the PDF4LHC15 several nuisance parameter sets for main contribution. A baseline value of the strong coupling $\alpha_s(M_Z) = 0.118$ is used for each of these sets, at both NLO and NNLO, with an uncertainty of $\delta\alpha_s(M_Z) = 0.0015$. The difference weights form baseline are shown in each flavour. The same weights set in $\bar{b} = b$ and $\bar{c} = c$.

8.3 Tables with systematic uncertainties

Two approach for the total uncertainty are considered with and without marginalization of the ME and PS signal modelling systematic uncertainties. These samples (ME, PS) are unfolded with keeping the response matrix using the nominal POWHEG+PYTHIA8 sample fixed. The systematic uncertainties due to the signal modeling is estimated by changing the Asimov dataset of these alternative samples as follows.

$$\text{Signal modeling unc. (PS,ME)} = |A_C^{\text{unfold,alt}} - A_C^{\text{true,alt}}| \tag{8.1}$$

Total uncertainties without marginalization of the PS and ME uncertainties are calculated in quadrature as below:

$$\text{Total unc. w/o marg. of PS and ME} = \sqrt{PS^2 + ME^2 + (excl.PS + ME)^2} \tag{8.2}$$

where PS and ME are calculated by above equation, $excl.PS+ME$ is the systematic uncertainties of marginalization excluding PS and ME. In detail, the comparison with and without marginalization of these signal modelling uncertainties for the inclusive and differential measurements are shown in App. H. A summary of all different uncertainties affecting the measurements are shown in Table 8.2 using MC samples. The main contributions are coming form statistical uncertainty in dilepton channels.

8.4 Bootstrap generator method

The Bootstrap Generator [77] method is applied on each systematic uncertainty in order to remove unphysical fluctuations due to limited Monte Carlo sample size. In general it is not easy to estimate statistical uncertainties of the systematic effect, since both the nominal and shifted distribution are typically largely correlated. The Bootstrap method generates for each event n random weights from a Poisson distribution $P(\lambda = 1)$ and subsequently creates n replicas of the nominal and shifted distributions by filling them event by event with the corresponding Poisson weights. Run number and event number are used as a seed for generating the Poisson weights, this ensures that the events which are the same in both the nominal and shifted distributions will behave in a correlated way. The relative difference between the nominal and shifted distributions is then calculated in each bin for all n replicas. The mean relative difference is taken as the systematic uncertainty and the RMS as its statistical component.
Having the correctly estimated statistical uncertainties of the systematic uncertainty it is possible to smooth the distribution in order to remove statistically insignificant effects. The $\Delta|y|$ distribution contains only 4 bins in one channel,

		Stat.	Total	No marg. ME/PS.
inclusive		0.005	0.007	0.007
$m_{t\bar{t}}$	< 500 GeV	0.015	0.018	0.018
	500-750 GeV	0.008	0.010	0.010
	750-1000 GeV	0.025	0.028	0.029
	1000-1500 GeV	0.049	0.054	0.055
	> 1500 GeV	0.189	0.201	0.202
$p_{T,t\bar{t}}$	< 30 GeV	0.016	0.019	0.019
	30-120 GeV	0.012	0.014	0.014
	> 120 GeV	0.013	0.019	0.017
$\beta_{z,t\bar{t}}$	0-0.3	0.019	0.021	0.022
	0.3-0.6	0.014	0.016	0.017
	0.6-0.8	0.012	0.013	0.014
	0.8-1.0	0.011	0.013	0.013

Table 8.2: Summary of the uncertainties affecting the inclusive and differential $A_C^{t\bar{t}}$ measurements in the dilepton channels. Two scenarios for the total uncertainty are considered - with and without marginalization of the ME and PS signal modelling systematic uncertainties, labeled as Total and No marg. ME/PS, respectively.

therefore the smoothing procedure differs from the one described in [77] and [78]. Bootstrapping is applied on $\Delta|y|$ distributions (used for unfolding and the measurement itself) only, not in the control distributions for other variables. All systematic uncertainties are bootstrapped, except those, which are 100% correlated and therefore always statistically significant, such as various scale-factor systematic uncertainties.

8.5 Effect of marginalization on data/MC agreement

The FBU procedure is used to constrain the effect of the individual systematic uncertainties. This reduces the total uncertainty significantly and improves the agreement between data and prediction by pulling some of the uncertainties. This is demonstrated in Fig. 8.1 - 8.4. By definition, there should be a perfect agreement after the marginalization. For these variables, it doesn't expect perfect agreement between data and prediction, but if the pulls and constrains obtained from FBU are physical, the agreement should be better after the marginalization procedure.

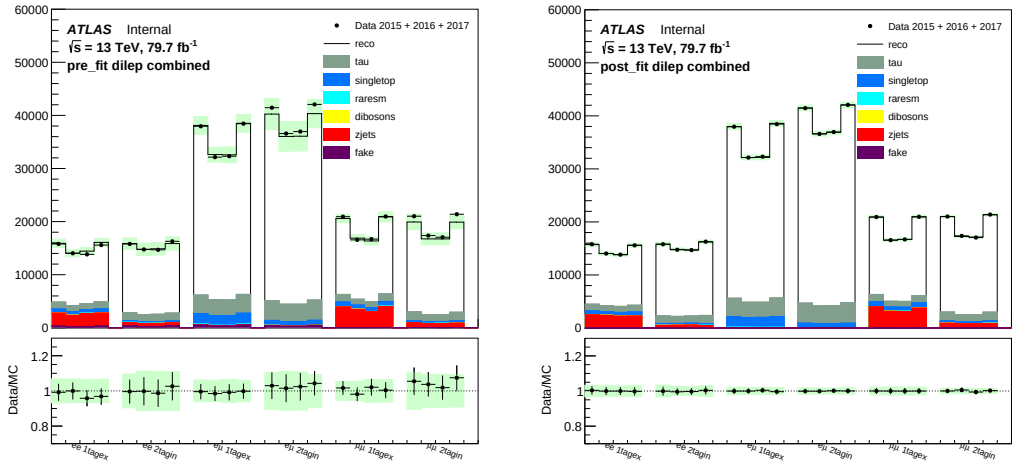

(a) Inclusive pre-fit

(b) Inclusive post-fit

Figure 8.1: Comparison between data and prediction for bins used in the inclusive A_C measurements. This comparison is shown before (left, labeled as pre-fit) and after (right, labeled as post-fit) marginalization within FBU.

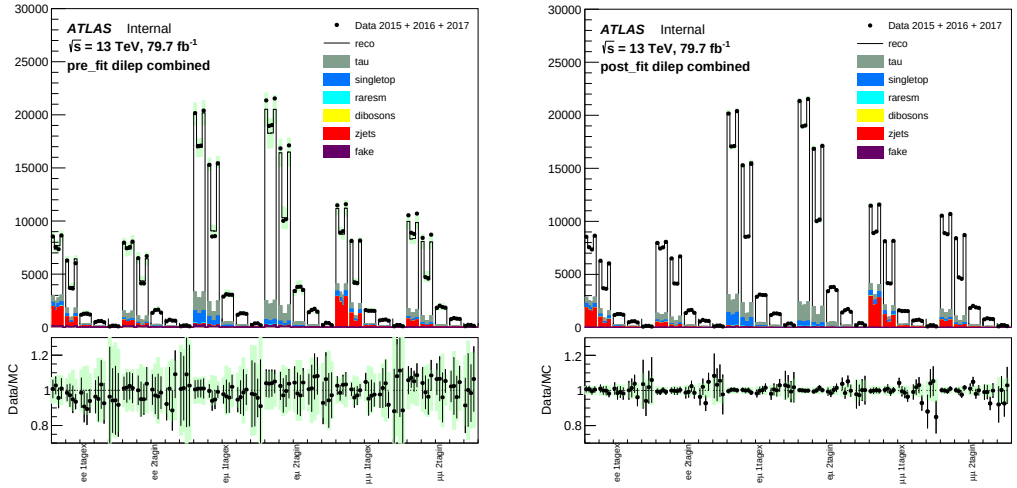

(a) Differential $m_{t\bar{t}}$ pre-fit

(b) Differential $m_{t\bar{t}}$ post-fit

Figure 8.2: Comparison between data and prediction for bins used in the differential as function of $m_{t\bar{t}}$ (bottom) A_C measurements. This comparison is shown before (left, labeled as pre-fit) and after (right, labeled as post-fit) marginalization within FBU.

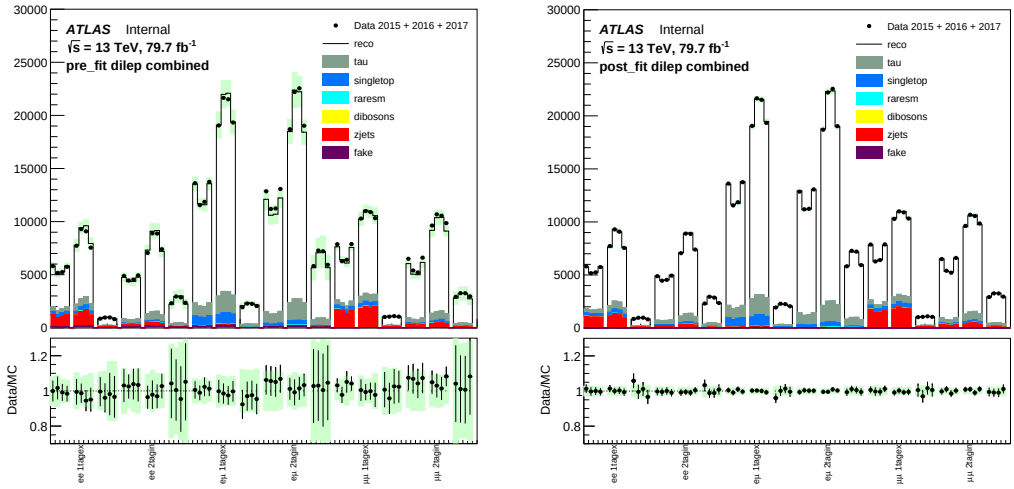

(a) Differential $p_{T,t\bar{t}}$ pre-fit (b) Differential $p_{T,t\bar{t}}$ post-fit

Figure 8.3: Comparison between data and prediction for bins used in the differential as function of $p_{T,t\bar{t}}$ (bottom) A_{C} measurements. This comparison is shown before (left, labeled as pre-fit) and after (right, labeled as post-fit) marginalization within FBU.

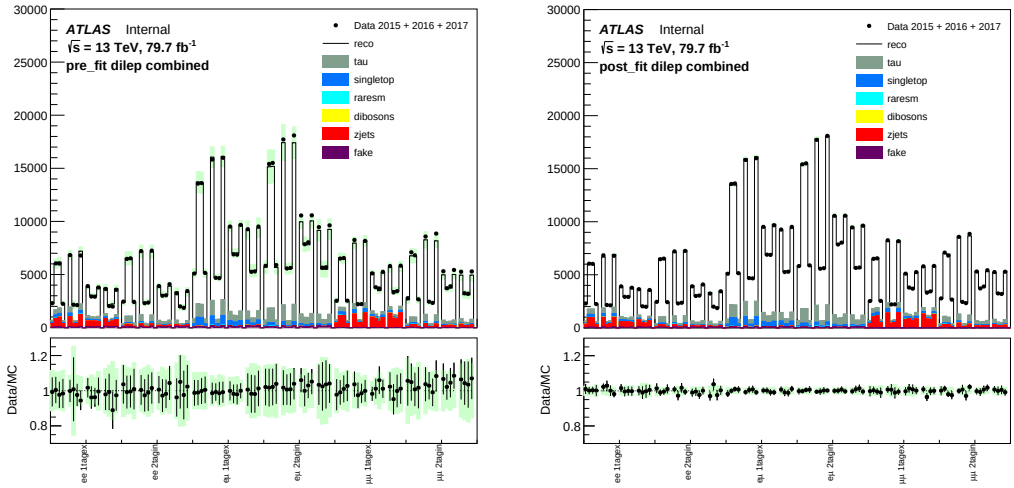

(a) Differential $\beta_{z,t\bar{t}}$ pre-fit (b) Differential $\beta_{z,t\bar{t}}$ post-fit

Figure 8.4: Comparison between data and prediction for bins used in the differential as function of $\beta_{z,t\bar{t}}$ (bottom) A_{C} measurements. This comparison is shown before (left, labeled as pre-fit) and after (right, labeled as post-fit) marginalization within FBU.

Chapter 9

Results

At first, the sensitivity of $t\bar{t}$ charge asymmetry after unfolding is discribed. The sensitivities of the inclusive and differential charge asymmetries in the simulated data corresponding to an intergrated luminosity of 79.7 fb^{-1}, together with the MC truth values as the green hatched regions are shown in Fig. 9.1. The red vertical var indicates the statistical uncertainty and the blue one refers to total uncertainty with the systematic uncertainty. The statistical unceratainties are caused by the statistic of MC simulation. The estimation of systematic uncertainties is used the Asimov data set. As mentioned in Chapter 8, the statistical uncertainties are more dominant than the systematic uncertainties in both inclusive and differential measurements. The systematic uncertaintiies are small enough for the statistics uncertaintiies. These unfolded $A_{\text{C}}^{t\bar{t}}$ mean values are in good agreement with the MC truth values.

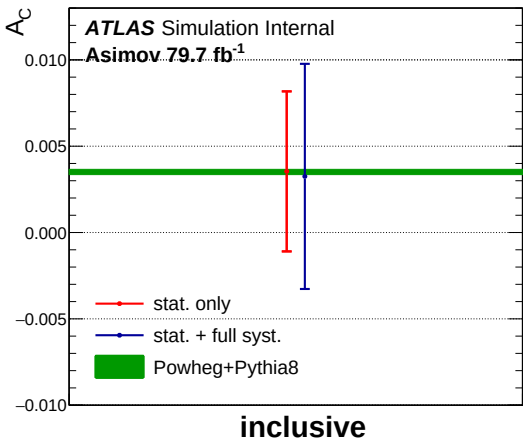

(a) Asimov test inclusive

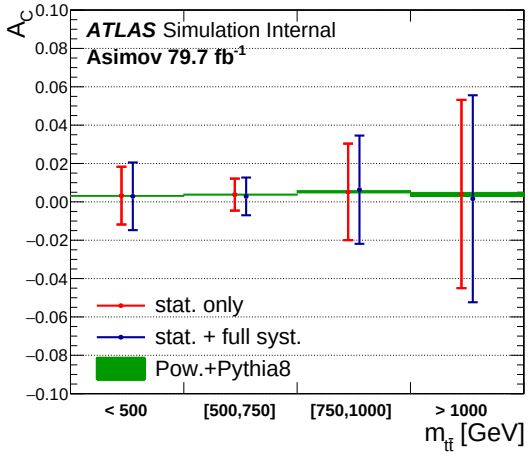

(b) Asimov test differential $m_{t\bar{t}}$

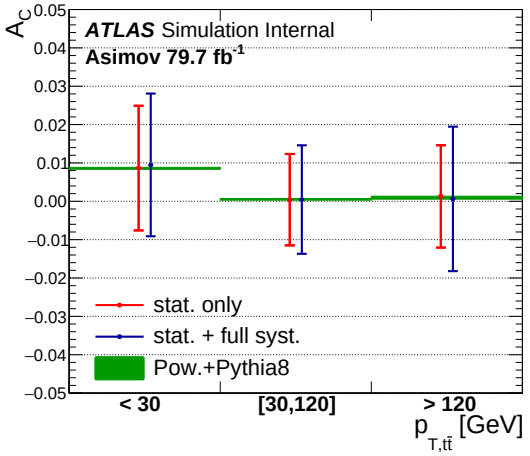

(c) Asimov test differential $p_{T,t\bar{t}}$

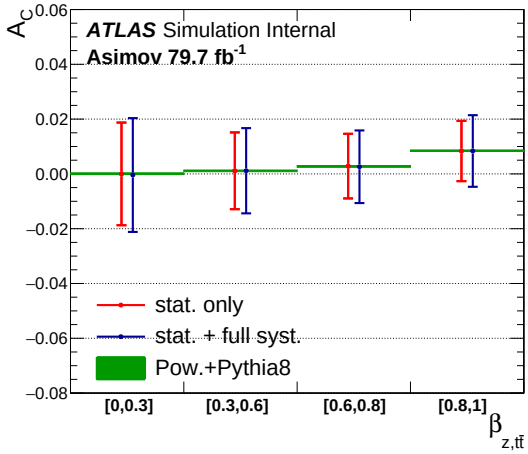

(d) Asimov test differential $\beta_{z,t\bar{t}}$

Figure 9.1: The sentitivities of inclusive and differential charge asymmetries as a function of the invariant mass, transverse momentum, and the transverse boost of the top pair system, from the Asimov data sample. The statistical uncertainties only (red) and total uncertainties (blue) are shown. Green hatched regions show MC truth values with the uncertainties, and vertical bars correspond to statistical and total uncertainties.

Finally, the $t\bar{t}$ charge asymmetry using the real data in an integrated luminosity of 79.7 fb^{-1} at $\sqrt{s} = 13\,\text{TeV}$, collected with the ATLAS detector is discribed. The inclusive and differential $t\bar{t}$ charge asymmetry measured in an integrated luminosity of 79.7 fb^{-1} using the MC simulation and collision data are shown in Table 9.1. In case of differential $m_{t\bar{t}}$ measurement, the result is combined as the highest $m_{t\bar{t}}$ bin with $m_{t\bar{t}} > 1000\,\text{GeV}$ because it is much less statistics in $m_{t\bar{t}} > 1500\,\text{GeV}$ as mentioned in Sec. 8.3. In both case of inclusive and differential measurements, the unfolded $A_C^{t\bar{t}}$ mean values using the MC truth values are consistant with the real data within total uncertaintiies.

Unfolded $A_{\mathrm{C}}^{t\bar{t}}$		MC simulation	Collision data (79.7 fb^{-1})
inclusive		0.0035 ± 0.0002	0.006 ± 0.006
$m_{t\bar{t}}$	< 500 GeV	0.0031 ± 0.0002	0.003 ± 0.017
	500-750 GeV	0.0038 ± 0.0002	0.012 ± 0.010
	750-1000 GeV	0.0053 ± 0.0006	−0.037 ± 0.027
	> 1000 GeV	0.0039 ± 0.0011	0.074 ± 0.052
$p_{T,t\bar{t}}$	< 30 GeV	0.0086 ± 0.0003	0.010 ± 0.018
	30-120 GeV	0.0005 ± 0.0002	0.011 ± 0.014
	> 120 GeV	0.0009 ± 0.0004	−0.018 ± 0.019
$\beta_{z,t\bar{t}}$	0-0.3	0.0001 ± 0.0003	−0.011 ± 0.021
	0.3-0.6	0.0011 ± 0.0003	0.004 ± 0.015
	0.6-0.8	0.0027 ± 0.0003	0.015 ± 0.013
	0.8-1.0	0.0085 ± 0.0003	0.014 ± 0.013

Table 9.1: Comparison of the inclusive and differential unfolded $A_{\mathrm{C}}^{t\bar{t}}$ in collision data (79.7 fb^{-1}) and MC simulation (MC truth values).

Chapter 10

Conclusion

The improvement of estimation method of the systematic uncertainties about the $t\bar{t}$ charge asymmetry in dilepton final states has been presented. In this thesis, to surpress systematic uncertainties, the uncertainties are estimated using *Fully Bayesian Unfolding* based on bayesian statistics. Here, the bayesian technique "marginalization" is used to deal with nuisance parameters affecting the measurement.

The inclusive and differential $t\bar{t}$ charge asymmetry measured using the collision data in an integrated luminosity of 79.7 fb^{-1} with the ATLAS detector at the LHC $\sqrt{s} = 13\,\text{TeV}$, are:

$$\begin{aligned} A_C^{t\bar{t}} &= 0.006 \pm 0.006(0.004(\text{stat. only})) \\ A_C^{t\bar{t}}\,(500\text{GeV} < m_{t\bar{t}} < 750\text{GeV}) &= 0.012 \pm 0.010(0.008(\text{stat. only})) \\ A_C^{t\bar{t}}\,(p_{\text{T}}^{t\bar{t}} > 120\text{GeV}) &= -0.018 \pm 0.019(0.013(\text{stat. only})) \\ A_C^{t\bar{t}}\,(0.8 < \beta_z^{t\bar{t}} < 1.0) &= 0.014 \pm 0.013(0.010(\text{stat. only})) \end{aligned}$$

For the result in $\sqrt{s} = 8\,\text{TeV}$, the inclusive $A_{\text{C}}^{t\bar{t}}$ value is 0.021 $\pm$ 0.016(0.011(stat.) $\pm$ 0.012(syst.)) [6]. The total uncertainty is about one-half smaller than the $\sqrt{s} = 8\,\text{TeV}$ result. The total uncertainty with systematic uncertainty is similar value to statstical uncertainty. Therefore, the systematic uncertainty has succeeded to reduce much small. In case of the differential measurements in the same way, the systematic uncertainties are also surpressed.

In this thesis, the $t\bar{t}$ charge asymmetry is estimated using not full statistics (140 fb^{-1}) of LHC Run-2 until 2018 but the statistics of LHC Run-2 of 2015-2017 years. By the Asimov data (79.7 fb^{-1}) extrapolated to 140 fb^{-1}, the inclusive $A_{\text{C}}^{t\bar{t}}$ uncertainty is expected to 0.0057(0.0035(stat. only)). As compared with the total uncertainties (0.0063) in the result this time, the precision of this measurement will be improved approximately 10% only. The differential measurements will also be improved in the same precision. For full Run-2 data (140 fb^{-1}), the $A_{\text{C}}^{t\bar{t}}$ meas-

urement can be reduced the statistics uncertainties, but needs to reconsider the estimation of systematic uncertainties to improve more precision.

To increase statistics more, the $t\bar{t}$ charge asymmetry is also measured in lepton+jets channel which has a leptonic W boson decay process ($t\bar{t} \to W^+bW^-\bar{b} \to q\bar{q}bl\bar{\nu}_l\bar{b}$). The lepton+jets channel has advantage to measure $A_C^{t\bar{t}}$ at much smaller statistics uncertainties than dilepton channels because this channel has branching ratio ($\sim$45%). However, the estimation of systematic uncertainties is difficult in this channel because there are QCD backgrounds caused by one side hadronic decay of W boson.

Acknowledgements

I would like to express gratitude to many people that have supported my Ph.D studies. First of all, I would like to express my gratitude to my supervisor, Prof. Hisaya Kurashige, for giving me a great opportunity for the research in the ATLAS experiment. His support and guidance were always encouraging me and leading me to the right way, throughout master and doctoral programs in Kobe University. Without his great help, my Ph.D thesis couldn't have got into shape. I'm also grateful to Prof. Yuji Yamazaki. He gave me many useful advices about the top quark physics analysis. I was able to analyze smoothly by his advice. I appreciates that Dr. Kentaro Kawade led me into this analysis group and help me accommodate my first physics analysis. I also thank him to support me an aspect of my living at CERN. I could spend profitable days for my study at CERN. For the same analysis team members, Jacob Julian Kempster, Miriam Watson, Robert Adam Vallance, Clement Helsens, Pavol Bartos, Matej Melo, and Oliver Majersky thank to them to help my study. Discussions with them have been extremely useful for my understanding and improvement of this analysis. I would like to extend my thanks to Dr. Junpei Maeda, who is the staff of the same experiment. I studied with him from the master's course to first grade of the doctoral course. He also provided me many advices about this study. In the case of traveling on business to CERN, I'm thanksful for Yumi Yokoyama and Kazumi Yoshida who have supported me. I also thanks to other staffs in the Kobe University Particle Physics Group, specially Prof. Yasuo Takeuchi, Prof. Kentaro Miuchi, Prof. Ochi Atsuhiko and Dr. Atsumu Suzuki. They taught a lot of knowledge about the particle physics.

I would like to extend my appreciations to the ATLAS Japan group. I'm thankful to Prof. Osamu Sasaki, Prof. Kunihiro Nagano, Prof. Masaya Ishino, Prof. Makoto Tomoto, Prof. Yasuyuki Okumura, Dr. Yasuyuki Horii, Dr. Masato Aoki, Dr. Toshi Sumida, Dr. Tatsuya Masubuchi and Dr. Tomoyuki Saito. Their organization and supports were essential for my research activities in the TGC group. I learned a lot of things in this group, detector operations, analyses using the data. For life at CERN, it is supported by a lot of colleagues, Dai Kobayashi, Kazuki Motohashi, Shota Suzuki, Takuto Kunigo, Kouta Onogi, Satoshi Higashino, Yuya Kano, Masahiro Yamatani, Tomohiro Yamazaki, Masahiko Saito, Masahiro Tanaka, Daiki Hayakawa, Sano Yuta, Kazuki Yajima, Atsushi Mizkami, Kenta Uno, Shunichi Akatsuka, Yohei Noguchi, Tomomi Kawaguchi, Yuta Okazaki and Kosuke Takeda.

In particular, I could spend in a meaningful way because I played a card game with Y. Sano and played tennis with my colleagues on weekends.

Finally, I would like to express my deepest thanks to my family. In particular, I thank greatly for my parents and cat that I had before. Unfortunately the cat I loved died in October 2017 when I had stayed at the CERN. I have been encouraged during a long stay at CERN with the photo such as shown in the Fig 10.1. I couldn't spend my research life without their supports.

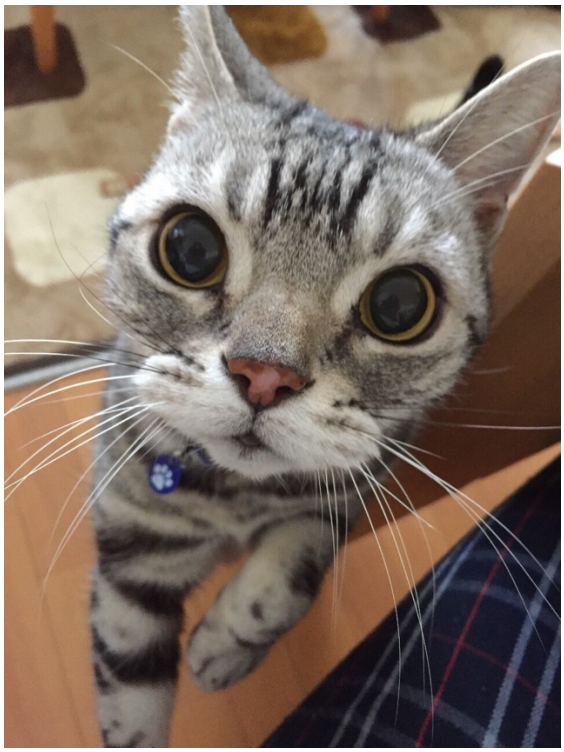

Figure 10.1: A photograph of my cat. The cat's name is Leon. I think that it may be fateful, Leon hides in the dilepton channels which I focuses on this analysis. (di*le*pt*on* channels)

Shogo Kido
January, 2019

Bibliography

[1] P. W. Higgs, *Broken symmetries, massless particles and gauge fields*, Phys.Lett. **12** (1964) 132.

[2] F. Englert and R. Brout, *Broken Symmetry and the Mass of Gauge Vector Mesons*, Phys. Rev. Lett. **13** (1964) 321.

[3] O. Antunano, J. H. Kuhn and G. Rodrigo, *Top quarks, axigluons and charge asymmetries at hadron colliders*, Phys. Rev. **D77** (2008) 014003, arXiv: 0709.1652 [hep-ph].

[4] ATLAS Collaboration, *Measurements of top-quark pair to Z-boson cross-section ratios at $\sqrt{s} = 13, 8, 7$ TeV with the ATLAS detector*, JHEP **02** (2017) 117, arXiv: 1612.03636 [hep-ex].

[5] J. H. Kühn and G. Rodrigo, *Charge asymmetry of heavy quarks at hadron colliders*, Phys.Rev. **D59** (1998), arXiv: hep-ph/9807420 [hep-ph].

[6] ATLAS Collaboration, *Measurements of the charge asymmetry in top-quark pair production in the dilepton final state at $\sqrt{s} = 8$ TeV with the ATLAS detector*, Phys. Rev. D **94** (2016) 032006, arXiv: 1604.05538 [hep-ex].

[7] M. Aaboud et al., *Combination of inclusive and differential $\mathrm{t\bar{t}}$ charge asymmetry measurements using ATLAS and CMS data at $\sqrt{s} = 7$ and 8 TeV*, Submitted to: JHEP (2017), arXiv: 1709.05327 [hep-ex].

[8] W. Bernreuther and Z.-G. Si, *Top quark and leptonic charge asymmetries for the Tevatron and LHC*, Phys. Rev. **D86** (2012) 034026, arXiv: 1205.6580 [hep-ph].

[9] J. M. Meyer, 'Measurement of the Top Quark Mass using Dilepton Events and a Neutrino We§ighting Algorithm with the D0 Experiment at the Tevatron (Run II)', PhD thesis: Bonn U., 2007, URL: http://lss.fnal.gov/cgi-bin/find_paper.pl?thesis-2007-65.

[10] G.Choudalakis, *Fully Bayesian Unfolding*, (2012), arXiv: 1201.4612 [hep-ex].

[11] *Standard Model*, https://www.physik.uzh.ch/en/researcharea/lhcb/outreach/StandardModel.html.

[12] CDF Collaboration,
Observation of Top Quark Production in Pbar-P Collisions,
Phys.Rev.Lett. **74** (1995), arXiv: hep-ex/9503002 [hep-ex].

[13] S. Abachi, et al. D0 Collaboration, *Observation of the Top Quark*,
Phys.Rev.Lett. **74** (1995), arXiv: hep-ex/9503003 [hep-ex].

[14] N. Cabibbo, *Unitary Symmetry and Leptonic Decays*,
Phys.Lett. **10** (1963) 531.

[15] M. Kobayashi and T. Maskawa,
CP-Violation in the Renormalizable Theory of Weak Interaction,
Prog.Theor.Phys. **49** (1973) 652.

[16] G. Rodrigo and P. Ferrario, *Charge asymmetry: A Theory appraisal*,
Nuovo Cim. C **33** (2010) 221, arXiv: arXiv:1007.4328 [hep-ph].

[17] P. H. Frampton and S. L. Glashow,
Chiral color: An alternative to the standard model,
Phys.Lett.B **190** (1987) 157.

[18] P. Ferrario and G. Rodrigo, *Massive color-octet bosons and the charge asymmetries of top quarks at hadron colliders*, Phys. Rev. D **78** (2008),
arXiv: arXiv:0809.3354 [hep-ph].

[19] P. Ferrario and G. Rodrigo,
Constraining heavy colored resonances from top-antitop quark events,
Phys. Rev. D **80** (2009), arXiv: arXiv:0906.5541 [hep-ph].

[20] ATLAS and CMS Collaborations,
Combination of inclusive and differential $t\bar{t}$ charge asymmetry measurements using ATLAS and CMS data at $\sqrt{s} = 7$ TeV and 8 TeV,
JHEP **04** (2018) 033, arXiv: 1709.05327 [hep-ex].

[21] ATLAS Collaboration, *Measurement of the charge asymmetry in highly boosted top-quark pair production in $\sqrt{s} = 8$ TeV pp collision data collected by the ATLAS experiment*, Phys. Lett. **B756** (2016) 52,
arXiv: 1512.06092 [hep-ex].

[22] M. P. Rosello and M. Vos, *Constraints on four-fermion interactions from the $t\bar{t}$ charge asymmetry at hadron colliders*, Eur. Phys. J. **C76** (2016) 200,
arXiv: 1512.07542 [hep-ex].

[23] *CERN Media Archive Photo*,
https://mediastream.cern.ch/MediaArchive/Photo/Public/2008/0812015/0812015/0812015-A4-at-144-dpi.jpg.

[24] ATLAS Collaboration,
Studies of the performance of the ATLAS detector using cosmic-ray muons,
Eur. Phys. J. **C71** (2011), arXiv: arXiv:1011.6665 [hep-ex].

[25] C. Kourkoumelis and S. Vourakis,
HYPATIA—an online tool for ATLAS event visualization,
Phys.Educ. **49** (2014).

[26] J. J. Goodson, 'Search for Supersymmetry in States with Large Missing Transverse Momentum and Three Leptons including a Z-Boson',
PhD thesis: Stony Brook U., 2012, URL: https://cds.cern.ch/record/1449722/files/CERN-THESIS-2012-053.pdf.

[27] ATLAS Collaboration,
The ATLAS Experiment at the CERN Large Hadron Collider,
JINST **3** (2008) S08003.

[28] ATLAS Collaboration,
Study of the material of the ATLAS inner detector for Run 2 of the LHC,
JINST **12** (2017), arXiv: arXiv:1707.02826 [hep-ex].

[29] ATLAS Collaboration, *Track Reconstruction Performance of the ATLAS Inner Detector at* $\sqrt{s} = 13$ *TeV*, ATL-PHYS-PUB-2015-018, 2015,
URL: https://cds.cern.ch/record/2037683.

[30] *ATLAS Experiment - Photos*, http://atlasexperiment.org/photos/calorimeters-combined-endcap.html.

[31] M. Aharrouche et al, ATLAS Electromagnetic Barrel Calorimeter Collaboration, *Energy Linearity and Resolution of the ATLAS Electromagnetic Barrel Calorimeter in an Electron Test-Beam*,
Nucl. Instrum. Meth A **568** (2006),
arXiv: arXiv:physics/0608012 [physics.ins-det].

[32] ATLAS Collaboration, *Electron and photon energy calibration with the ATLAS detector using data collected in 2015 at* $\sqrt{s} = 13$ *TeV*,
ATL-PHYS-PUB-2016-015, 2016,
URL: https://cds.cern.ch/record/2203514.

[33] T. H. Park, 'Jet energy resolution measurement of the ATLAS detector using momentum balance', PhD thesis: Carleton U., 2018, URL: https://cds.cern.ch/record/2642494/files/CERN-THESIS-2018-187.pdf.

[34] A. Salvucci,
Measurement of muon momentum resolution of the ATLAS detector,
(2012), arXiv: arXiv:1201.4704 [physics.ins-det].

[35] ATLAS Collaboration, *Performance of the ATLAS trigger system in 2015*,
Eur. Phys. J. C **77** (2017) 317, arXiv: 1611.09661 [hep-ex].

[36] ATLAS Collaboration, *2015 start-up trigger menu and initial performance assessment of the ATLAS trigger using Run-2 data*, ATL-DAQ-PUB-2016-001, 2016, URL: https://cds.cern.ch/record/2136007.

[37] S. van der Meer, *Calibration of the effective beam height in the ISR*, https://cds.cern.ch/record/296752, 1968.

[38] ATLAS Collaboration, *Improved luminosity determination in pp collisions at $\sqrt{s} = 7$ TeV using the ATLAS detector at the LHC*, Eur. Phys. J. C **73** (2013) 2518, arXiv: 1302.4393 [hep-ex].

[39] ATLAS Collaboration, *Luminosity determination in pp collisions at $\sqrt{s} = 8$ TeV using the ATLAS detector at the LHC*, Eur. Phys. J. C **76** (2016) 653, arXiv: 1608.03953 [hep-ex].

[40] M. A. Dobbs, *Les Houches Guidebook to Monte Carlo Generators for Hadron Collider Physics*, (2004), arXiv: arXiv:hep-ph/0403045 [hep-ex].

[41] S. Agostinelli et al., *Geant4a simulation toolkit*, Nuclear Instruments and Methods in Physics Research Section A: Accelerators, Spectrometers, Detectors and Associated Equipment **506** (2003) 250, ISSN: 0168-9002, URL: http://www.sciencedirect.com/science/article/pii/S0168900203013688.

[42] S. Alioli, P. Nason, C. Oleari and E. Re, *A general framework for implementing NLO calculations in shower Monte Carlo programs: the POWHEG BOX*, JHEP **06** (2010) 043, arXiv: 1002.2581 [hep-ph].

[43] T. Sjostrand, S. Mrenna and P. Z. Skands, *A Brief Introduction to PYTHIA 8.1*, Comput. Phys. Commun. **178** (2008) 852, arXiv: 0710.3820 [hep-ph].

[44] E. Richter-Was, D. Froidevaux and L. Poggioli, *ATLFAST 2.0 a fast simulation package for ATLAS*, tech. rep. ATL-PHYS-98-131, CERN, 1998, URL: https://cds.cern.ch/record/683751.

[45] J. Alwall et al., *The automated computation of tree-level and next-to-leading order differential cross sections, and their matching to parton shower simulations*, JHEP **07** (2014) 079, arXiv: 1405.0301 [hep-ph].

[46] J. Bellm et al., *Herwig 7.0/Herwig++ 3.0 release note*, Eur. Phys. J. **C76** (2016) 196, arXiv: 1512.01178 [hep-ph].

[47] ATLAS Collaboration,
Expected electron performance in the ATLAS experiment,
ATL-PHYS-PUB-2011-006, 2011,
URL: https://cds.cern.ch/record/1345327.

[48] ATLAS Collaboration, *Electron efficiency measurements with the ATLAS detector using 2012 LHC proton-proton collision data*,
Eur. Phys. J. **C77** (2017) 64, arXiv: 1612.01456 [hep-ex].

[49] ATLAS Collaboration, *Muon reconstruction performance of the ATLAS detector in proton-proton collision data at* $\sqrt{s} = 13$ *TeV*,
Eur. Phys. J. **C76** (2016) 44, arXiv: 1603.05598 [hep-ex].

[50] M. Cacciari, G. P. Salam and G. Soyez,
The Anti-k(t) jet clustering algorithm, JHEP **04** (2008) 063,
arXiv: 0802.1189 [hep-ph].

[51] W. Lampl et al.,
Calorimeter Clustering Algorithms: Description and Performance,
tech. rep. ATL-LARG-PUB-2008-002. ATL-COM-LARG-2008-003,
CERN, 2008, URL: https://cds.cern.ch/record/1099735.

[52] ATLAS Collaboration,
Expected performance of the ATLAS b-tagging algorithms in Run-2,
ATL-PHYS-PUB-2015-022, 2015,
URL: https://cds.cern.ch/record/2037697.

[53] I. Connelly, 'Performance and calibration of b-tagging with the ATLAS experiment at LHC Run-2',
5th International Conference on New Frontiers in Physics,
ATL-PHYS-PROC-2016-193, 2016,
URL: https://cds.cern.ch/record/2229557.

[54] ATLAS Collaboration,
Tagging and suppression of pileup jets with the ATLAS detector,
ATLAS-CONF-2014-018, 2014,
URL: https://cds.cern.ch/record/1700870.

[55] D. Adams et al., *Recommendations of the Physics Objects and Analysis Harmonisation Study Groups 2014*, tech. rep. ATL-PHYS-INT-2014-018,
CERN, 2014, URL: https://cds.cern.ch/record/1743654.

[56] ATLAS Collaboration,
Top-antitop charge asymmetry at 13 TeV with the ATLAS Detector,
ATL-COM-PHYS-2018-636, 2018,
URL: https://cds.cern.ch/record/2319913.

[57] ATLAS Collaboration,
Performance of missing transverse momentum reconstruction with the ATLAS detector in the first proton–proton collisions at $\sqrt{s} = 13$ *TeV*,
ATL-PHYS-PUB-2015-027, 2015,
URL: https://cds.cern.ch/record/2037904.

[58] J. Erdmann et al., *A likelihood-based reconstruction algorithm for top-quark pairs and the KLFitter framework*, Nucl. Instrum. Meth. **A748** (2014) 18,
arXiv: 1312.5595 [hep-ex].

[59] P. Diaconis, *The Markov Chain Monte Carlo Revolution*,
Bull. Amer. Math. Soc. (N.S.) **46** (2009) 179.

[60] N. Metropolis, A. W. Rosenbluth, M. N. Rosenbluth, A. H. Teller and E. Teller, *Equation of State Calculations by Fast Computing Machines*,
The Journal of Chemical Physics **21** (1953) 1087,
eprint: https://doi.org/10.1063/1.1699114,
URL: https://doi.org/10.1063/1.1699114.

[61] M. D. Hoffman and A. Gelman, *The No-U-Turn Sampler: Adaptively Setting Path Lengths in Hamiltonian Monte Carlo*, ArXiv e-prints (2011),
arXiv: 1111.4246 [stat.CO].

[62] J. Salvatier, T. V. Wiecki, C. Fonnesbeck,
Probabilistic programming in Python using PyMC3,
PeerJ Computer Science **2:e55** (2016),
URL: https://doi.org/10.7717/peerj-cs.55.

[63] ATLAS Collaboration, *Measurement of the charge asymmetry in highly boosted top-quark pair production in* $\sqrt{s} = 8$ *TeV pp collision data collected by the ATLAS experiment*, Phys. Lett. B **756** (2016) 52,
arXiv: 1512.06092 [hep-ex].

[64] J. A. Aguilar-Saavedra,
Single top quark production at LHC with anomalous Wtb couplings,
Nucl. Phys. **B804** (2008) 160, arXiv: 0803.3810 [hep-ph].

[65] W. Buttinger, 'Extended Pileup Reweighting', 2018,
URL: https://twiki.cern.ch/twiki/bin/viewauth/AtlasProtected/ExtendedPileupReweighting.

[66] ATLAS Collaboration, *Electron efficiency measurements with the ATLAS detector using the 2015 LHC proton–proton collision data*,
ATLAS-CONF-2016-024, 2016,
URL: https://cds.cern.ch/record/2157687.

[67] ATLAS Collaboration, *Muon reconstruction performance of the ATLAS detector in proton–proton collision data at* $\sqrt{s} = 13$ *TeV*,
Eur. Phys. J. C **76** (2016) 292, arXiv: 1603.05598 [hep-ex].

[68] ATLAS Collaboration, *Electron and photon energy calibration with the ATLAS detector using LHC Run 1 data*, Eur. Phys. J. C **74** (2014) 3071, arXiv: 1407.5063 [hep-ex].

[69] ATLAS Collaboration, *Jet energy measurement with the ATLAS detector in proton–proton collisions at* $\sqrt{s} = 7$ *TeV*, Eur. Phys. J. C **73** (2013) 2304, arXiv: 1112.6426 [hep-ex].

[70] ATLAS Collaboration, *Jet Calibration and Systematic Uncertainties for Jets Reconstructed in the ATLAS Detector at* $\sqrt{s} = 13$ *TeV*, ATL-PHYS-PUB-2015-015, 2015, URL: https://cds.cern.ch/record/2037613.

[71] ATLAS Collaboration, *Jet energy resolution in proton–proton collisions at* $\sqrt{s} = 7$ *TeV recorded in 2010 with the ATLAS detector*, Eur. Phys. J. C **73** (2013) 2306, arXiv: 1210.6210 [hep-ex].

[72] ATLAS Collaboration, *Monte Carlo Calibration and Combination of In-situ Measurements of Jet Energy Scale, Jet Energy Resolution and Jet Mass in ATLAS*, ATLAS-CONF-2015-037, 2015, URL: https://cds.cern.ch/record/2044941.

[73] ATLAS Collaboration, *Identification of Boosted, Hadronically Decaying W Bosons and Comparisons with ATLAS Data Taken at* $\sqrt{s} = 8$ *TeV*, Eur. Phys. J. C **76** (2016) 154, arXiv: 1510.05821 [hep-ex].

[74] ATLAS Collaboration, *In-situ measurements of the ATLAS large-radius jet response in* 13 *TeV pp collisions*, ATLAS-CONF-2017-063, 2017, URL: https://cds.cern.ch/record/2275655.

[75] ATLAS Collaboration, *Performance of Missing Transverse Momentum Reconstruction in ATLAS studied in Proton–Proton Collisions recorded in 2012 at* $\sqrt{s} = 8$ *TeV*, ATLAS-CONF-2013-082, 2013, URL: https://cds.cern.ch/record/1570993.

[76] J. Rojo, *PDF4LHC recommendations for Run II*, PoS **DIS2016** (2016) 018, arXiv: 1606.08243 [hep-ph].

[77] G. Bohm and G. Zech, *Introduction to Statistics and Data Analysis for Physicists; 2nd rev. ed.* Verlag Deutsches Elektronen-Synchrotron, 2014, ISBN: 978-3-935702-88-1, URL: http://bib-pubdb1.desy.de/record/169869.

[78] G. Aad and etal, *Measurement of dijet cross-sections in pp collisions at 7 TeV centre-of-mass energy using the ATLAS detector*, Journal of High Energy Physics **2014** (2014) 59, ISSN: 1029-8479, URL: https://doi.org/10.1007/JHEP05(2014)059.

Appendix A

Control plots

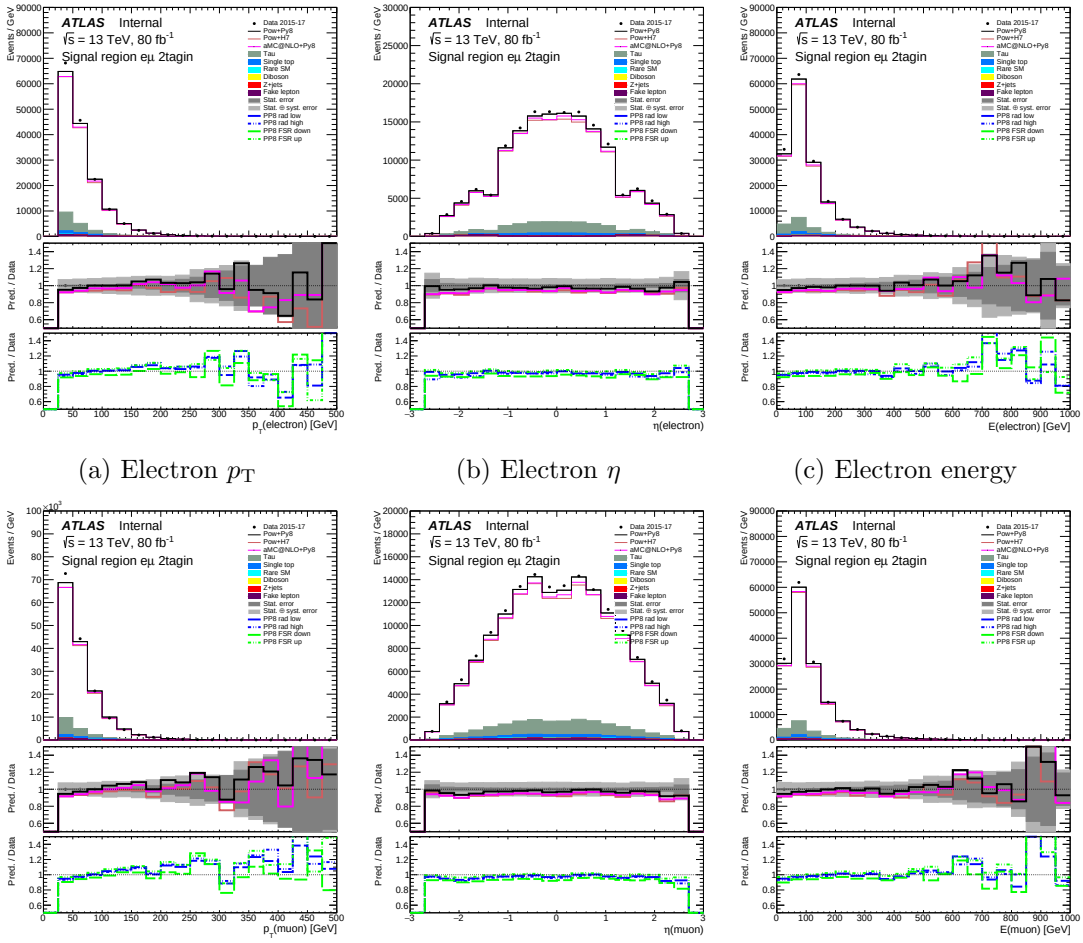

(a) Electron p_{T} (b) Electron η (c) Electron energy

(d) Muon p_{T} (e) Muon η (f) Muon energy

Figure A.1: A comparison of the observed data and prediction for the individual lepton properties in the $e\mu$ 2-b incl. channel. The bottom panels show the ratio of MC to data predictions.

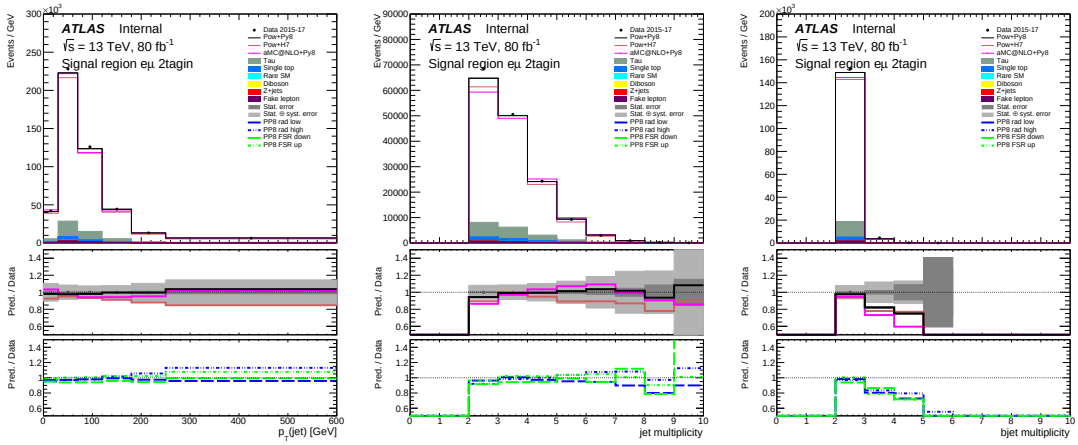

(a) Jet p_{T} (b) Jet multiplicity (c) b-jet multiplicity

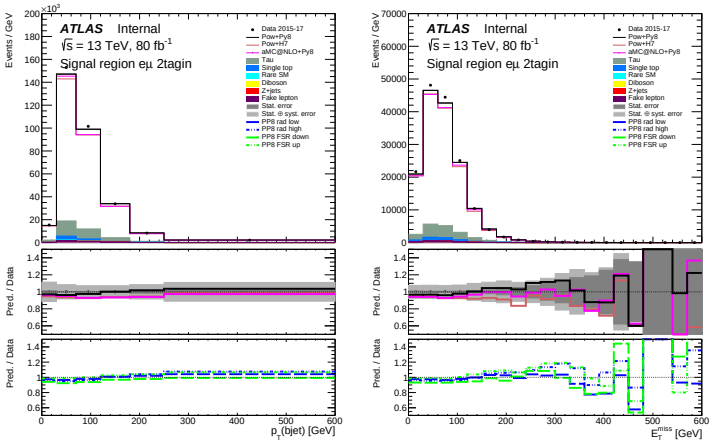

(d) b-jet p_{T} (e) $E_{\mathrm{T}}^{\mathrm{miss}}$

Figure A.2: A comparison of the observed data and prediction for the jet and $E_{\mathrm{T}}^{\mathrm{miss}}$ properties in the $e\mu$ $2b$ incl. channel. The bottom panels show the ratio of MC to data predictions.

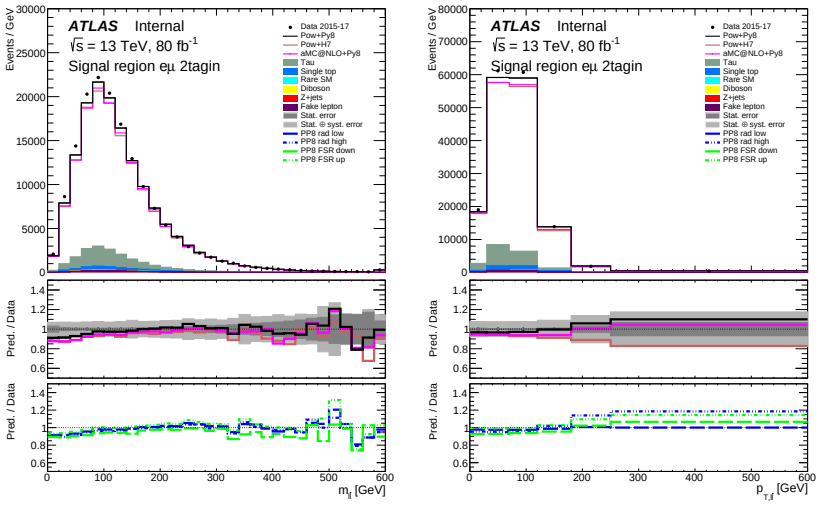

(a) Dilepton invariant mass, $m_{l\bar{l}}$ (b) Dilepton transverse momentum, $p_{T,l\bar{l}}$

Figure A.3: A comparison of the observed data and prediction for the dilepton properties in the $e\mu$ 2-b incl. channel. The bottom panels show the ratio of MC to data predictions.

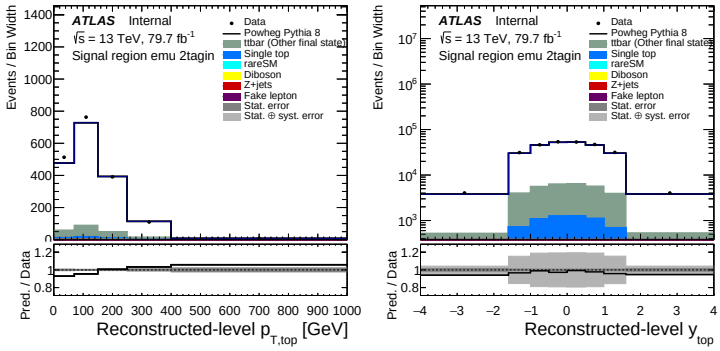

(a) top p_{T} (b) top y

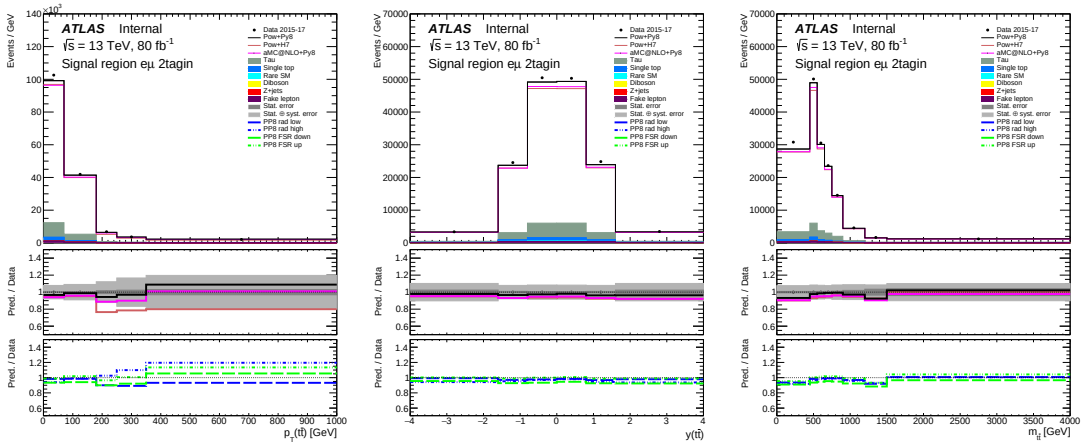

(c) top pair p_{T} (d) top pair y (e) top pair mass

Figure A.4: A comparison of the observed data and prediction for the top-quark and top-pair properties in the $e\mu$ 2-b incl. channel. The bottom panels show the ratio of data to MC predictions.

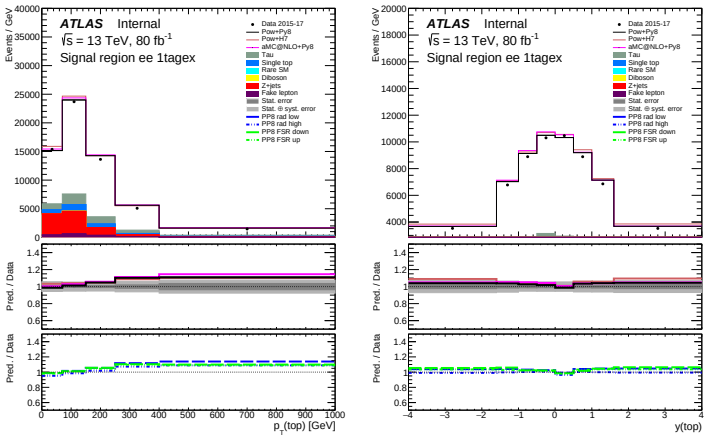

(a) top p_{T} (b) top y

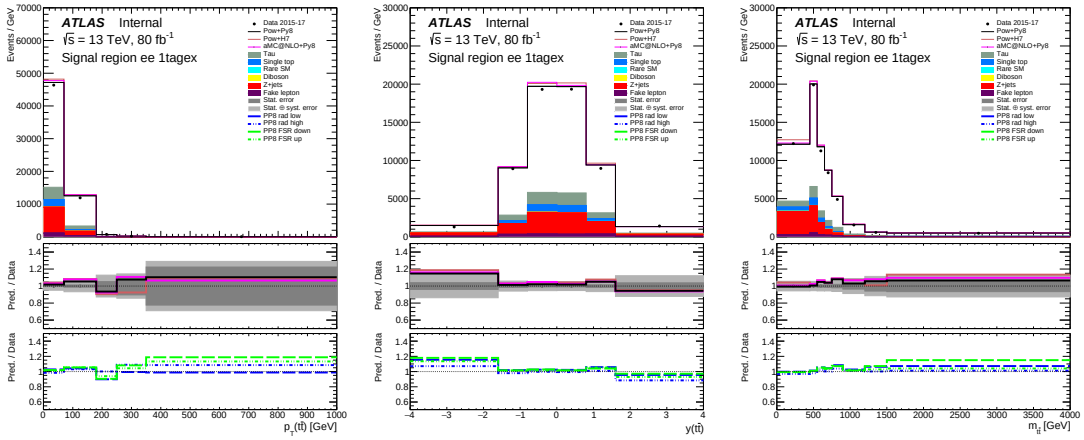

(c) top pair p_{T} (d) top pair y (e) top pair mass

Figure A.5: A comparison of the observed data and prediction for the top-quark and top-pair properties in the *ee* 1-*b* excl. channel. The bottom panels show the ratio of data to MC predictions.

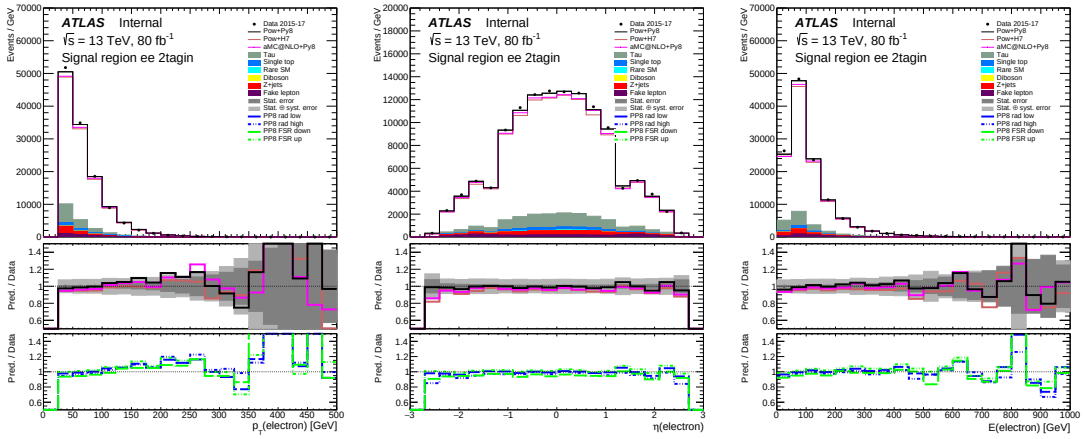

(a) Electron p_{T} (b) Electron η (c) Electron energy

Figure A.6: A comparison of the observed data and prediction for the individual lepton properties in the ee 2-b incl. channel. The bottom panels show the ratio of MC to data predictions.

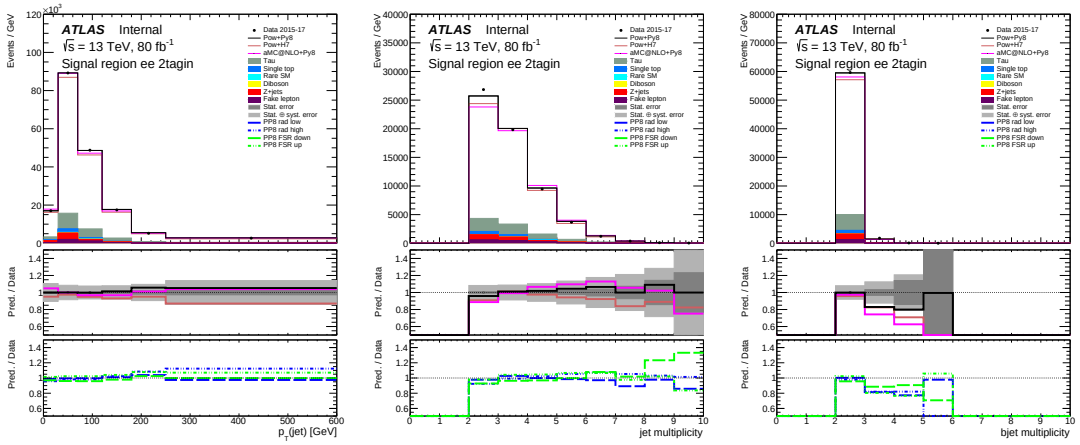

(a) Jet p_{T} (b) Jet multiplicity (c) b-jet multiplicity

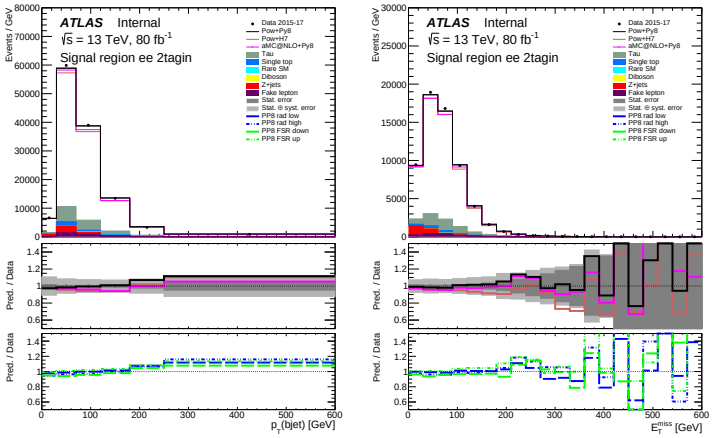

(d) b-jet p_{T} (e) $E_{\mathrm{T}}^{\mathrm{miss}}$

Figure A.7: A comparison of the observed data and prediction for the jet and $E_{\mathrm{T}}^{\mathrm{miss}}$ properties in the ee 2-b incl. channel. The bottom panels show the ratio of MC to data predictions.

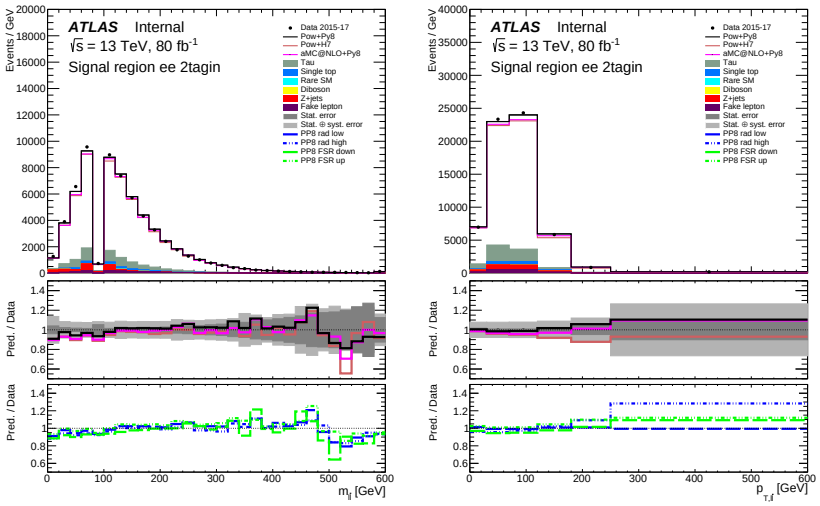

(a) Dilepton invariant mass, $m_{l\bar{l}}$ (b) Dilepton transverse momentum, $p_{T,l\bar{l}}$

Figure A.8: A comparison of the observed data and prediction for the dilepton properties in the *ee* 2-*b* incl. channel. The bottom panels show the ratio of MC to data predictions.

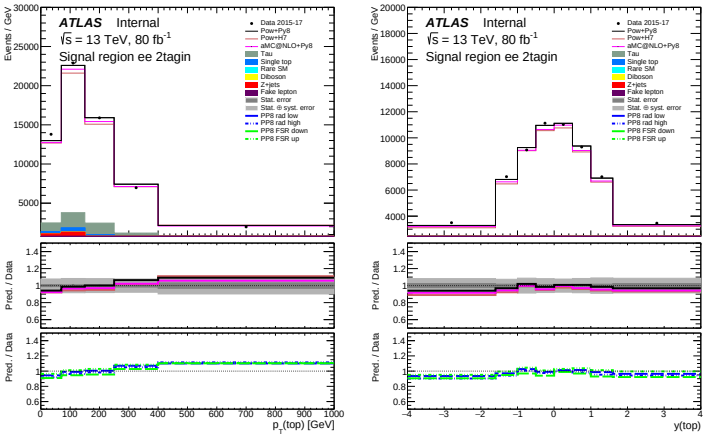

(a) top p_{T} (b) top y

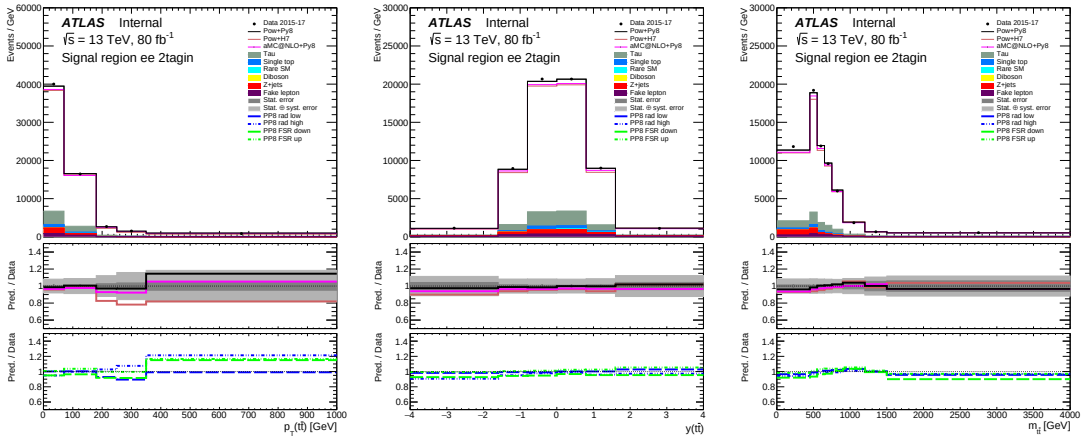

(c) top pair p_{T} (d) top pair y (e) top pair mass

Figure A.9: A comparison of the observed data and prediction for the top-quark and top-pair properties in the *ee* 2-*b* incl. channel. The bottom panels show the ratio of data to MC predictions.

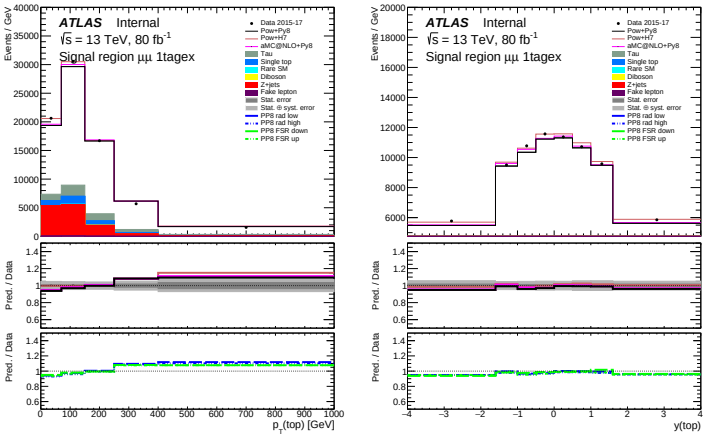

(a) top p_{T} (b) top y

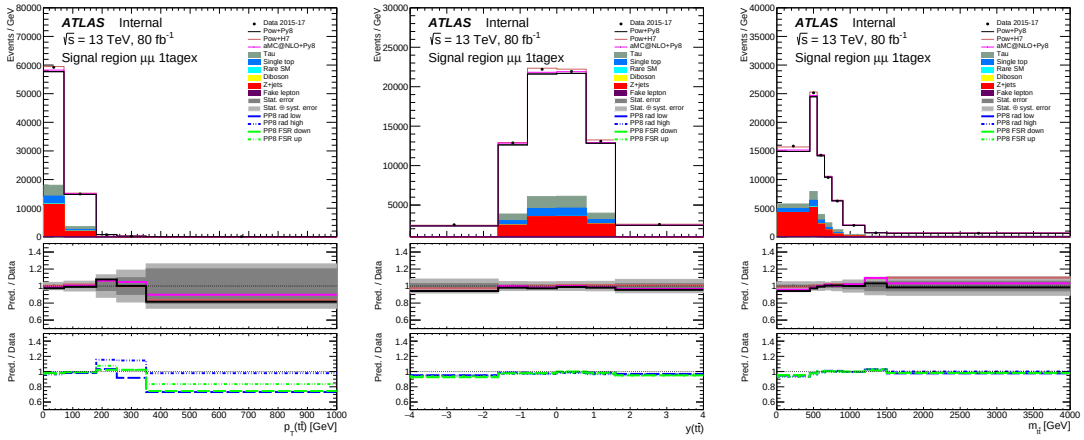

(c) top pair p_{T} (d) top pair y (e) top pair mass

Figure A.10: A comparison of the observed data and prediction for the top-quark and top-pair properties in the $\mu\mu$ 1-b excl. channel. The bottom panels show the ratio of data to MC predictions.

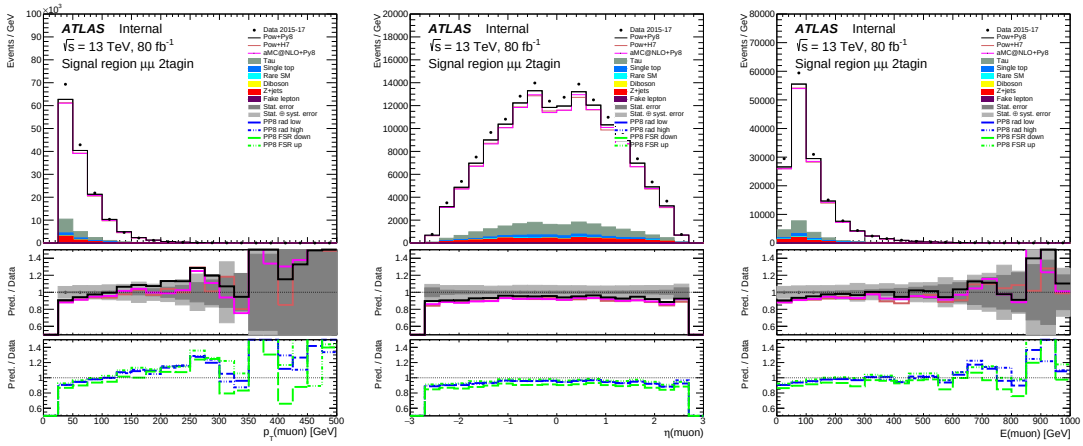

(a) Muon p_{T} (b) Muon η (c) Muon energy

Figure A.11: A comparison of the observed data and prediction for the individual lepton properties in the $\mu\mu$ 2-b incl. channel. The bottom panels show the ratio of MC to data predictions.

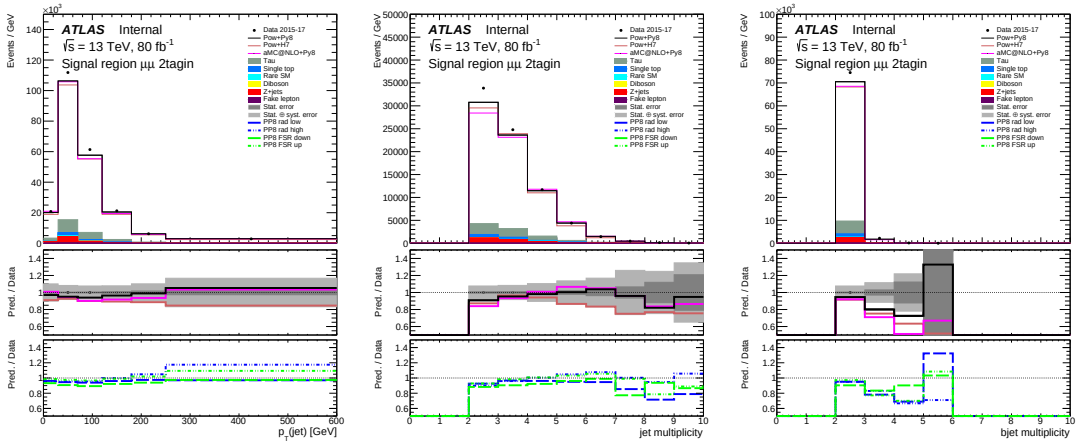

(a) Jet p_{T} (b) Jet multiplicity (c) b-jet multiplicity

(d) b-jet p_{T} (e) $E_{\mathrm{T}}^{\mathrm{miss}}$

Figure A.12: A comparison of the observed data and prediction for the jet and $E_{\mathrm{T}}^{\mathrm{miss}}$ properties in the $\mu\mu$ 2-b incl. channel. The bottom panels show the ratio of MC to data predictions.

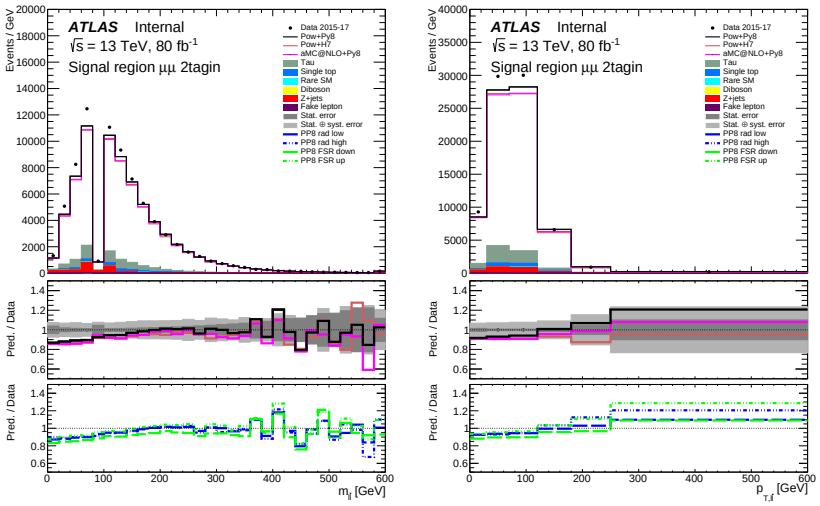

(a) Dilepton invariant mass, $m_{l\bar{l}}$ (b) Dilepton transverse momentum, $p_{T,l\bar{l}}$

Figure A.13: A comparison of the observed data and prediction for the dilepton properties in the $\mu\mu$ 2-b incl. channel. The bottom panels show the ratio of MC to data predictions.

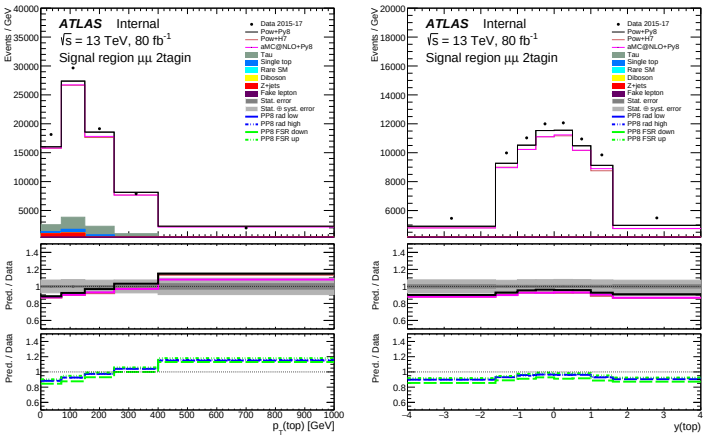

(a) top p_{T} (b) top y

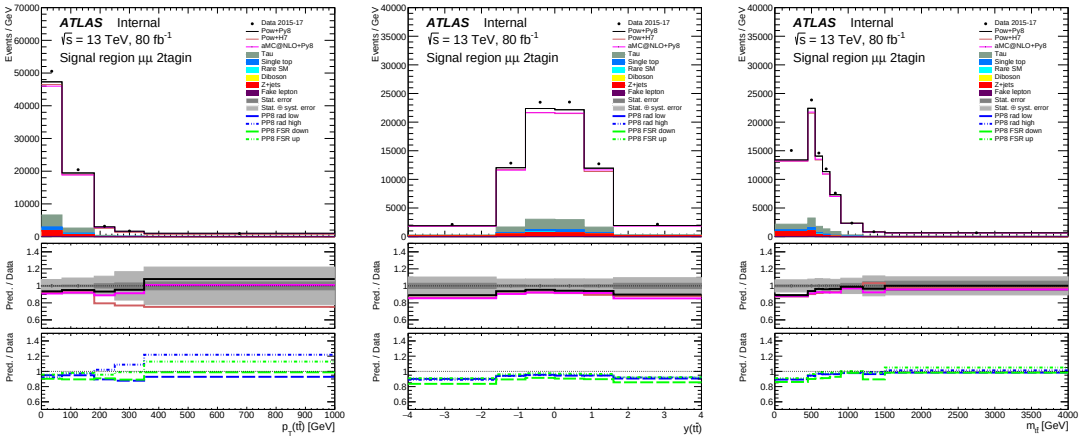

(c) top pair p_{T} (d) top pair y (e) top pair mass

Figure A.14: A comparison of the observed data and prediction for the top-quark and top-pair properties in the $\mu\mu$ 2-b incl. channel. The bottom panels show the ratio of data to MC predictions. The error bars on data points are statistical error only.

Appendix B

Kinematic Likelihood method

The Kinematic Likelihood Fitter (KLFitter) [58] reconstructs the $t\bar{t}$ system using a likelihood approach. It is designed to permute objects (leptons, jets) observed in an event between each possible location in a given decay topology and for each permutation calculate a likelihood with parameters usually set by:

- Transfer functions for the energies and angular measurements of the objects
  - The probability of measuring a certain value for an observable, given the true value of the associated model parameter. These are derived from MC, and depend on the type of objects and η-region and are motivated by detector geometry.
- Breit-Wigner functions
  - These provide constraints based on particle mass.

The likelihood is used to determine the agreement between the reconstructed event and the decay model signature. For each permutation of objects, the likelihood function is maximised during the fit. After all permutations are considered, a probability is calculated for each and the 'best permutation' is identified, which is considered to represent the most likely association of measured objects to decay products within the model as well as their fitted four-vectors.

In the dilepton channel, the system is under-constrained due to the unknown neutrino kinematics. A neutrino-weighting method is utilised alongside the four-momenta of two jets and two charged leptons. The likelihood uses transfer functions $W(...)$ for the leptons and jets, as well as Gaussian Functions $G(...)$ to describe the transfer functions of the missing transverse momentum as a function of the ntrunio four-momenta and the probability density function of the neutrino pseudoradidity distributions [58].

$$\mathcal{L} = \prod_{x,y} G(E_i^{\text{miss}} | p_i^{\nu_1}, p_i^{\nu_2}, \sigma_i^{\text{miss}}(m_t, m_W, \eta_{\nu_1}, \eta_{\nu_2})) \cdot \prod_{i=1}^{2} G(\eta_{\nu_i} | m_t) \cdot (m_{\ell_1,q_1} + m_{\ell_2,q_2})^{\alpha} \cdot \prod_{i=1}^{2} W_{\text{jet}}(E_{\text{jet},i}^{\text{meas}} | E_{\text{jet},i}) \cdot \prod_{i=1}^{2} W_{\ell}(E_{\ell,i}^{\text{meas}} | E_{\ell,i}) \tag{B.1}$$

The probability density functions for the neutrino pseudorapidities distributions have a dependence on the top mass which is assumed to be linear.

This method shows comparable performance with NW, but at a higher CPU cost. Due to the substantial increase in required processing time the KLFitter is not utilised for this analysis.

Appendix C

Comparison of NW and KLF

Two $t\bar{t}$ reconstruction algorithms were considered for the analysis: the Neutrino Weighter (NW) and Kinematic Likelihood Fitter (KLFitter). These were tested using the AnalysisTop Release 20 framework with the old nominal $t\bar{t}$ sample. The best performing algorithm was then used for the Release 21 analysis.

As a first test, it was seen how stable the two methods would be against reconstructed variables such as lepton and $t\bar{t}$ p_{T}, pseudorapidity (η) and azimuthal angle (ϕ) quantities. The events were required to match up according to run number and event number. The performance variable on the y-axis was the mean rapidity difference between the top and antitop at reconstruction level minus that at parton (truth) level. This is labelled Mean $t\bar{t}$ _dy_RES. The idea was to see if this resolution deviated from 0 as a function of this variable and if cuts could therefore be placed on the variable to improve the overall performance. Some original cuts in place were the requirement of one lepton to have a transverse momentum, p_{T} $>$ 28 GeV (to pass the High-Level Trigger), and the other electron a $p_{\mathrm{T}} > 25$ GeV. Greater than 1 jet and greater than 0 b-tagged jets at 77 % efficiency were also required per event. The NW and KLFitter required their event reconstruction quality parameters (d_weight_max and log-likelihood variables) to be > 0. Fig. C.1-C.4 shows the stabilities for a range of reconstructed variables.

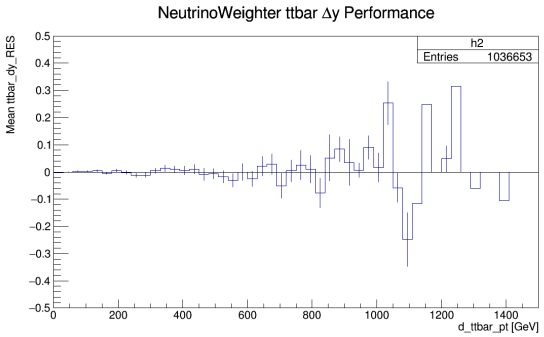

Figure C.1: NW resolution for $t\bar{t}$ p_{T}.

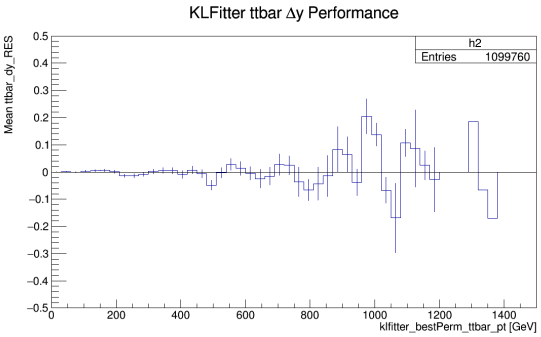

Figure C.2: KLFitter resolution for $t\bar{t}$ p_{T}.

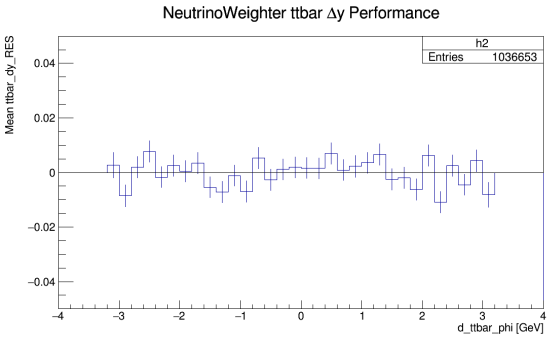

Figure C.3: NW resolution for $t\bar{t}$ ϕ.

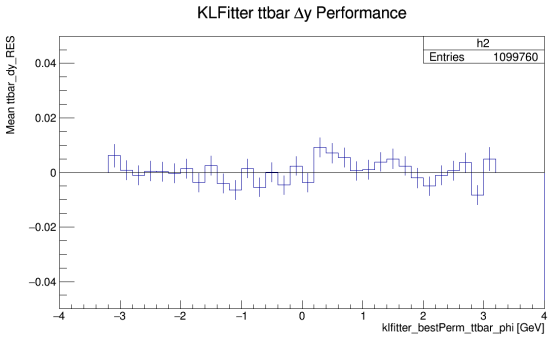

Figure C.4: KLFitter resolution for $t\bar{t}$ ϕ.

From the p_{T} plots, it can be seen that as these variables increase, the stability decreases for both algorithms. This is largely due to fewer statistics in this regime. Performing a cut at these higher values may not necessarily improve the performance but rather lead to a loss of potentially interesting high-energy events.

Other variables plotted included the NW d_weight_max and similarly the KLFitter log-likelihood. These are shown in Fig. C.5 and C.6.

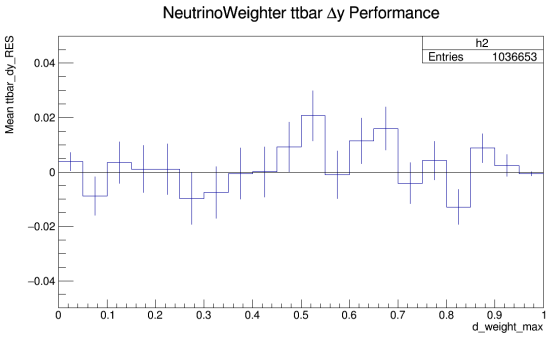

Figure C.5: NW resolution for max weight.

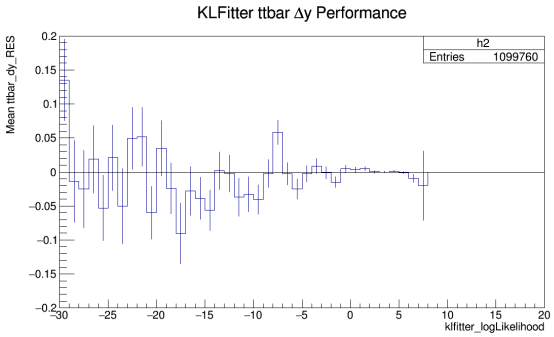

Figure C.6: KLFitter resolution for log-likelihood.

It was decided to keep events of maximum weight > 0 for the NW and log-likelihood > 0 for the KLFitter as they currently are. This does remove a fair fraction of events for the NW and KLFitter as can be seen in Fig. C.7 and C.8 so will have a non-negligible improvement on the performance. Fig. C.9 and C.10 show the rapidity, y, values for $t\bar{t}$ cases.

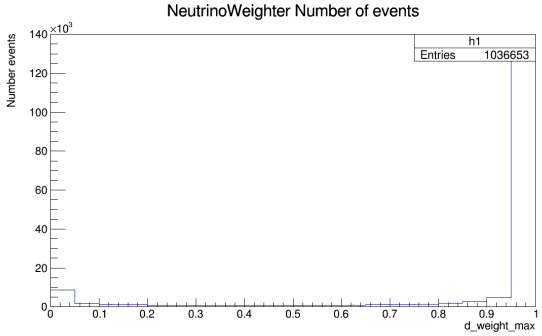

Figure C.7: Number of events binned by NW max weight.

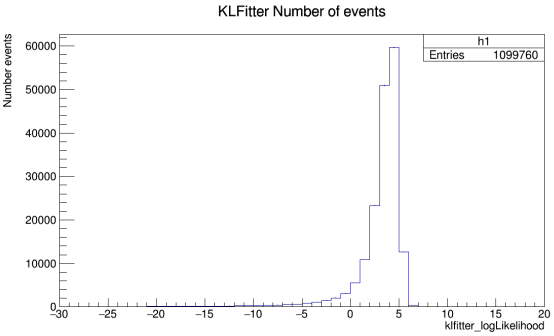

Figure C.8: Number of events binned by KLFitter log-likelihood.

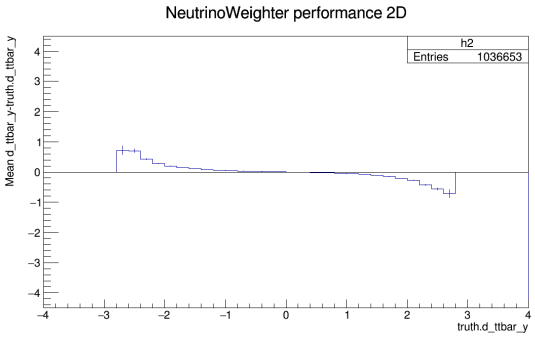

Figure C.9: NW performance for $t\bar{t}$ y.

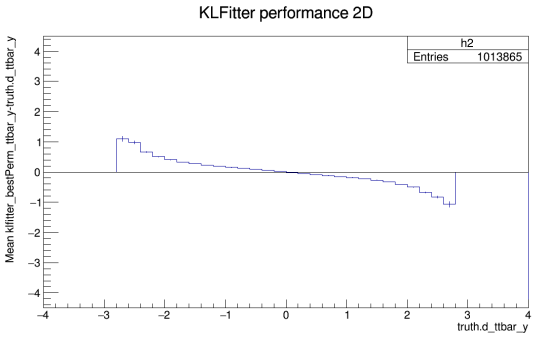

Figure C.10: KLFitter performance for $t\bar{t}$ y.

From the top and antitop mass plots, there is a clear linear trend. This is to be expected since the truth level top mass is constrained to its known value but the reco-level masses are allowed to float around this.

To conclude this study, it is clear the NW and KLFitter perform similarly, but in some cases, the KLFitter performs worse. This is surprising since with more freedom to smear and building on NW information, one would expect the KLFitter to perform better overall. It was thus decided to use the NW for the analysis.

C.0.1 Old method used only at the beginning of the analysis

Top quark kinematic reconstruction is tested based on a kinematic fitting (minimum χ^2) method developed for this analysis. The three vectors of two neutrinos from W bosons can be determined by minimizing the χ^2 defined as below equation.

For each event, the χ^2 is minimized with each possible permutation of the b-jets, leptons in the final state.

$$\begin{aligned}\chi^2 &= \left(\frac{m_{l_1\nu_1}-m_W}{\sigma_{m_W}}\right)^2+\left(\frac{b_1 m_{l_1\nu_1}-m_t}{\sigma_{m_t}}\right)^2+\left(\frac{m_{l_2\nu_2}-m_W}{\sigma_{m_W}}\right)^2+\left(\frac{b_2 m_{l_2\nu_2}-m_t}{\sigma_{m_t}}\right)^2 \\ &+ \left(\frac{p_{x,\nu_1}+p_{x,\nu_2}-E_x^{miss}}{\sigma_{MET}(m_{t\bar{t}})}\right)^2+\left(\frac{p_{y,\nu_1}+p_{y,\nu_2}-E_y^{miss}}{\sigma_{MET}(m_{t\bar{t}})}\right)^2 \end{aligned} \quad \text{(C.1)}$$

The first and third terms are constraint from the W boson mass, the second and forth terms are constraint from the top quark mass, and the last two terms correspond to constraint from measured E_T^{miss}. In the fitting process, p_t, η, ϕ of each neutrino (ν1,ν2) are treated as free parameters. This method is no longer used since it cost much CPU time and the performance is comparable to the other methods.

Appendix D

Response matrix

In the inclusive and differential measurements, response matrices were derived for use in the unfolding procedure. The response matrices are shown graphically below for the inclusive and differential measurements. The values on the x-axis represent the truth $\Delta|y|$ bins: 4 for the inclusive measurement, 20 for the differential measurement with respect to $m_{t\bar{t}}$ (4 $\Delta|y|$ bins in each of the 5 $m_{t\bar{t}}$ bins), 12 for the differential measurements with respect to $p_{\mathrm{T}}^{t\bar{t}}$ (4 $\Delta|y|$ bins in each of the 3 $p_{\mathrm{T}}^{t\bar{t}}$ bins), and 16 for the differential measurements with respect to $\beta_z^{t\bar{t}}$ (4 $\Delta|y|$ bins in each of the 4 $\beta_z^{t\bar{t}}$ bins). The y-axis represents the reconstructed values for the same binning configuration as the x-axis. These matrices are shown below for the inclusive measurement in Fig. D.1-D.3.

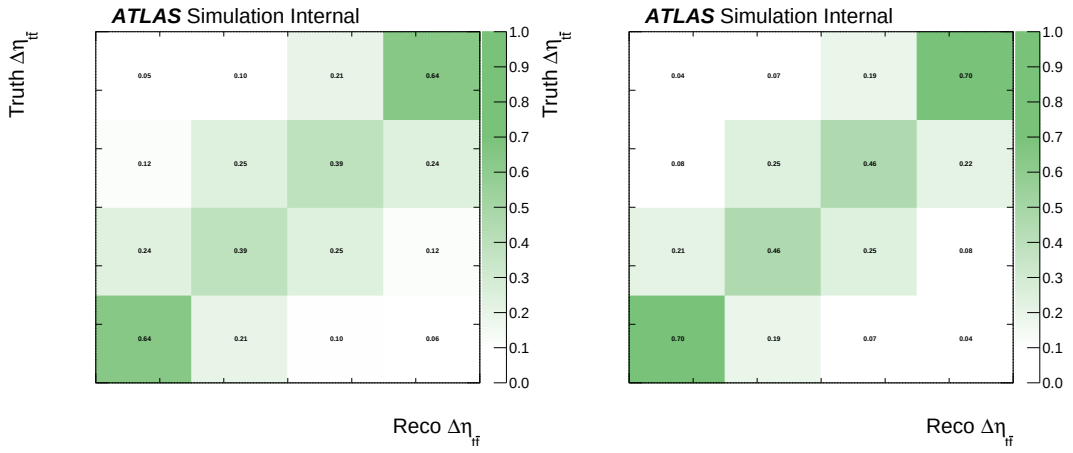

(a) $e\mu$ 1 b-tag (b) $e\mu$ 2 b-tag

Figure D.1: The response matrices in the $e\mu$ 1 b-tag and 2 b-tag channel, split by positive and negative lepton charge, for the inclusive measurement.

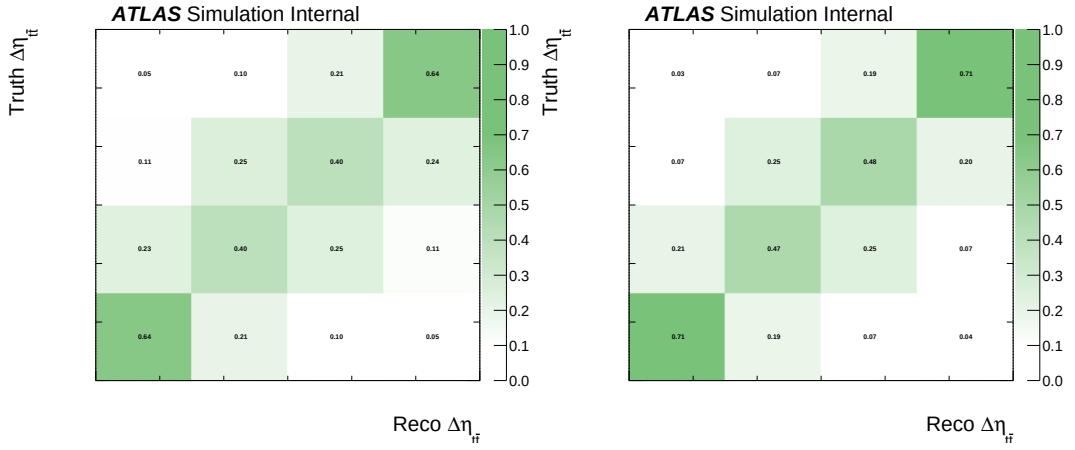

(a) ee 1 b-tag (b) ee 2 b-tag

Figure D.2: The response matrices in the ee 1 b-tag and 2 b-tag channel, split by positive and negative lepton charge, for the inclusive measurement.

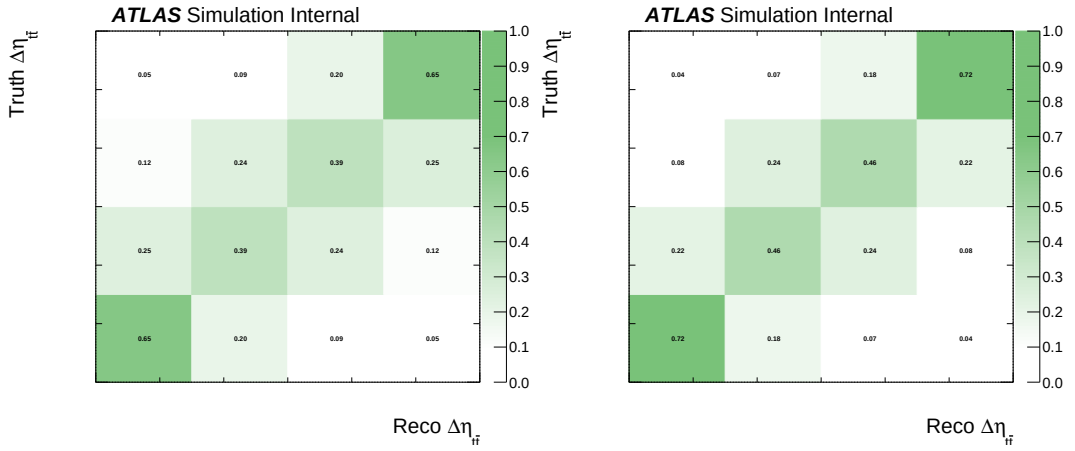

(a) $\mu\mu$ 1 b-tag (b) $\mu\mu$ 2 b-tag

Figure D.3: The response matrices in the $\mu\mu$ 1 b-tag and 2 b-tag channel, split by positive and negative lepton charge, for the inclusive measurement.

At the differential measurement, these matrices are also shown in $m_{t\bar{t}}$ (Fig. D.4-D.6), $p_{\mathrm{T}}^{t\bar{t}}$ (Fig. D.7-D.9) and $\beta_z^{t\bar{t}}$ (Fig. D.10-D.12).

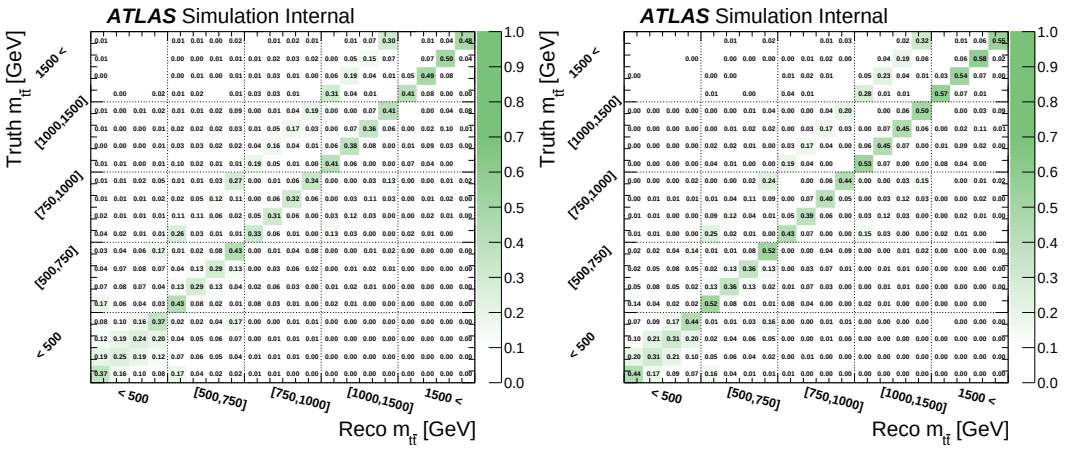

(a) $e\mu$ 1 b-tag (b) $e\mu$ 2 b-tag

Figure D.4: The response matrices in the $e\mu$ 1 b-tag and 2 b-tag channel, split by positive and negative lepton charge, for the differential $m_{t\bar{t}}$ measurement.

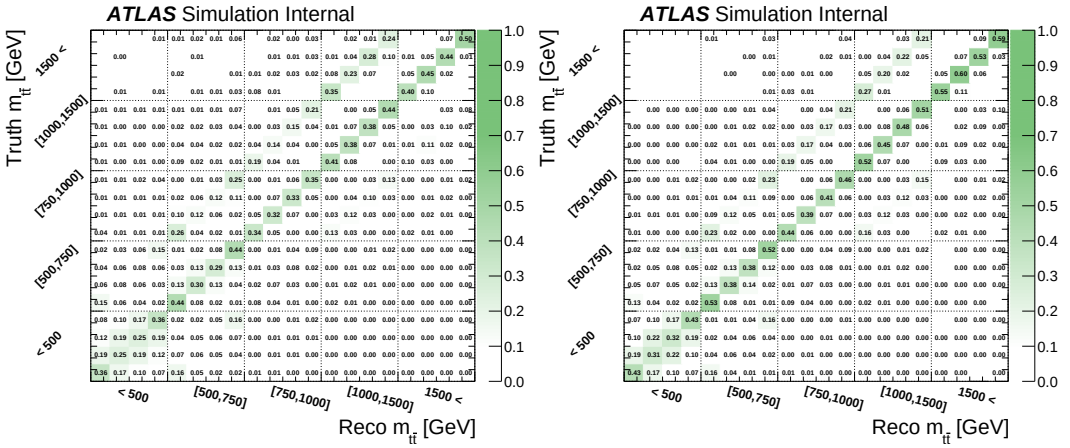

(a) ee 1 b-tag (b) ee 2 b-tag

Figure D.5: The response matrices in the ee 1 b-tag and 2 b-tag channel, split by positive and negative lepton charge, for the differential $m_{t\bar{t}}$ measurement.

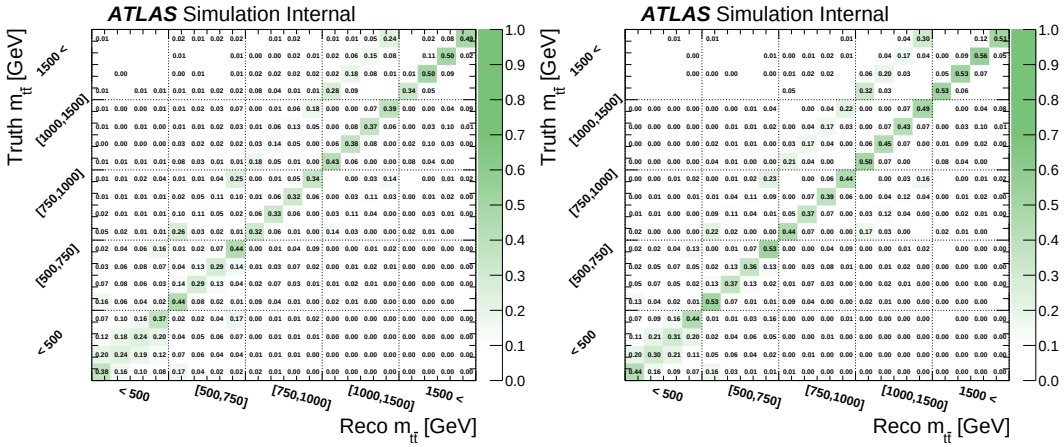

(a) $\mu\mu$ 1 b-tag (b) $\mu\mu$ 2 b-tag

Figure D.6: The response matrices in the $\mu\mu$ 1 b-tag and 2 b-tag channel, split by positive and negative lepton charge, for the differential $m_{t\bar{t}}$ measurement.

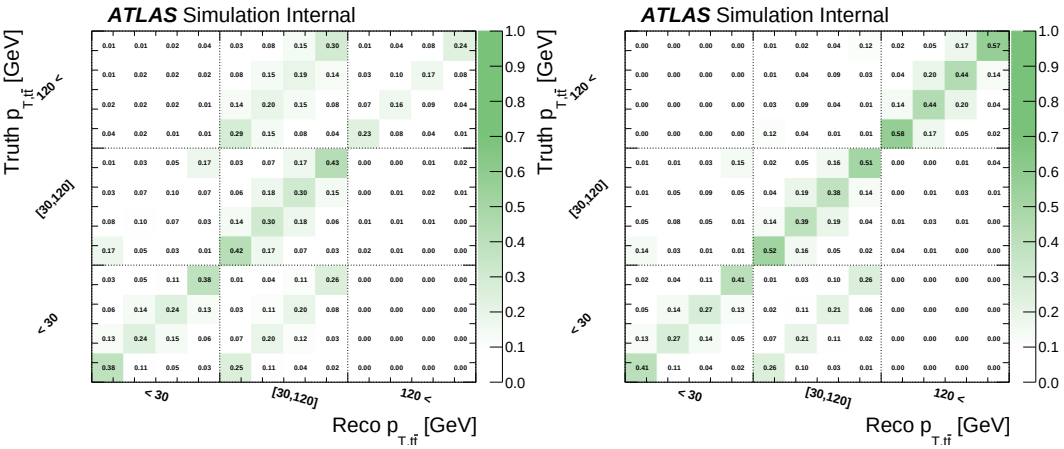

(a) $e\mu$ 1 b-tag (b) $e\mu$ 2 b-tag

Figure D.7: The response matrices in the $e\mu$ 1 b-tag and 2 b-tag channel, split by positive and negative lepton charge, for the differential $p_{\mathrm{T}}^{t\bar{t}}$ measurement.

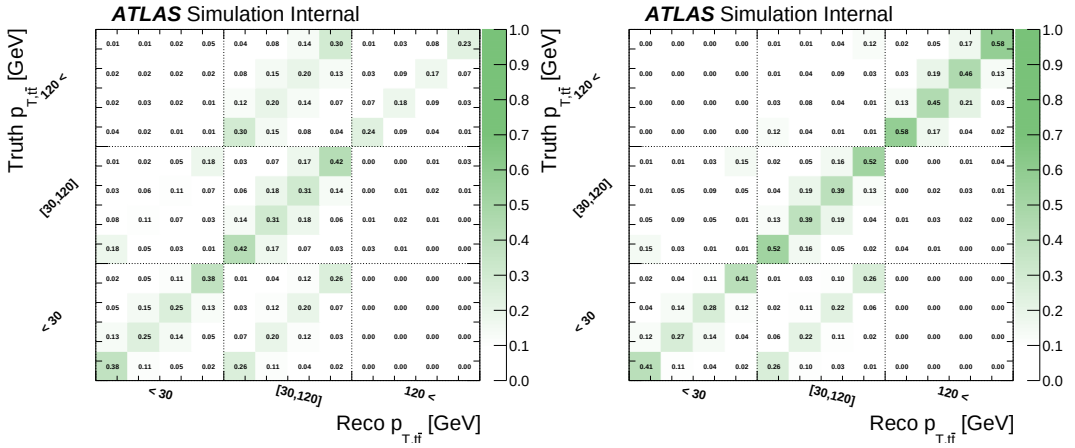

(a) ee 1 b-tag (b) ee 2 b-tag

Figure D.8: The response matrices in the ee 1 b-tag and 2 b-tag channel, split by positive and negative lepton charge, for the differential $p_{\mathrm{T}}^{t\bar{t}}$ measurement.

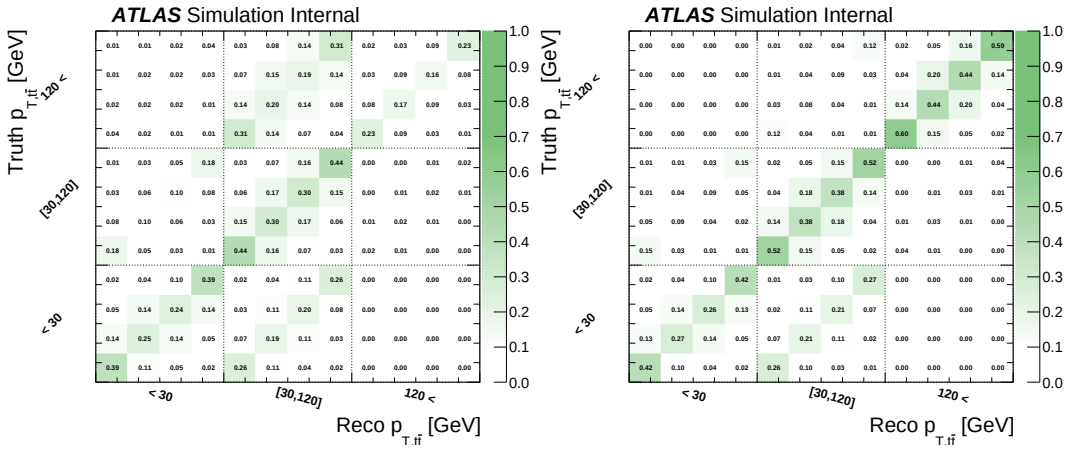

(a) $\mu\mu$ 1 b-tag (b) $\mu\mu$ 2 b-tag

Figure D.9: The response matrices in the $\mu\mu$ 1 b-tag and 2 b-tag channel, split by positive and negative lepton charge, for the differential $p_{\mathrm{T}}^{t\bar{t}}$ measurement.

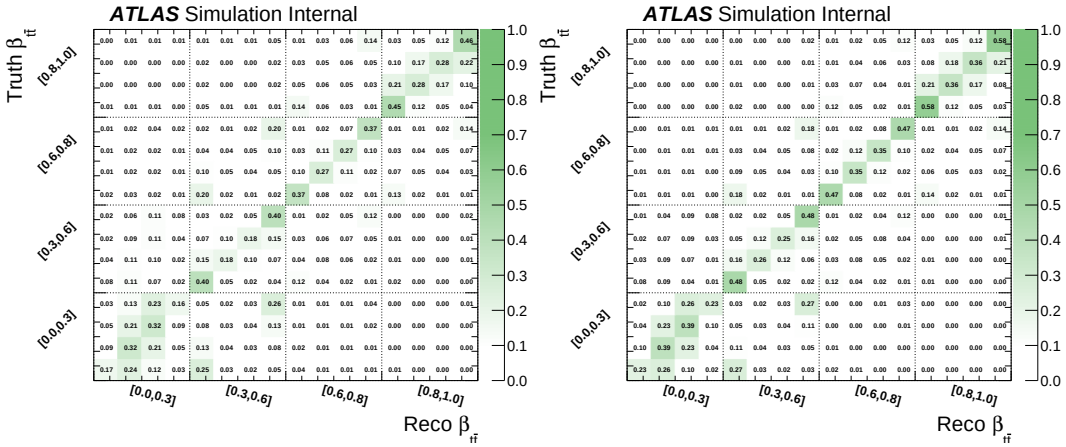

(a) $e\mu$ 1 b-tag (b) $e\mu$ 2 b-tag

Figure D.10: The response matrices in the $e\mu$ 1 b-tag and 2 b-tag channel, split by positive and negative lepton charge, for the differential $\beta_z^{t\bar{t}}$ measurement.

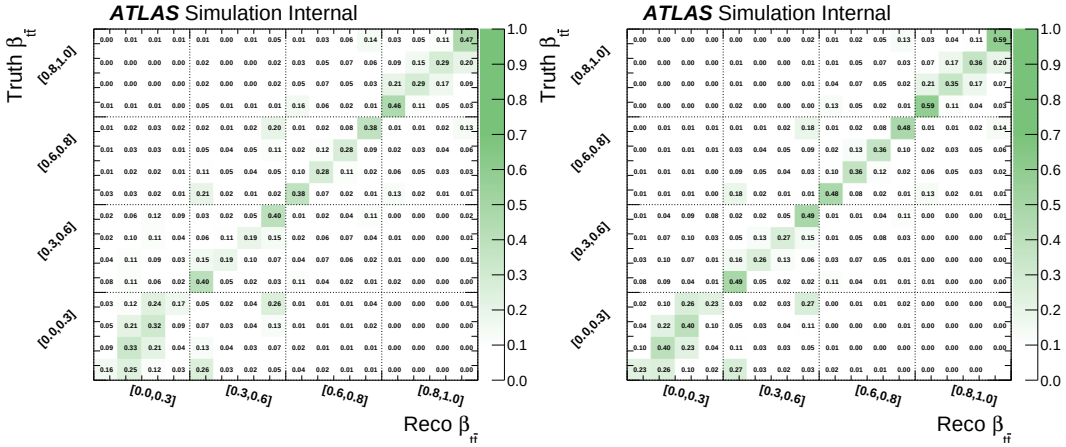

(a) ee 1 b-tag (b) ee 2 b-tag

Figure D.11: The response matrices in the ee 1 b-tag and 2 b-tag channel, split by positive and negative lepton charge, for the differential $\beta_z^{t\bar{t}}$ measurement.

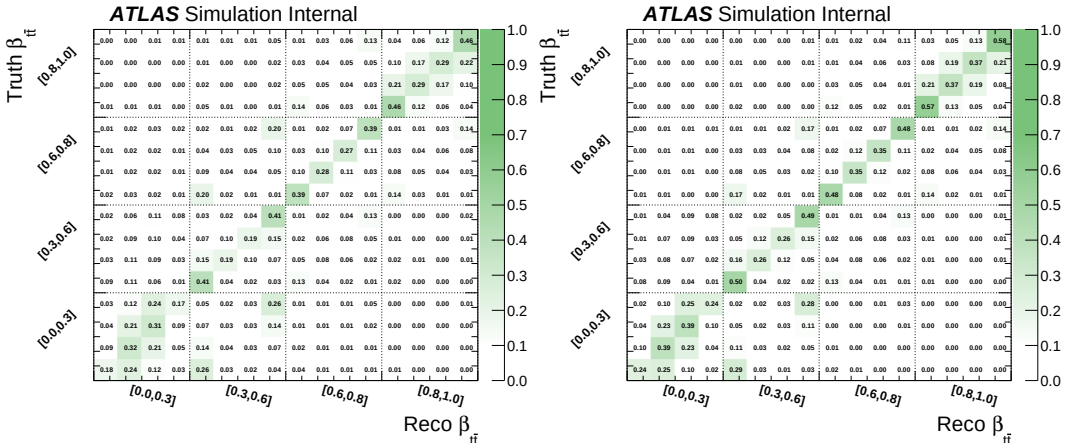

(a) $\mu\mu$ 1 b-tag

(b) $\mu\mu$ 2 b-tag

Figure D.12: The response matrices in the $\mu\mu$ 1 b-tag and 2 b-tag channel, split by positive and negative lepton charge, for the differential $\beta_z^{t\bar{t}}$ measurement.

Appendix E

Iterative Bayesian method

The unfolding from reconstruction level to parton level is carried out using the `RooUnfold` package with an iterative method inspired by Bayes' theorem. The number of iterations in the unfolding procedure is chosen to be four while it should be optimized to balance the goodness of fit and statistical uncertainties.

The detector response is described using a migration matrix that relates the generated parton(particle)-level distributions to the measured distributions. The migration matrix $\mathcal{M}$ is determined using Powheg+Pythia8 $t\bar{t}$ Monte Carlo simulation, where the parton-level top quark is defined as the top quark after radiation and before decay.

Fig. E.1(a) and E.1(b) present the migration matrices of the top quark p_{T} and rapidity in the $e\mu$ channel. The matrix element $\mathcal{M}_{ij}$ represents the probability for an event generated at parton level with X in bin i to have a reconstructed X in bin j, so the elements of each row add up to unity (within rounding uncertainties).

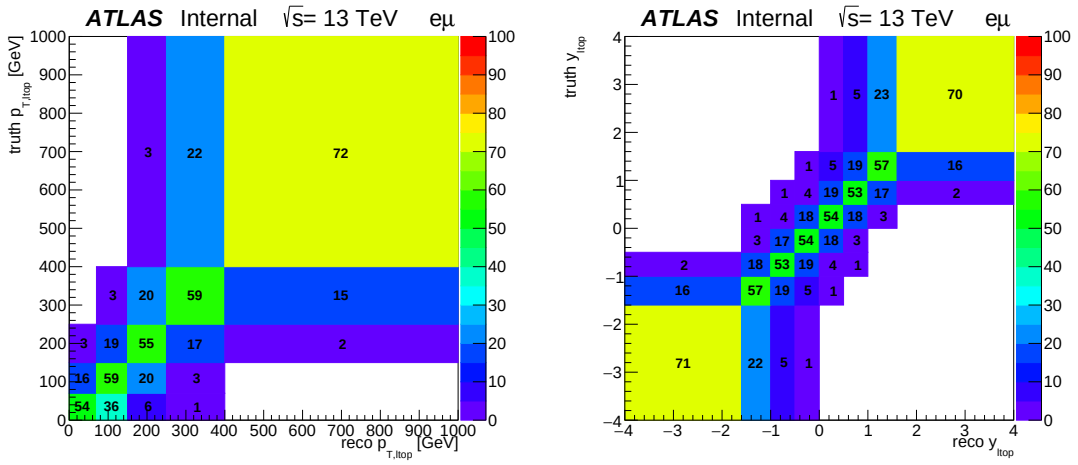

(a) top quark p_{T} matrix

(b) top quark rapidity matrix

Figure E.1: Migration matrices of the top quark p_{T} and rapidity in the $e\mu$ channel

The probability for the parton-level events to remain in the same bin in the measured distribution is shown in the diagonal, and the off-diagonal elements represent the fraction of parton-level events that migrate into other bins. Fig. E.2 shows two dimensional response matrix for $\Delta|y_{t\bar{t}}| \times m_{t\bar{t}}$.

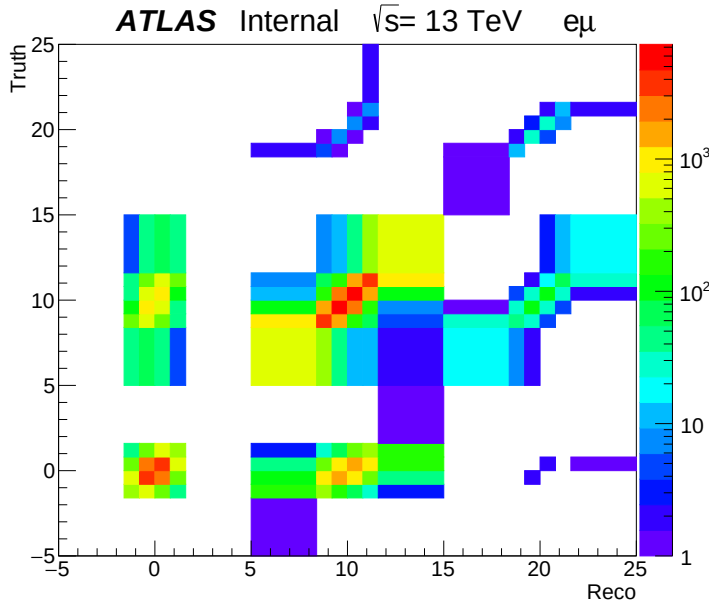

Figure E.2: Two dimensional response matrix ($\Delta|y_{t\bar{t}}| \times m_{t\bar{t}}$)

E.0.1 Closure test

When using pseudo-data generated with the help of Monte Carlo simulations, the truth distribution is known, thus the unfolding results may be directly compared to it. Such comparisons, where pseudo-data are unfolded and compared to the truth are often called closure tests. The closure tests are based on independent Monte Carlo samples. Fig. E.3 shows the result of closure test in differential $A_{\mathrm{C}}^{t\bar{t}}$ as a function of the mass of $t\bar{t}$ system. The result shows that the unfolded $A_{\mathrm{C}}^{t\bar{t}}$ value is not closer to the truth $A_{\mathrm{C}}^{t\bar{t}}$ value and does not converge even if the number of times of iteration increases (especially 2nd $m_{t\bar{t}}$ bin ([450,750] GeV)). As a result, the unfolded $A_{\mathrm{C}}^{t\bar{t}}$ should be evaluated without using iterative Bayesian method.

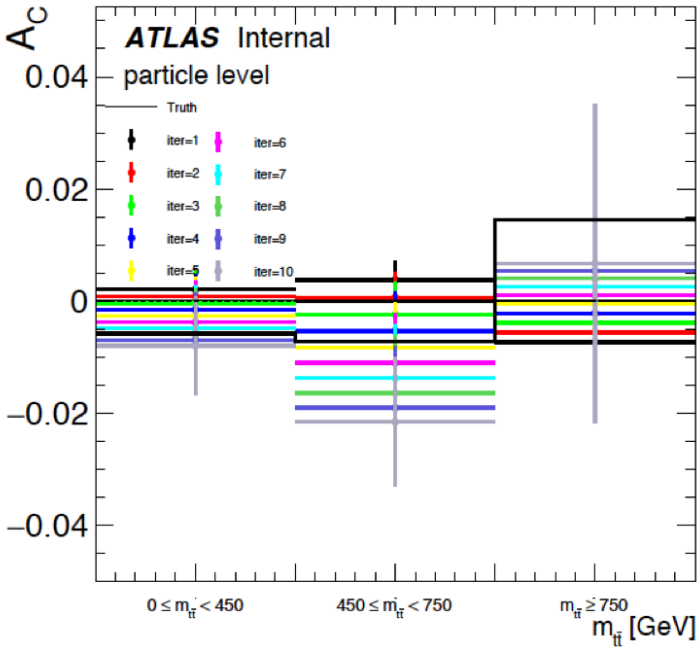

Figure E.3: Result of closure test in differential $A_{\mathrm{C}}^{t\bar{t}}$ as a function of $m_{t\bar{t}}$

Appendix F

PROTOS reweighting

To test if there is any bias in the unfolding procedure and how correctly unfold back to expected charge asymmetry, a linearity test and binning optimization were carried out as discussed in Sec. 7.4. The benchmark distributions with arbitrary shifted charge asymmetry for above tests are generated by using PROTOS $t\bar{t}$ generator [64]. To generate benchmark points, the process of light axigluon decay into top anti-top pair with various couplings are considered. In table F.1, the parameters used in PROTOS are summarized.

Table F.1: Parameters' settings used to simulate different values of the $A_{\mathrm{C}}^{t\bar{t}}$ in PROTOS.

	m^{axigluon} [GeV]	guL	guR	gdL	gdR	gtL	gtR
SM	-	0.0	0.0	0.0	0.0	0.0	0.0
1%	250. $\pm$ 50.	-0.1	0.1	-0.1	0.1	-1.9	1.9
2%	250. $\pm$ 50.	-0.1	0.1	-0.1	0.1	-3.9	3.9
3%	250. $\pm$ 50.	-0.1	0.1	-0.1	0.1	-6.1	6.1
4%	250. $\pm$ 50.	-0.1	0.1	-0.1	0.1	-8.3	8.3

The simulated $\Delta|y|$ distributions are shifted base on the reweighting function derived by taking the ratio between shifted and nominal distributions (see Fig. F.1)

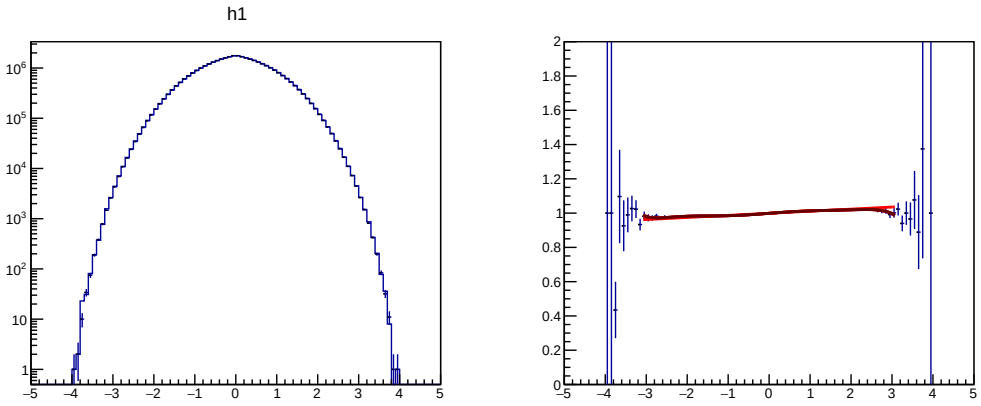

(a) 1% shift

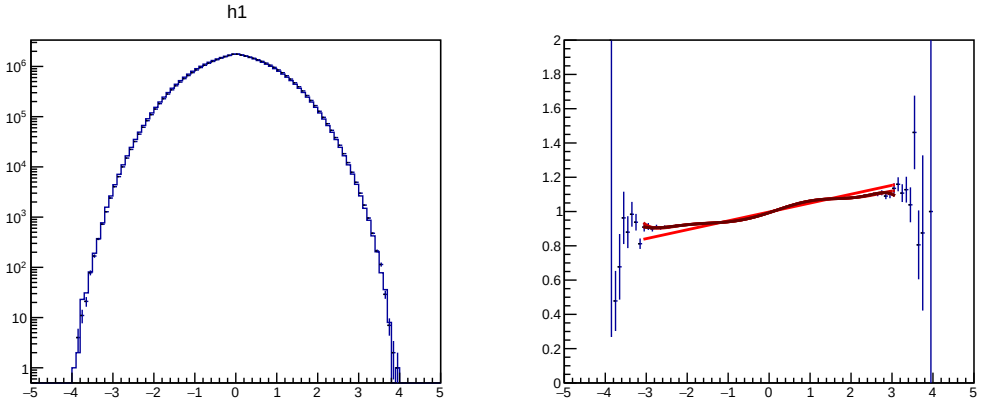

(b) 4% shift

Figure F.1: Comparison of shifted $\Delta|y|$ distribution obtained from PROTOS and nominal distribution (left), together with their ratio and derived reweighting function (right).

Appendix G

Nuisance parameters

In this section all the Nuisance parameters for inclusive and differential measurements are presented for the dilepton channel. The nuisance parameters are obtained through the marginalization procedure of Full Bayesian Unfolding(FBU), as shown in Fig. G.1 for the inclusive measurement, Fig. G.2 for the differential measurement as a function of the invariant mass of the $t\bar{t}$ system, Fig. G.3 for the differential measurement as a function of the transeverse momentum of the $t\bar{t}$ system, Fig. G.4 for the differential measurement as a function of the transverse boost of the $t\bar{t}$ system. These black dots correspond to asimov data. These red dots correspond to data(79.7 fb^{-1}) fit. These color regions highlight the 1σ (green) and 2σ (yellow) intervals of the prior probability density. The estimations of nuisance parameters are using PyMC3.

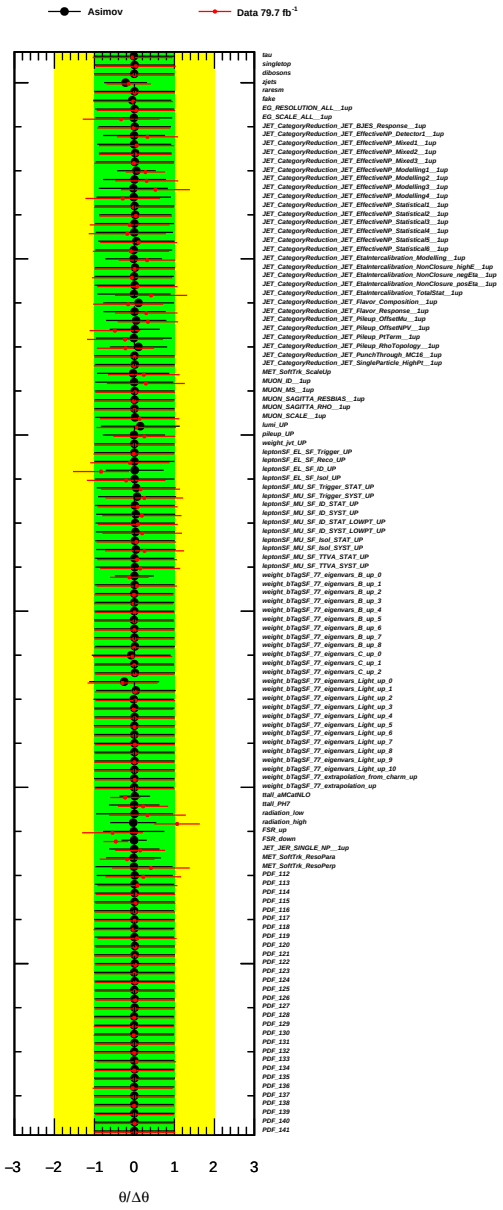

Figure G.1: Nuisance parameters for the inclusive $A_C^{t\bar{t}}$ measurement using asimov data and data (79.7 fb^{-1}) in dilepton channel. The color regions highlight the 1σ (green) and 2σ (yellow) intervals of the prior probability density. The boostrapping is applied, fit is performed with 10000 steps, while 2500 steps are used for tuning

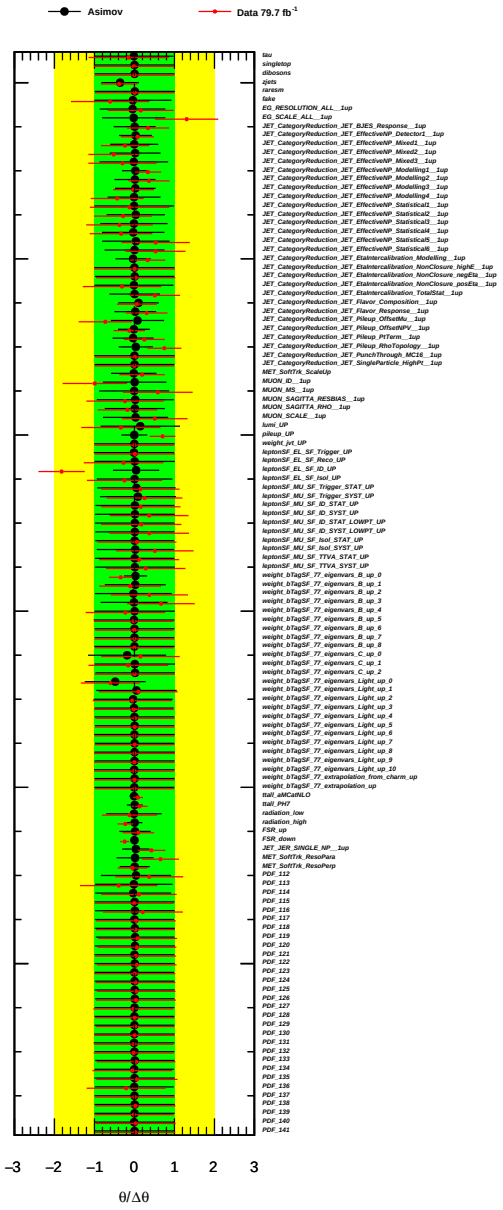

Figure G.2: Nuisance parameters for the $A_{\mathrm{C}}^{t\bar{t}}$ measurement as a function of the $t\bar{t}$ mass using asimov data (black dots) and data (79.7 fb^{-1}) (red dots). The color regions highlight the 1σ (green) and 2σ (yellow) intervals of the prior probability density. The boostrapping is applied, fit is performed with 10000 steps, while 2500 steps are used for tuning.

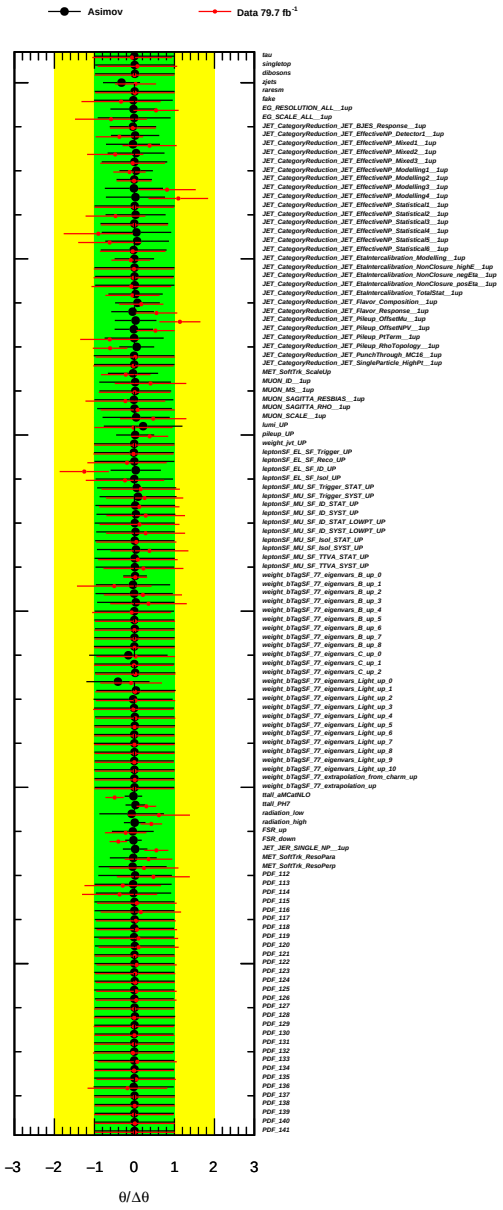

Figure G.3: Nuisance parameters for the $A_{\mathrm{C}}^{t\bar{t}}$ measurement as a function of the transverse momentum of the $t\bar{t}$ system using asimov data (black dots) and data (79.7 fb^{-1}) (red dots). The color regions highlight the 1σ (green) and 2σ (yellow) intervals of the prior probability density. The boostrapping is applied, fit is performed with 10000 steps, while 2500 steps are used for tuning.

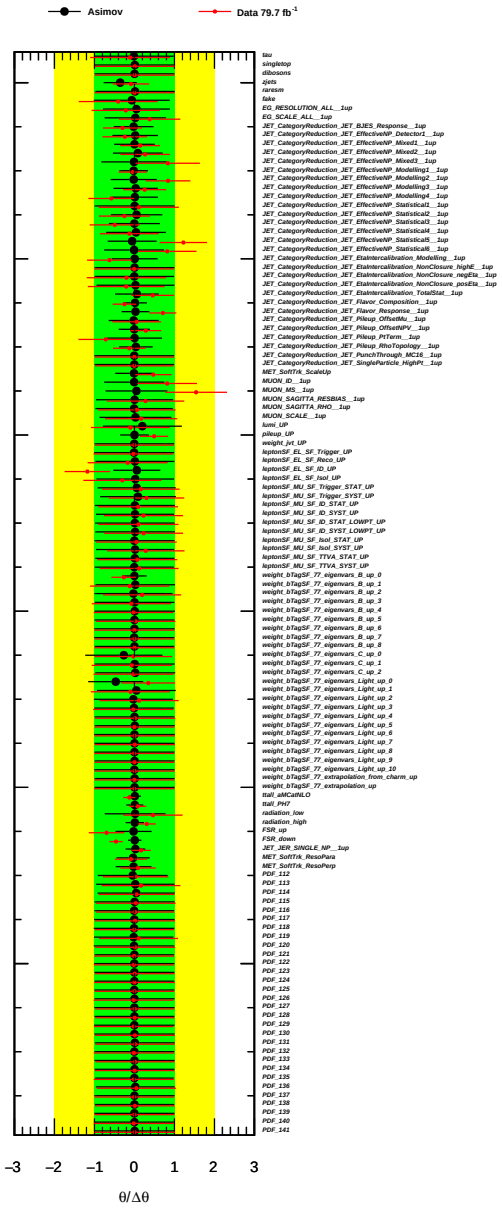

Figure G.4: Nuisance parameters for the $A_{\mathrm{C}}^{t\bar{t}}$ measurement as a function of the boost of the $t\bar{t}$ system using asimov data (black dots) and data (79.7 fb^{-1}) (red dots). The color regions highlight the 1σ (green) and 2σ (yellow) intervals of the prior probability density. The boostrapping is applied, fit is performed with 10000 steps, while 2500 steps are used for tuning.

Appendix H

Test of signal modeling uncertainties

In order to check that there is not too strong constrains for the uncertainties related to singal modelling for the unfolded result, total uncertainties are compared.

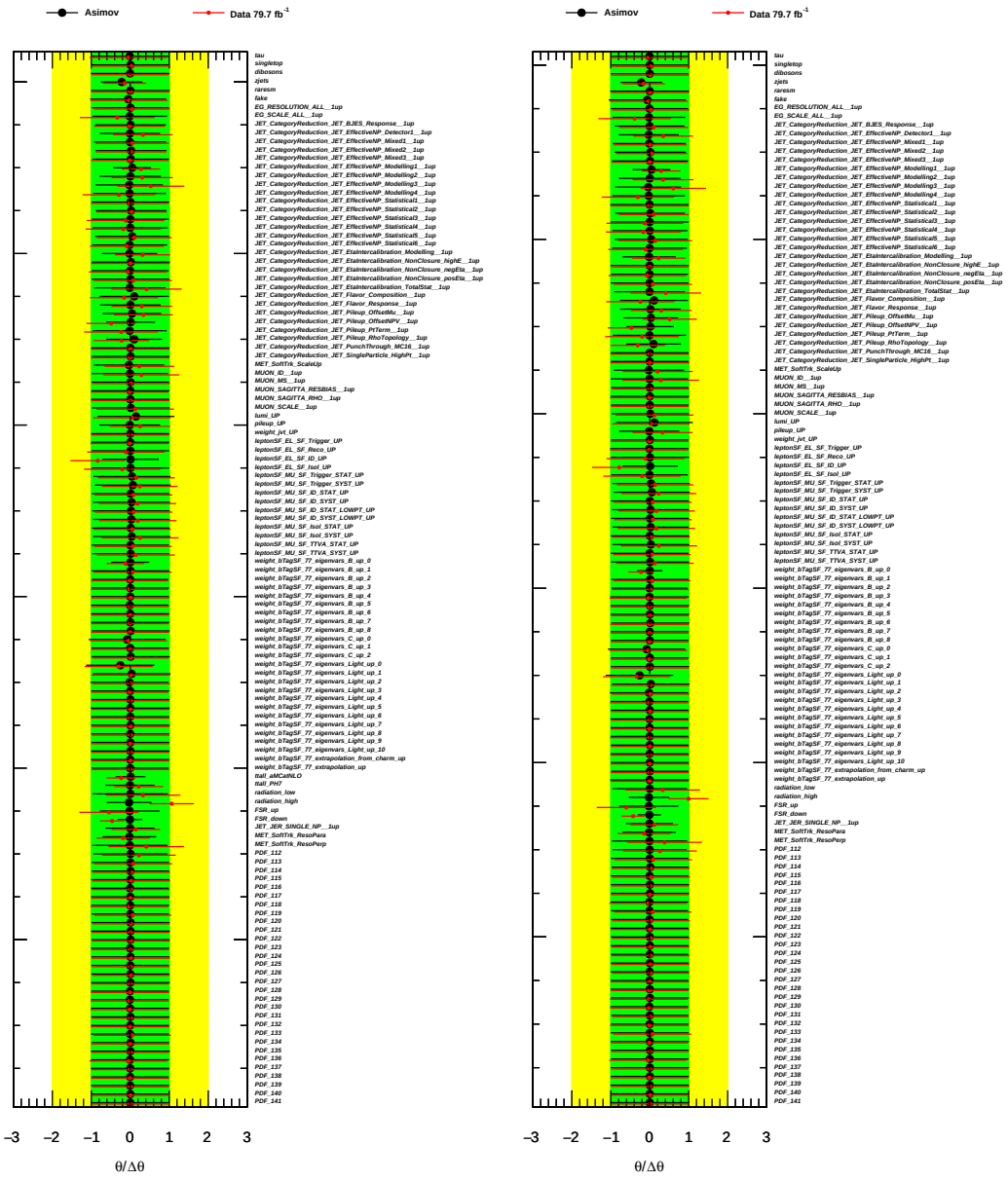

(a) Asimov fit with ME+PS

(b) Asimov fit without ME+PS

Figure H.1: Comparison of profiling plot for the inclusive $A_{\mathrm{C}}^{t\bar{t}}$ measurement

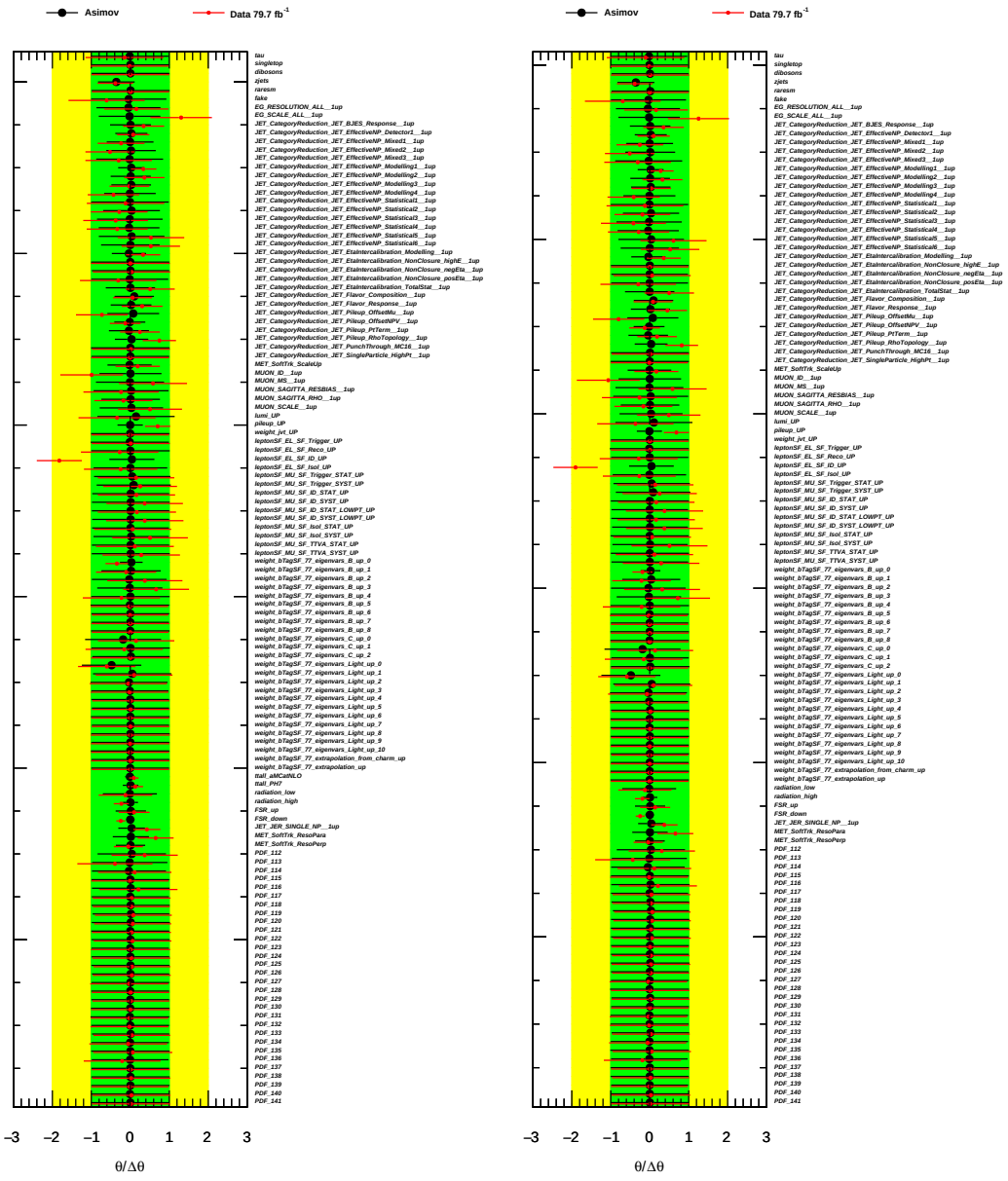

(a) Asimov fit with ME+PS

(b) Asimov fit without ME+PS

Figure H.2: Comparison of profiling plot for the $A_{\mathrm{C}}^{t\bar{t}}$ measurement as a function of the $t\bar{t}$ mass.

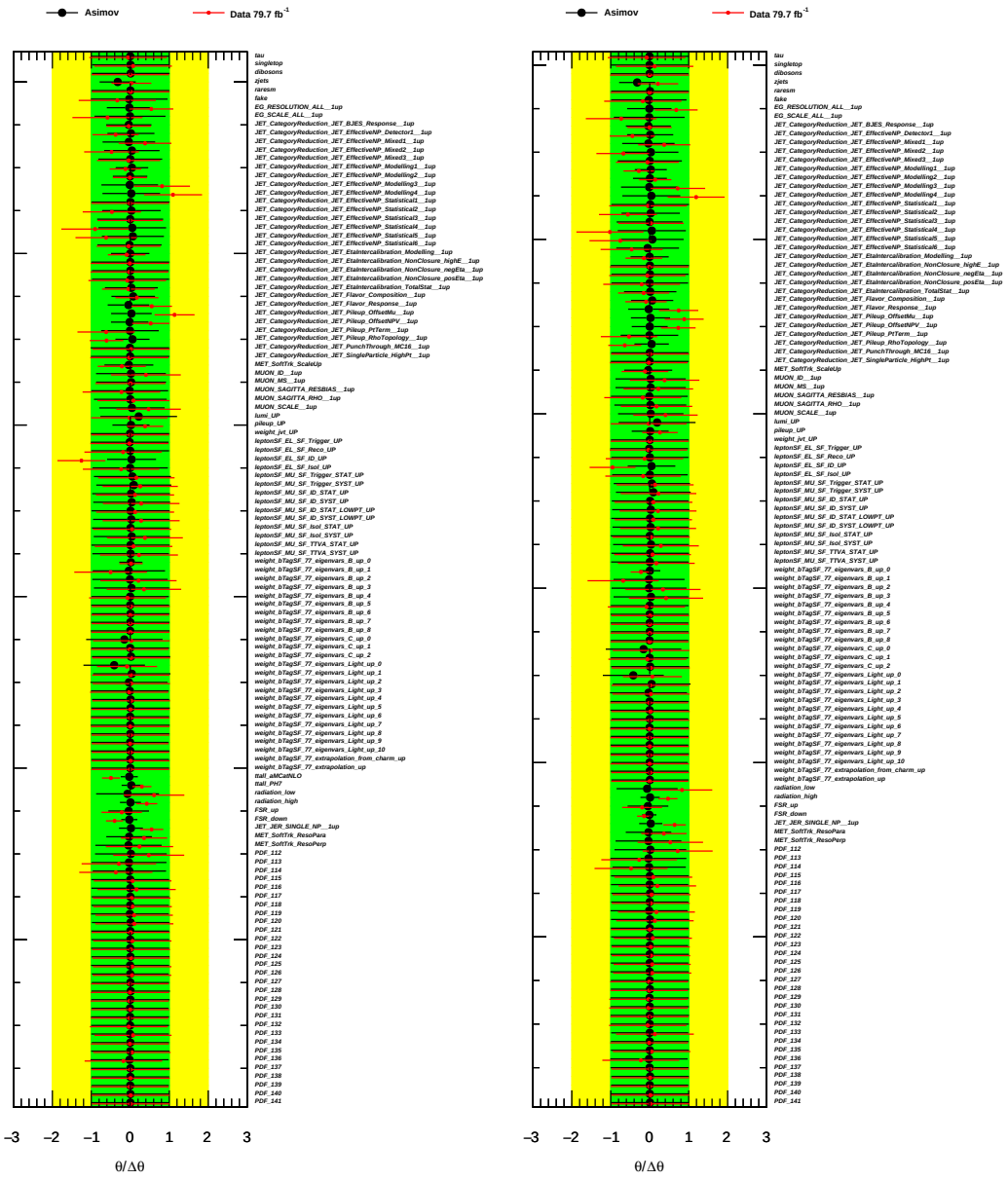

(a) Asimov fit with ME+PS

(b) Asimov fit without ME+PS

Figure H.3: Comparison of profiling plot for the $A_{\mathrm{C}}^{t\bar{t}}$ measurement as a function of the transverse momentum of the $t\bar{t}$ system.

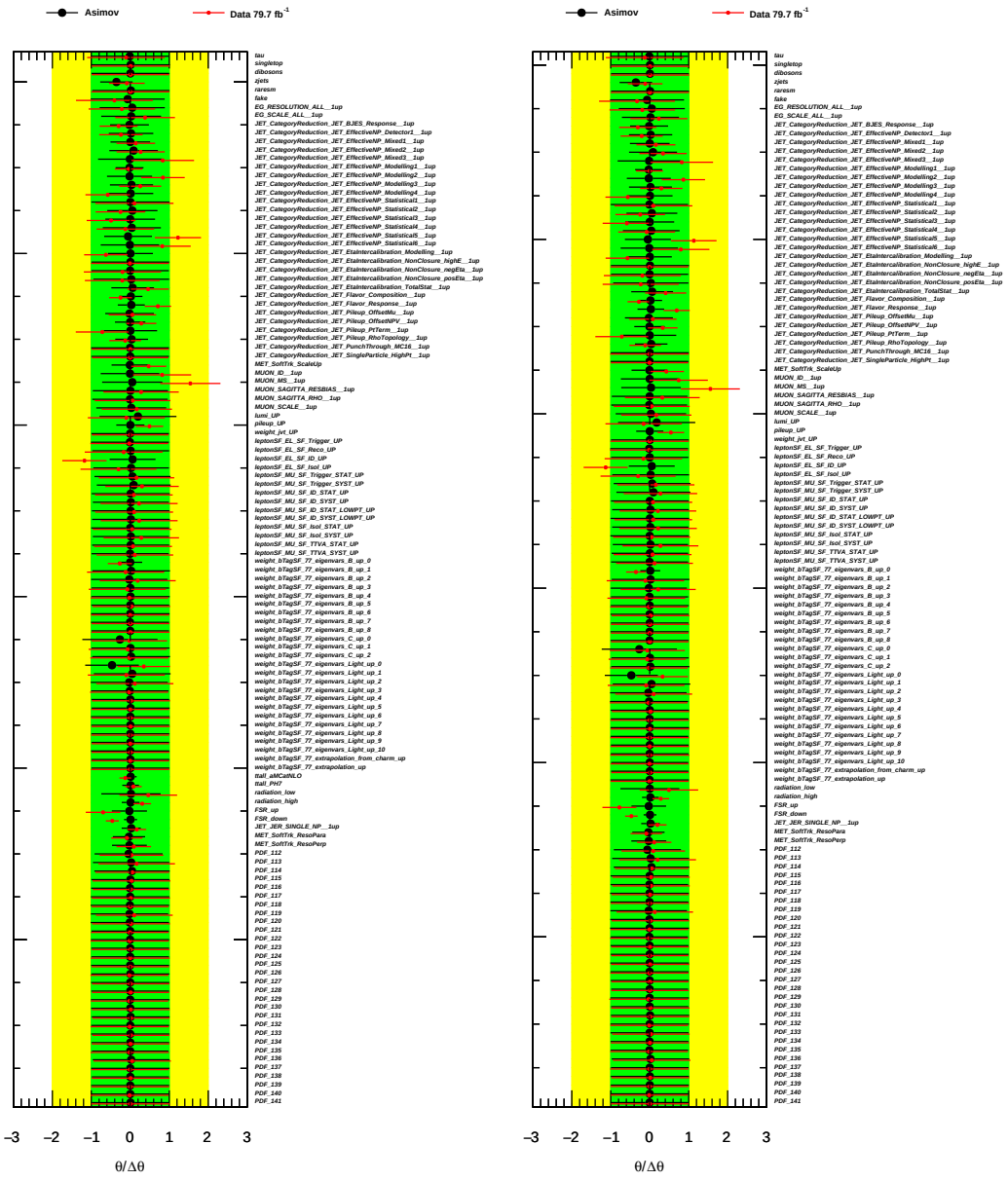

(a) Asimov fit with ME+PS

(b) Asimov fit without ME+PS

Figure H.4: Comparison of profiling plot for the $A_{\mathrm{C}}^{t\bar{t}}$ measurement as a function of the boost of the $t\bar{t}$ system.

A comparison of ME and PS affecting the measurements are shown in Table H.1 using MC samples.

Table H.1: Comparison of unfold $A_C^{t\bar{t}}$ value with ME and PS from the different source affecting the $A_C^{t\bar{t}}$ in full phase space

		unfold $A_C^{t\bar{t}}$ w/o ME+PS	unfold $A_C^{t\bar{t}}$ w/ ME+PS
inclusive		0.0033	0.0033
$m_{t\bar{t}}$	< 500 GeV	0.0027	0.0029
	500-750 GeV	0.0030	0.0028
	750-1000 GeV	0.0064	0.0063
	1000-1500 GeV	0.0015	0.0016
	> 1500 GeV	0.0120	0.0112
$p_{T,t\bar{t}}$	< 30 GeV	0.0092	0.0095
	30-120 GeV	0.0003	0.0005
	> 120 GeV	0.0004	0.0006
$\beta_{z,t\bar{t}}$	0-0.3	-0.0005	-0.0004
	0.3-0.6	0.0011	0.0012
	0.6-0.8	0.0026	0.0026
	0.8-1.0	0.0083	0.0084

The unfolded inclusive and differential charge asymmetries using different scenarios with (dark blue) and without (red) marginalization of the PS and ME uncertainties are shown in Fig. H.5.

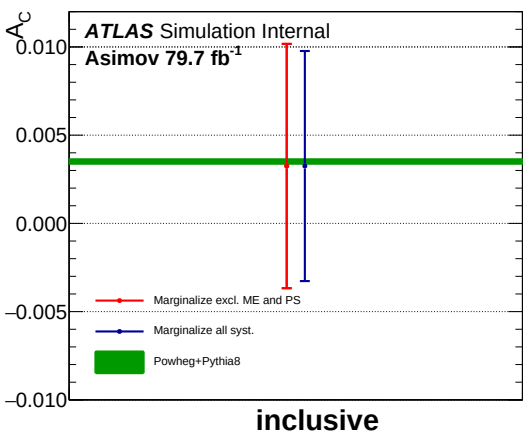

(a) Asimov test inclusive

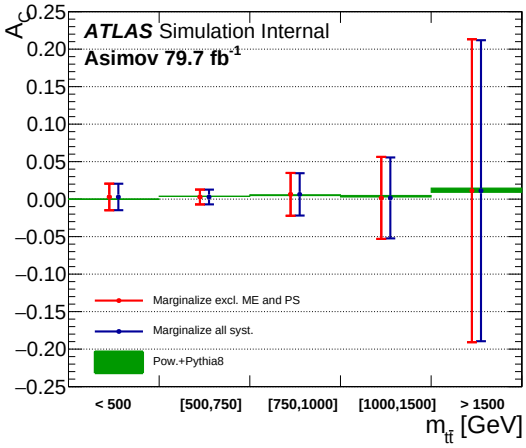

(b) Asimov test differential $m_{t\bar{t}}$

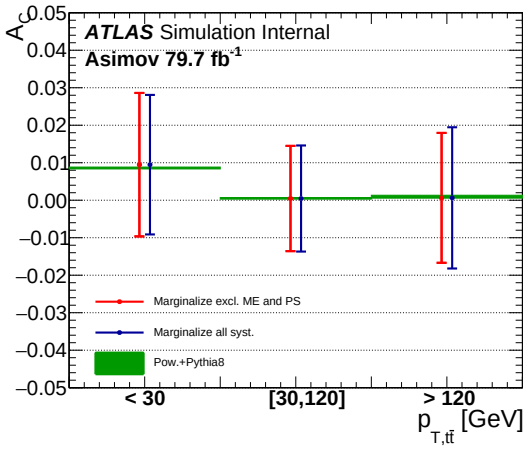

(c) Asimov test differential $p_{T,t\bar{t}}$

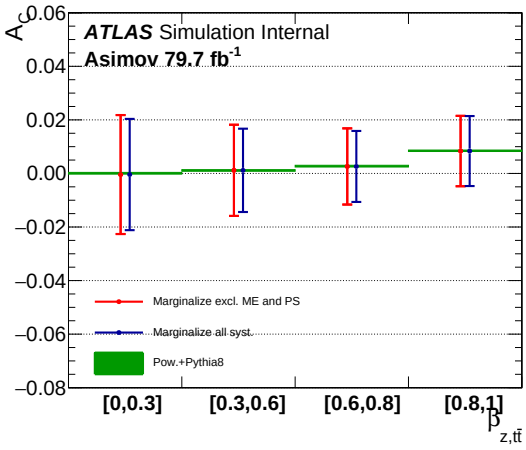

(d) Asimov test differential $\beta_{z,t\bar{t}}$

Figure H.5: Comparison of sensitivities for inclusive and differential charge asymmetries as a function of the invariant mass, transverse momentum, and the transverse boost of the top pair system, from the Asimov data sample in dilepton channel.